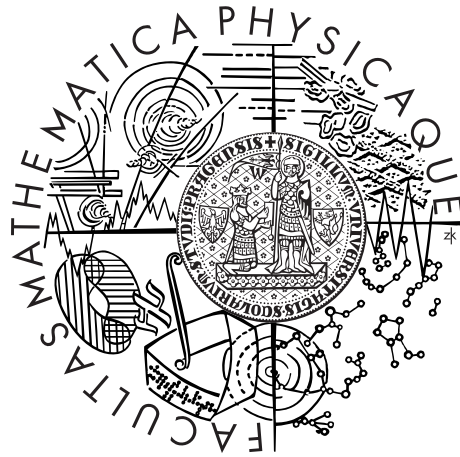


Charles University in Prague  
Faculty of Mathematics and Physics

## DOCTORAL THESIS



Jaroslav Hamerský

## Astrophysical processes near a galactic centre

Astronomical Institute of the Academy of Sciences  
of the Czech Republic

Supervisor of the doctoral thesis: prof. RNDr. Vladimír Karas, DrSc.

Study programme: Physics

Specialization: Theoretical physics,  
astronomy and astrophysics

Prague 2015



I would like to thank my supervisor Vladimír Karas for the patient guidance, advice and rewarding discussions he has provided throughout my doctoral studies.

I acknowledge the Astronomical Institute of the Czech Academy of Sciences for providing me with a stimulating working environment and appropriate computational equipment.



I declare that I carried out this doctoral thesis independently, and only with the cited sources, literature and other professional sources.

I understand that my work relates to the rights and obligations under the Act No. 121/2000 Coll., the Copyright Act, as amended, in particular the fact that the Charles University in Prague has the right to conclude a license agreement on the use of this work as a school work pursuant to Section 60 paragraph 1 of the Copyright Act.

In Prague, June 24, 2015

.....



Název práce: Astrofyzikální procesy v blízkosti jádra galaxie

Autor: Jaroslav Hamerský

Katedra: Astronomický ústav Akademie věd České republiky

Vedoucí disertační práce: prof. RNDr. Vladimír Karas, DrSc., Astronomický ústav Akademie věd České republiky

Abstrakt: Akreční disk je důležitý astrofyzikální jev, jehož přítomnost je klíčem k vysvětlení mnoha procesů souvisejících s tokem hmoty a uvolňováním energie ve formě záření na různých prostorových škálách, a to jak kolem málo hmotných tak kolem superhmotných černých děr. Pokud je jeho stacionární stav perturbován, disk začne oscilovat, a jestliže při tom nějaká část disku přesáhne uzavřenou ekvipotenciální plochu, je tento materiál akreován, nebo urychlen ve formě výtrysku. Tyto oscilace jsou zdrojem informací o časoprostoru a o vnitřní struktuře disku. V této práci se zabýváme studiem oscilačních a akrečních vlastností geometricky tlustých akrečních disků pomocí obecně relativistických magnetohydrodynamických simulací v axiálně symetrickém 2-D přístupu. Diskutujeme vliv velkorozměrového magnetického pole a profilu hustoty momentu hybnosti na oscilace disku a na pohyb akreované hmoty.

Klíčová slova: Černá díra, akreční disk, obecná relativita, jádro galaxie

Title: Astrophysical processes near a galactic centre

Author: Jaroslav Hamerský

Department: Astronomical Institute of the Academy of Sciences of the Czech Republic

Supervisor: prof. RNDr. Vladimír Karas, DrSc., Astronomical Institute of the Academy of Sciences of the Czech Republic

Abstract: An accretion torus is an important astrophysical phenomenon which is believed to account for various features of mass inflow and release of radiation on diverse scales near stellar-mass as well as supermassive black holes. When the stationary torus is perturbed it starts to oscillate and once some part of the torus overflows the closed equipotential surface, defined by the stationary solution, this material is accreted or ejected. These oscillations reveal both spacetime properties and the intrinsic characteristics of the torus model. We study the oscillation and accretion properties of geometrically thick accretion tori using general relativistic magnetohydrodynamic simulations. Assuming axial symmetry these simulations are restricted to 2-D approximation. We discuss the impact of the presence of the large scale magnetic field and the profile of the specific angular momentum on the oscillation properties and on the accretion flow motion.

Keywords: Black hole, accretion torus, general relativity, galactic centre



# Contents

<b>Preface</b>	<b>3</b>
<b>1 Introduction</b>	<b>5</b>
1.1 Galactic centre and centres of other galaxies . . . . .	5
1.2 AGN and jets . . . . .	8
1.3 Accretion with angular momentum (fluid tori) . . . . .	9
1.4 Role of small-scale magnetic fields (MRI) . . . . .	16
<b>2 Accretion tori: an overview of relevant aspects</b>	<b>23</b>
2.1 Geometrically thick accretion tori . . . . .	23
2.2 Magnetised torus . . . . .	29
2.3 Oscillation modes of relativistic tori . . . . .	30
<b>3 Method: General Relativistic MHD for axisymmetric accretion</b>	<b>39</b>
3.1 Theoretical framework for magnetised 2D models . . . . .	39
3.2 Numerical scheme for magnetised 2D models . . . . .	46
<b>4 Results: oscillations and destruction of magnetised tori</b>	<b>51</b>
4.1 Toroidal magnetic field and the runaway instability . . . . .	51
4.2 A magnetised black hole torus disrupted by stellar fly-by . . . . .	69
<b>5 Discussion</b>	<b>87</b>
<b>6 Conclusions</b>	<b>91</b>
<b>7 Future perspectives</b>	<b>93</b>
<b>Appendix</b>	<b>95</b>
<b>Bibliography</b>	<b>107</b>

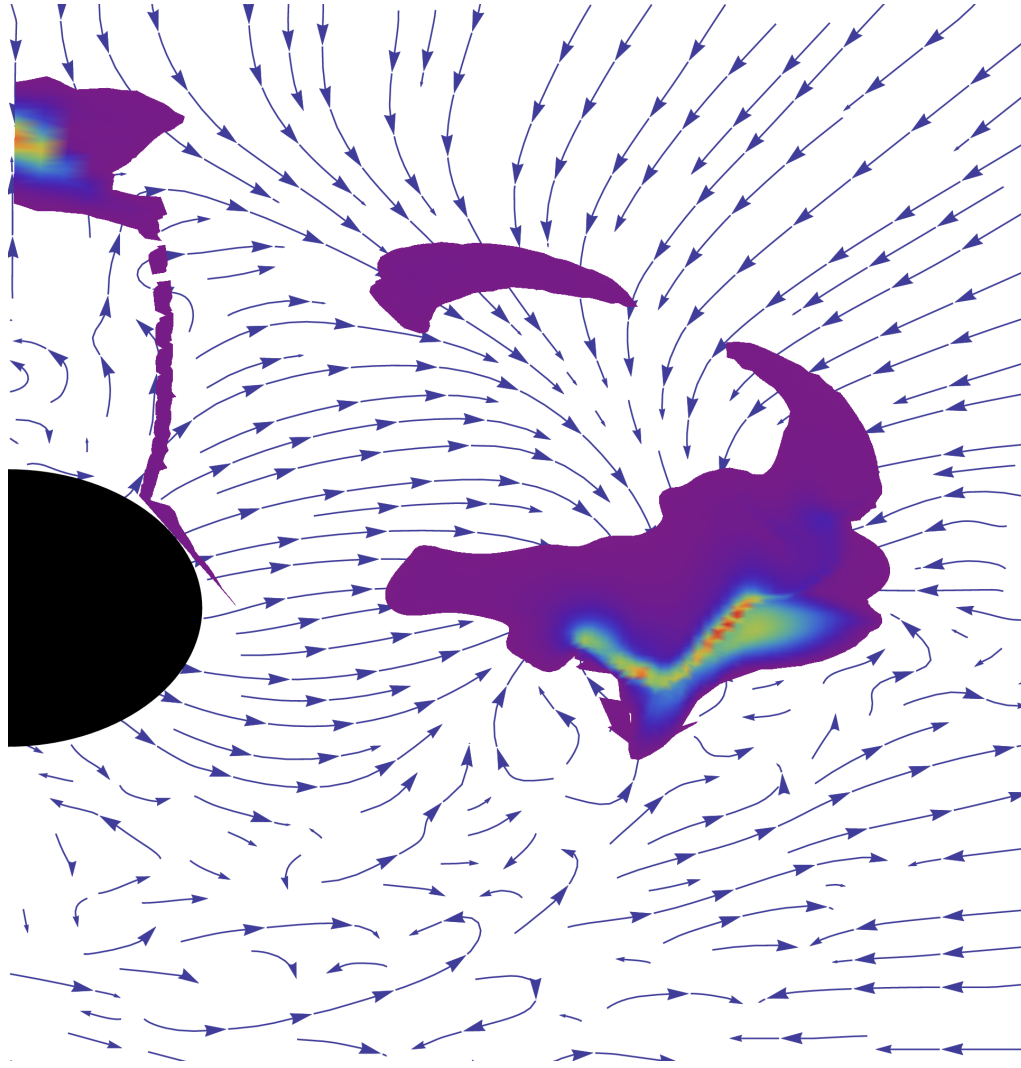


Figure 1: Snapshot of the azimuthal section across a magnetised accretion torus disrupted by a stellar fly-by event at the distance of a few gravitational radii from the rotating black hole (black circle). Part of the gaseous material (shown by the colour-coded density scale) is brought from the equatorial plane towards the rotation axis and it eventually accretes on the black hole or is ejected out of the system, along the magnetic field lines, which are also evolved together with plasma motions (see Sec. 4 for details).

# Preface

This thesis summarizes all the main results which I obtained during my PhD studies which I performed at the Astronomical Institute of the Academy of Sciences of the Czech Republic and at the Faculty of Mathematics and Physics of Charles University in Prague during the period 2011-2015. Most of these results were published in the following papers: Hamerský & Karas (2013) and Hamerský & Karas (2015). This Thesis is organized as follows. Chapter 1 is an introduction which contains the motivation for this work. First I briefly overview selected characteristics of Galactic centre, active galactic nuclei and relativistic jets relevant for our own work. I also introduce the basic results from the accretion theory that form the basis for the following investigation. Chapter 2 is an introduction to the theory of accretion tori. I focus primarily on the Abramowicz et al. (1978) model of relativistic accretion torus and on Komissarov's solution (Komissarov 2006) as its natural generalization including a large-scale toroidal magnetic field. I also give a short introduction to the study of oscillation modes of relativistic tori, which was deeply studied by Blaes et al. (2006). I present an overview of solving general relativistic magnetohydrodynamical (GRMHD) equations in the conservative scheme in Chapter 3. I discuss both theoretical and numerical schemes that are adopted by the numerical program HARM-2D (Gammie et al. 2003) which I used for my simulations.

I present our results in Chapter 4. I discuss the impact of the presence of the toroidal magnetic field on the runaway instability of relativistic accretion tori and on their oscillation properties in Section 4.1. I study also the impact of changing black hole parameters (spin and mass) and the specific angular momentum of the accreted material on the evolution of the torus. Section 4.2 discusses the scenario of star-disc hydrodynamical interactions as a feasible agent of material delivery from the inner disc into the corona. I start with the study of small oscillations, triggered by a small density perturbation, which can be treated in the linearized approximation (Blaes et al. 2006). Large perturbations, on the other hand, lead to a combination of episodic accretion and ejection. I study the influence of magnetic field strength and geometry on the outflow velocities.

Last chapters present discussion, conclusions and the view of future perspectives. An Appendix that contains derivations of important equations, which reader could appreciate for better insight, and list of symbols is at the end of the Thesis. All sources which I drew from are cited in Bibliography.

I would like to thank the Czech Science Foundation (project GAČR No. 14-37086G), Charles University in Prague (project SVV-260211) and the Grant Agency of Charles University (project No. 139810) for financial support during my study.



# 1. Introduction

## 1.1 Galactic centre and centres of other galaxies

Our discussion and the description of magnetised tori in this work can be scaled from stellar-mass to supermassive black holes (SMBH), i.e. over nine orders of magnitude in mass and size. However, for definiteness of our examples, a special prominent case of Galactic centre SMBH is particularly relevant.

Our Solar System resides in a barred spiral galaxy (Gerhard 2002). Because of its appearance as a dim glowing belt on the night sky, it got its name Milky Way. Galileo Galilei was the first who discovered that this belt consists of individual stars in 1610. Until the beginning of 20th century, it was generally thought that all stars in the Universe were situated inside the Milky Way. It was Edwin Hubble who discovered by his observations that the Milky Way is just one of many galaxies.

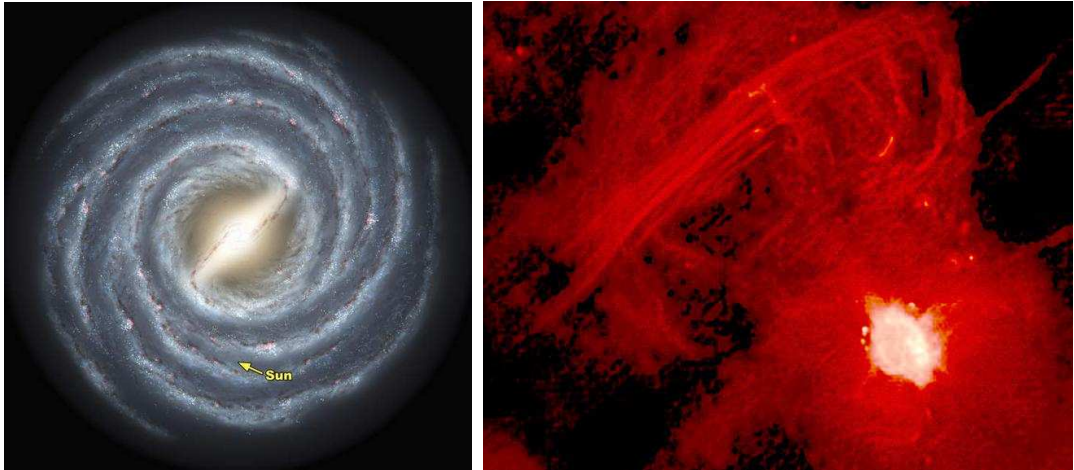


Figure 1.1: Left Panel: an artist's rendering of the Milky Way and its central bar structure, with the Sun's position noted. Credit: NASA/JPL-Caltech/R. Hurt (SSC/Caltech). Right panel: the central roughly hundred parsecs of the Galactic region in the radio band. The Galactic centre itself is the bright source. The arcs are thought to be hot gas flowing along a strong magnetic field. Credit: F. Yusef-Zadeh et al., VLA, NRAO.

The centre of the Milky Way is  $7.6 \pm 0.3$  kpc far from the Sun (Schödel et al. 2003) and it is the only nucleus of a normal spiral galaxy that can be resolved in detail by observations, which makes it exceptional amongst other galactic nuclei. However, the centre of the Milky Way is obscured by interstellar dust in the plane of the Galactic disc, which makes it impossible to observe it in visible light. Only observations in infrared, microwave, hard X-ray or  $\gamma$  rays can give us some information about features in the Galactic centre. The vast development of instruments and techniques over the last few decades caused a considerable progress in our knowledge of central parts of the Milky Way. The study of galactic cores underwent a great push forward with the deployment of Hubble

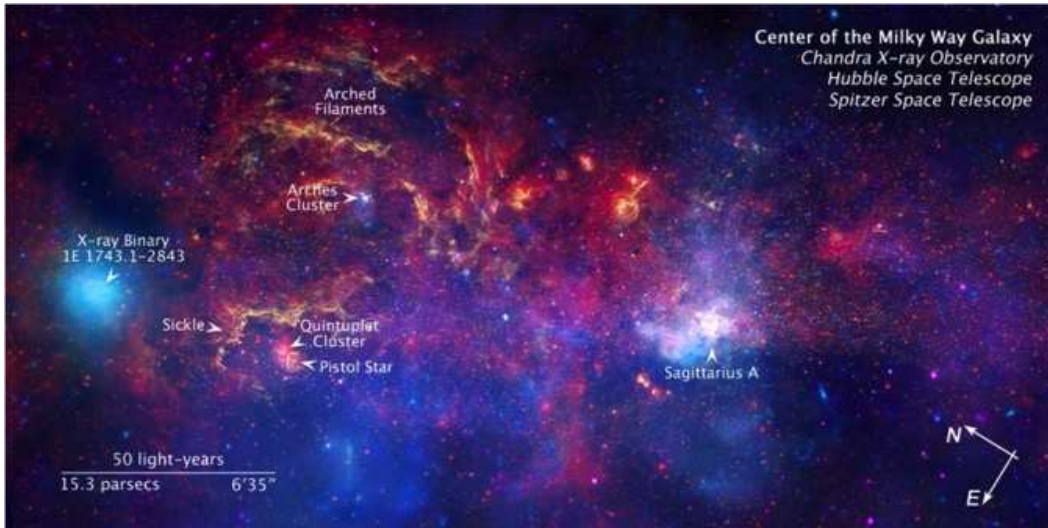


Figure 1.2: In this composit image of Galactic centre, yellow colour represents the near-infrared image of Hubble Space Telescope. Red colour represents the infrared observations of Spitzer satellite. Blue to violet colours are the X-ray image from Chandra Observatory, originating from gas heated to millions of Kelvins near the supermassive black hole. The Milky Way’s dynamical centre and the position of the supermassive black hole coincide with Sagittarius A object. Credit: NASA/JPL-Caltech/ESA/CXC/STScI.

Space Telescope which gets credit for the discovery of nuclear stellar discs, bars, dust features, irregular patches or highly organized discs.

Central light years contain a dense and luminous star cluster and ionized, extremely hot gas (Genzel et al. 1994). A very compact radio source  $SgrA^*$  (Balick & Brown 1974) is at the centre of this nuclear star cluster and ionized gas environment.  $SgrA^*$  emits also in X-ray band but this luminosity is quite modest. The motion of the material around the centre indicates the presence of a massive, compact object. This enormous concentration of mass is best explained by the existence of a supermassive black hole (SMBH) whose mass is estimated to  $(3.6 \pm 0.3)10^6 M_{\odot}$  (Schödel et al. 2003), where  $M_{\odot}$  denotes the mass of the Sun.  $SgrA^*$  is  $10^5$  times closer than the nearest quasars and, therefore, it offers the best target for observations which test the black hole paradigm. Recent millimetre, infrared and X-ray observations have detected irregular and sometimes intense outbursts of emission from  $SgrA^*$  (Baganoff 2001). It is believed that this emission comes from the synchrotron emission or the inverse Compton scattering from accelerated electrons in the innermost accretion zone of the black hole (Liu et al. 2006). Light curves of some of these flares reveal quasi-periodic behaviour. It is probably caused by an orbital motion of hot gas spots near the last circular orbit (Bélanger et al. 2006). Observations show that interstellar magnetic field is present in the Galactic centre region (Ferriere 2009). Magnetic field and especially its mutual interplay with strong gravitation is a crucial parameter determining the structure of an accretion flow. Moreover, it influences an ejecting material in the form of relativistic jets. However, the magnetization of the gas still remains

unknown.

Figure 1.2 summarizes the rich variety of different objects and processes present in our Milky Way's nucleus as a proto-typical centre of a galaxy in relative quiescence. Stars dominate the emission of the central region that is commonly called the nuclear bulge. A disc-shape region stands out clearly from the kiloparsec-scale Galactic bulge by releasing intense emission in the far-infrared spectral band. Ongoing star formation is seen in the regions of clumpy molecular gas. The nuclear bulge has the radius of about 200 pc and the scale height about  $\sim 45$  pc, with the total mass of about  $10^9 M_\odot$  (Launhardt et al. 2002).

A tight connection between central supermassive black holes and the properties of their host galaxies has been confirmed in both quiescent galaxies and active galactic nuclei (Watson et al. 2008, and further references cited therein). The strongest correlation is the  $M_\bullet - \sigma$  relation, which relates the central black hole mass  $M_\bullet$  and the bulge velocity dispersion  $\sigma$ . It supplements a similar relation between the black hole mass and luminosity of the bulge (Magorrian et al. 1998). The  $M_\bullet - \sigma$  relation was found by ranking black hole detections according to their trustfulness when the least secure cases were excluded. The correlation between  $M_\bullet$  and  $\sigma$  for the best-determined black hole masses was nearly perfect as a contrast to the much weaker correlation for the less secure masses.  $M_\bullet - \sigma$  relation brought a considerable push forward in our understanding of black hole demographics. A great outcome coming from the  $M_\bullet - \sigma$  relation was the resolution of the apparent discrepancy amongst black hole masses in nearby galaxies, the masses of black holes in AGNs and the mass density in black holes which would explain quasar light (Merritt & Ferrarese 2001). Moreover, the tightness of  $M_\bullet - \sigma$  relation indicates that some additional feedback mechanism acts to more directly connect black hole masses to stellar velocity dispersions. Otherwise, this connection would not maintain because of the mergers despite the strong correlation between black hole mass and bulge mass established in the early Universe.

Differences in observational appearance led to efforts to find a unification scheme of active galactic nuclei. The basic idea of the standard unification scheme is that AGNs are an asymmetric and anisotropic system (Urry & Padovani 1995). Since it is inevitable that a rotating system finds a preferential axis in space, it is a natural assumption. The orientation of the AGN rotation axis with respect to our line of sight is, therefore, an important parameter. Merloni et al. (2003) quantified the degree of correlation amongst radio luminosity, X-ray luminosity and a black hole mass. He fitted the data and obtained well constrained values for the correlation coefficients. He found that (both stellar mass and supermassive) black holes lie preferentially on a plane which is called the fundamental plane of black hole activity. This relation amongst radio luminosity, X-ray luminosity and a black hole mass is not influenced significantly by obscuration and beaming. Hence, this relation does not depend on orientation and, therefore, is supplementary to the standard unification scheme.

## 1.2 AGN and jets

We know from observations that the central region shines more than all stars in the galaxy itself in some galaxies. The spectrum is different from those produced by stars and the emission is bright at all wavelengths. The luminosity varies on very short timescales, which means that the size of the central region must be very small. Since the most efficient conversion of matter to energy is the accretion by a black hole, it is certain that it is a SMBH which causes the emission.

An active galactic nucleus (AGN) is defined as a compact region at the centre of the galaxy whose luminosity is much higher than that of an average galaxy. There is a number of AGN types, sorted according to their brightnesses and classification schemes. It is common to divide AGNs into two classes: radio-quiet and radio-loud. Radio-loud objects are characterized by emission which is dominated by a contribution from a jet. On the other hand, radio-quiet objects are simpler because the jet-related emission can be neglected.

The Milky Way is not an AGN, at least not in its present stage. Although it contains a SMBH, it is not very bright because of the lack of accretion. Radio-loud AGNs emit most of their energy over the entire electromagnetic spectrum non-thermally through powerful relativistic jets. The opposite case is the emission of radio-quiet AGNs which is dominantly thermal and related to the accretion disc (Bonzini et al. 2013).

Relativistic jets in AGNs are one of the most energetic events observed in the Universe. They are extremely powerful bursts of plasma launched from inner regions of some AGNs. Their lengths reach distances up to hundreds of kiloparsecs. Figure 1.3 shows the schematic model of AGN. We observe relativistic jets not only in AGNs but also in microquasars. Nonrelativistic jets, on the other hand, are evidenced around young stars. They indicate the activity of compact astrophysical sources and represent the universal and efficient mechanism of the energy release. However, a lot of questions about the origin of jets still remain unanswered. For example, it is not clear why jets are present only in some particular systems, what the correlation between the jet power and the black hole spin is and how magnetic fields influence a jet formation and its collimation. We know from observations that jets can be accelerated and collimated in the vicinity of a black hole (Junor & Biretta 1995). They can be accelerated up to relativistic velocities in AGNs and keep these velocities to kiloparsec distances.

It is believed that the accretion of interstellar mass and gas from tidally disrupted stars onto a black hole as well as magnetic fields play a crucial role in the process of jet formation. Magnetised accretion discs can drive jets under certain circumstances (Lovelace 1976; Blandford & Payne 1982) as well as a spinning black hole threaded by magnetic field supported by currents in external gas (Blandford & Znajek 1977). Blandford-Znajek mechanism is essential to the spin paradigm which tries to find a relation between the presence of a fast jet and a black hole spin. However, it does not cause any collimation, hence, there must exist some additional mechanism which confines the outflow.

The matter of a jet comes either from electron-positron pair production or from baryonic matter from the disc. Theoretical and observational considerations

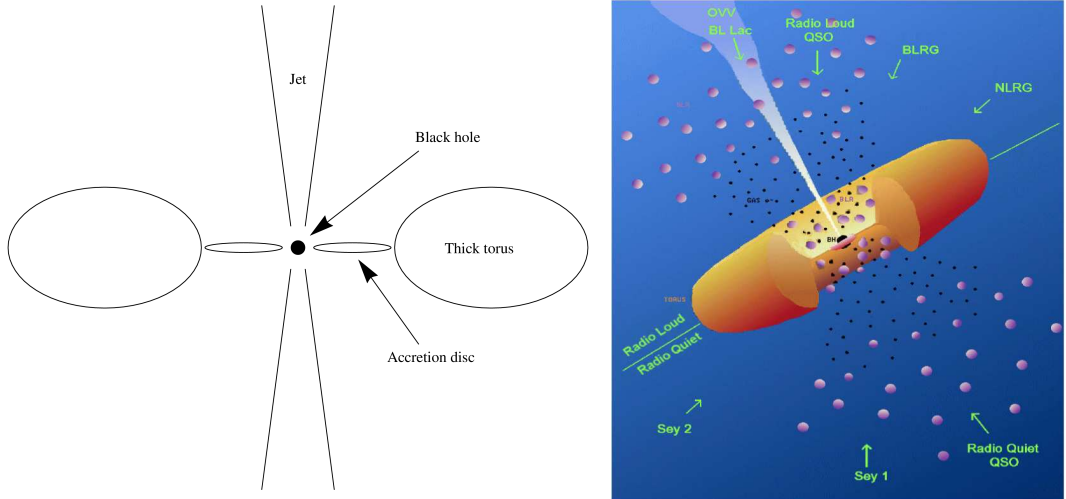


Figure 1.3: Left image: a schematic illustration of radio-loud AGN. At the centre of the galaxy there is a supermassive black hole that is surrounded by thin inner accretion disc and dusty thick torus. The material in the form of jet is expelled along the spin axis. Right image: a schematic picture of AGN (credit: Urry & Padovani (1995)). OVV = Optically Violent Variables, BL Lac = BL Lac objects, QSO = quasars, BLRG = Broad Line Region Galaxies, NLRG = Narrow Line Region Galaxies, Sey = Seyfert galaxies. The particular type of AGN is defined by the view angle of an observer.

suggest that jets must remain Poynting dominated along the acceleration phase (Agudo 2015). The particle acceleration process, which is responsible for maintaining power-law distribution of radiating ultra-relativistic electrons over sub-pc to pc scales, is not yet understood. In the case of low plasma magnetization, the most efficient way of energizing jet particles is a diffusive acceleration that takes place at the fronts of strong hydrodynamical shocks (Summerlin & Baring 2012). Relativistic magnetic reconnection and stochastic interactions of particles with magnetic turbulences are supposed to play the key role in the acceleration of particles for high magnetization case (Stawarz & Petrosian 2008).

We know from observations of radio-loud objects that jet power correlates with the accretion rate (Sbarrato et al. 2012). Consequently, powerful jets are associated with high rates of accretion (Ghisellini et al. 2010).

### 1.3 Accretion with angular momentum (fluid tori)

Accretion is a possible reservoir of a huge amount of energy and it powers the most energetic phenomena in the Universe (Frank et al. 2002). In order to reveal some basic principles of accretion, let us assume a body of mass  $M$  and radius  $R_\star$ . In Newtonian physics the gravitational energy released by the fall of the body of mass  $m$  from infinity onto its surface is

$$\Delta E_{acc} = \frac{GMm}{R_\star}, \quad (1.1)$$

from which we see that the amount of energy release depends on  $\frac{M}{R_\star}$ . This ratio is highest for neutron stars and black holes. If we assume that all of the energy released by falling matter onto a solid surface is converted into radiation and the accretion rate is  $\dot{M}$ , we get the accretion luminosity

$$L_{acc} = \frac{GM\dot{M}}{R_\star}. \quad (1.2)$$

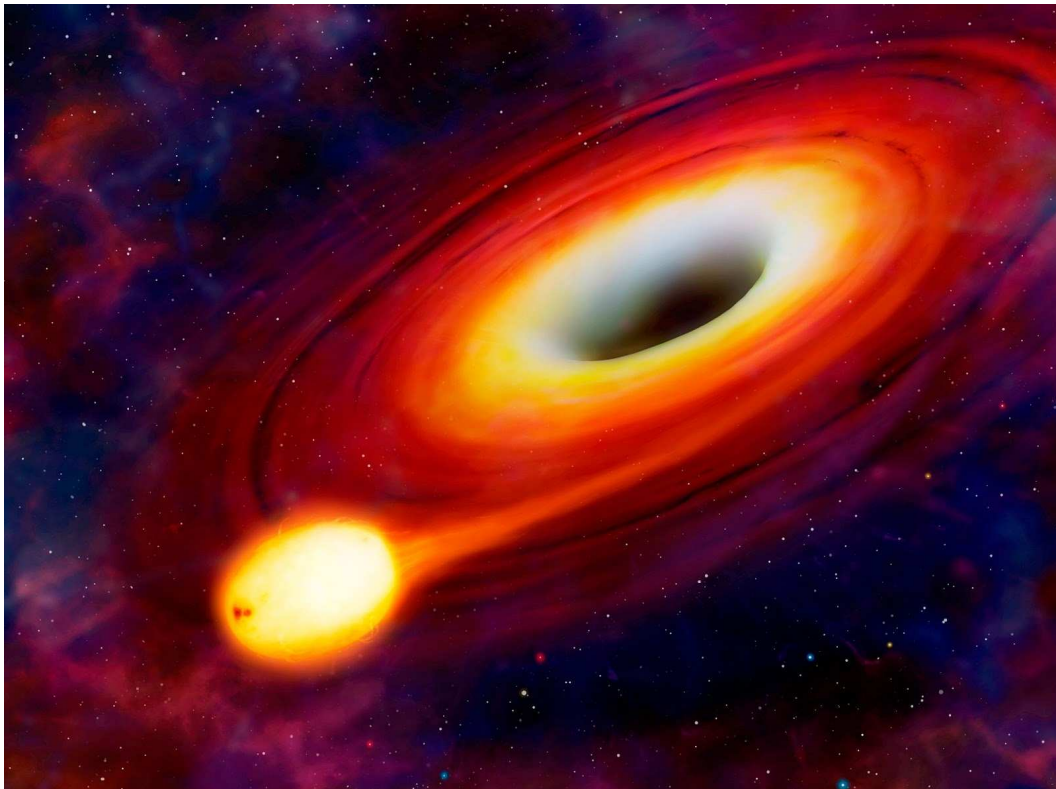


Figure 1.4: An artist impression of the tidal disruption of a star creating an accretion torus around a central black hole. Source: <http://www.media.inaf.it/>

When the central object has no solid surface, which is the case for black holes, some part of the accreted material can pass through the event horizon and contribute to the black hole energy instead of producing radiation. In this sense we must alter equation (1.2) by introducing a dimensionless accretion efficiency  $\eta$  by

$$L_{acc} = \frac{2\eta GM\dot{M}}{R_\star}. \quad (1.3)$$

When we replace  $R_\star$  with the Schwarzschild radius we obtain

$$L_{acc} = \eta\dot{M}c^2, \quad (1.4)$$

where  $c$  is the speed of light and a dot denotes a time derivative.

The simplest astrophysical accretion problem is steady, spherically symmetric accretion onto a star (Hoyle & Lyttleton 1939; Bondi 1952). It is a reasonable

approximation to a star accreting from a gas cloud or an interstellar medium. Moreover, it provides a useful upper estimation of the accretion rate onto a star. Let us assume a steady flow. Then we can write for the accretion rate

$$\dot{M} = -4\pi r^2 \rho v, \quad (1.5)$$

where  $\rho v$  is an inward flux. If we assume that all the material within a distance of  $r_{acc}$  is accreted by a star, then we can write

$$\dot{M} = -4\pi r_{acc}^2 \rho v. \quad (1.6)$$

The size of  $r_{acc}$  can be determined by two extreme conditions. The first one is when the motion of the star in the gas is supersonic and the second one is when the star is at rest with respect to the gas. We get  $r_{acc} \sim \frac{2GM}{v^2}$  for the first case (Hoyle & Lyttleton 1939) and  $r_{acc} \sim \frac{2GM}{c_S^2}$  for the second case (Bondi 1952), where  $c_S$  is the sound speed in the gas. Consequently, we can write two expressions for the accretion rate:

$$\begin{aligned} \dot{M} &= -4\pi\rho \frac{(GM)^2}{v^3}, \\ \dot{M} &= 4\pi\rho \frac{(GM)^2}{c_S^3}. \end{aligned} \quad (1.7)$$

As a trade-off between these two extremes Bondi (1952) proposed an interpolation formula

$$\dot{M} = 4\pi\rho \frac{(GM)^2}{(\Delta v^2 + c_S^2)^{\frac{3}{2}}}, \quad (1.8)$$

where  $\Delta v$  is the relative velocity between the star and the gas. The equations above are valid only if the accreted gas has no angular momentum. Otherwise, the non-zero specific angular momentum would make the gas orbit around the star (central object), which would lead to the formation of an accretion disc. For the specific angular momentum of a body in the orbit of radius  $R$  around the central body of mass  $M$  we can write

$$l = \sqrt{GMR}, \quad (1.9)$$

where  $G$  is the gravitational constant. When a body moves towards the central object, i.e. the distance  $R$  decreases, its angular momentum decreases too. Because of the fact that the total angular momentum is conserved, we deduce that the loss of the angular momentum via mass accretion has to be recouped by the enhancement of the angular momentum of the material in the outer disc. It means that the material can be accreted only if some amount of the angular momentum is transported outwards.

During deriving equations (1.2) and (1.4), the effect of radiation was not taken into account. The radiation pressure sets a limit for  $\dot{M}$ . If we assume that the accreted material consists only of ionised hydrogen, the gravitational force on electron-proton pairs is

$$F_{grav} = \frac{GM(m_p + m_e)}{r^2} \sim \frac{GMm_p}{r^2}, \quad (1.10)$$

where  $m_p$  and  $m_e$  are the proton mass and the electron mass. While the gravitational force is attractive, the force of the radiation pressure pushes ions outward. Thomson scattering is the main agent through which the radiation pressure affects electrons. Electrons drag protons outward thanks to the attractive Coulomb force. The radiation force acting on electrons is equal to

$$F_{rad} = \frac{L\sigma_T}{4\pi cr^2}, \quad (1.11)$$

where  $\sigma_T$  is the Thomson scattering cross-section for electrons and  $L$  is luminosity. If we prescribe an equality between (1.10) and (1.11) we get the value of luminosity at which the gravitational force and the radiative force are equal:

$$L_{\text{Edd}} = \frac{4\pi GMm_p c}{\sigma_T} \sim 1.3 \cdot 10^{38} \left( \frac{M}{M_\odot} \right) \text{ erg s}^{-1}. \quad (1.12)$$

We call this luminosity value the Eddington limit. It puts a constraint on the value of the accretion rate. Using equations (1.3) and (1.12) we get the expression for the mass accretion rate at the Eddington limit for the case when the central object is a black hole,

$$\dot{M}_{\text{Edd}} = \frac{1.3 \cdot 10^{38}}{\eta c^2} \frac{M}{M_\odot} g s^{-1}. \quad (1.13)$$

If the material which is gravitationally captured by a massive object has a non-zero angular momentum, it is not accreted immediately but it forms an accretion disc. The accretion disc orbits around the central object with a characteristic angular velocity. The mass of the accretion disc is typically much smaller than the mass of the central body and, accordingly, the self-gravity of the accretion disc can be neglected. Consequently, the disc orbits the central body with a Keplerian angular velocity

$$\Omega_K(R) = \sqrt{\frac{GM}{R^3}}, \quad (1.14)$$

where  $M$  is the mass of the central body and  $R$  is the distance from the central body. One can see that the closer the material orbits the higher angular velocity it has. When two neighbouring annuli slide past each other, random thermal motions of the gas result in an angular momentum transport perpendicular to the circular velocity of the gas. We call this process the shear viscosity.

Let us consider the speed of random motions  $\tilde{v}$  and the typical length scale between interacting elements  $\lambda$ . Then the kinematic viscosity is equal to

$$\nu = \lambda \tilde{v}. \quad (1.15)$$

The large shear viscosity is necessary for the angular momentum transport during the lifetime of an accretion disc. However, the question about the origin of viscosity remains unanswered and it is still a source of scientific debates. If the fluid is dominated by viscous forces, the Reynolds number is less than one. The Reynolds number for an accretion disc was calculated to be as high as  $10^{14}$ . It seems that molecular collisions are insufficient to provide the needed shear viscosity. We can assign the critical value of the Reynolds number to every

system. This value makes a boundary between laminar and turbulent motions. The large values obtained for accretion discs reveal the fact that the material motion in an accretion disc is turbulent, which is a conceivable source of the shear viscosity. Adopting the idea that turbulence is the source of the shear viscosity in accretion discs, we can write

$$\nu_{turb} = \lambda_{turb} v_{turb}, \quad (1.16)$$

where  $\lambda_{turb}$  and  $v_{turb}$  are the size and the velocity of the largest turbulent motion. However, a complete description of turbulence is still elusive. Shakura & Sunyaev (1973) parametrised all the ignorance involving turbulence in their relation

$$\nu = \alpha c_S H, \quad (1.17)$$

which is known as the  $\alpha$ -prescription of the shear viscosity. They proposed that the largest turbulent motions cannot exceed the height of the disc  $H$ , the motions cannot be supersonic and, accordingly, the maximum possible speed is the sound speed in the gas  $c_S$ . Equation (1.17) is elegant and useful prescription for the shear viscosity, which also brought an effort to experimentally determine the value of  $\alpha$  whose magnitude is expected to be  $\leq 1$ . However, the physical mechanism explaining viscosity is still uncertain. The magnetorotational instability (Balbus & Hawley 1991) is currently the favoured model to explain the origin of viscosity in accretion discs. Consider a rotating disc in the presence of the vertical magnetic field. Two neighbouring fluid elements behave as if they were connected by a spring. In fact, it is the magnetic tension which is responsible for this “spring-like” behaviour. The inner fluid element has a larger velocity than the outer element in the case of a Keplerian disc, which makes the spring stretch. Accordingly, the inner fluid element is slowed down by the spring which reduces its angular momentum and make it move to a lower orbit. On the other hand, the outer fluid element is accelerated by the spring. It increases its angular momentum and, therefore, moves up to higher orbits. It is hoped that this feature could provide the necessary viscosity to explain the observed accretion rates in accretion discs.

Let us now have a look at the mechanism by which the ring of matter spreads out due to viscous forces. Conceive of two bodies orbiting at distances  $R$  and  $R + dR$  as figure 1.5 shows. Element 1 carries, on average, the angular momentum equivalent to the position of  $R + dR$  and element 2 possesses the angular momentum equivalent to the position of  $R$ :

$$\begin{aligned} l_1 &= (R + dR)^2 \Omega(R + dR), \\ l_2 &= R^2 \Omega(R). \end{aligned} \quad (1.18)$$

If these two gas elements exchange their positions, they carry different amounts of angular momentum:

$$\begin{aligned} l_1 &= R(R + dR)\Omega(R + dR), \\ l_2 &= (R + dR)R\Omega(R). \end{aligned} \quad (1.19)$$

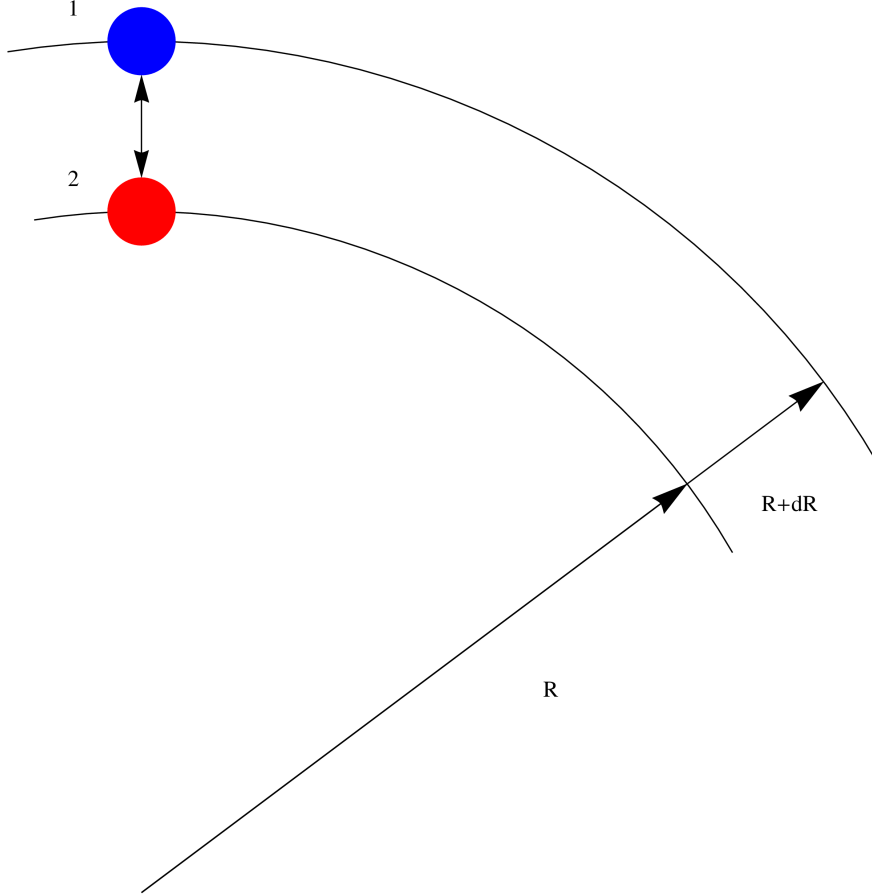


Figure 1.5: Illustration of the situation when two bodies exchange their positions: basic concept for the discussion of angular momentum transport in accretion discs.

A chaotic motion leads to the fact that the material passes through the surface  $R + \frac{1}{2}dR$  equally in both directions. The mass flux is the same in both directions and its value is of the order  $H\rho\tilde{v}$ . However, it is not true for the angular momentum. This disbalance results in a transport of angular momentum

$$\Delta l = R(R + dR)[\Omega(R + dR) - \Omega(R)]. \quad (1.20)$$

This difference between outward and inward angular momentum fluxes gives rise to the torque. The total angular momentum flux through the radius  $R$  is

$$\begin{aligned} G(R) &= 2\pi RH\rho\tilde{v}R(R + dR)[\Omega(R + dR) - \Omega(R)] \\ &= 2\pi R\nu\Sigma R^2\Omega', \end{aligned} \quad (1.21)$$

where  $\nu = \tilde{v}dR$  and the dash denotes the derivative according to  $R$ . The surface density  $\Sigma$  is defined for the constant  $\rho$  as

$$\Sigma \equiv \int_0^H \rho dz = \rho H. \quad (1.22)$$

Let us emphasise that for the case of the Keplerian angular velocity  $\Omega_K$ , the derivative  $\Omega'_K$  is always negative, though, we conclude from equation (1.21) that

the inner edge of the annulus loses the angular momentum in behalf of the outer annulus. The difference between the angular momentum fluxes at inner and outer edges of the annulus results in the total torque

$$G(R + dR) - G(R) = \frac{\partial G}{\partial R} dR. \quad (1.23)$$

This torque is acting in the presence of the angular velocity  $\Omega(R)$  and so we get for the power of the torque following relation:

$$P = \Omega \frac{\partial G}{\partial R} dR = \left[ \frac{\partial}{\partial R} (G\Omega) - G\Omega' \right] dR, \quad (1.24)$$

where the term  $G\Omega' dR$  denotes the rate at which the mechanical energy is dissipated and locally heats the gas as we can see from the equation of energy flux:

$$\begin{aligned} \dot{E} &= \int_{R_{in}}^{R_{out}} \left( \frac{\partial}{\partial R} (\Omega G) - G\Omega' \right) dR \\ &= (\Omega G)_{R_{out}} - (\Omega G)_{R_{in}} - \int_{R_{in}}^{R_{out}} G\Omega' dR, \end{aligned} \quad (1.25)$$

where the last term is equal to  $\int_S 2D(R) dS$  if we define the dissipation rate per unit surface area as

$$D(R) \equiv \frac{G\Omega'}{4\pi R} = \frac{1}{2} \nu \Sigma (R\Omega')^2, \quad (1.26)$$

where we used equation (1.21), and every ring has a surface area  $dS = 2 \times 2\pi R dR$ . Assuming a Keplerian velocity we get

$$D(R) = \frac{9}{8} \nu \Sigma \frac{GM}{R^3}. \quad (1.27)$$

Let us consider a thin disc orbiting in a Keplerian orbit around the central body of the mass  $M$ . The velocity of the disc is

$$v_\varphi = R\Omega_K(R). \quad (1.28)$$

Moreover, there can be also a small radial drift velocity  $v_r$  which reaches negative values for small  $R$  as a consequence of the matter falling towards the body. For the mass comprised inside a disc annulus of width  $\lambda$  we can write

$$\Delta m = 2\pi R \Sigma \lambda. \quad (1.29)$$

The angular momentum of the annulus is equal to  $2\pi R \Sigma R^2 \Omega_K \lambda$ . The rate of the change of mass inside the annulus is (Frank et al. 2002; Blaes 2014)

$$\frac{\partial}{\partial t} (2\pi R \Sigma) = v_r(R, t) 2\pi R \Sigma(R, t) - v_r(R + \lambda, t) 2\pi (R + \lambda) \Sigma(R + \lambda, t), \quad (1.30)$$

which in the limit  $\lambda \rightarrow 0$  reduces to

$$R \frac{\partial \Sigma}{\partial t} + \frac{\partial}{\partial R} (R \Sigma v_r) = 0. \quad (1.31)$$

If we consider the non-zero angular momentum we have to also include net effects of viscous torques. Then we can write

$$\begin{aligned} \frac{\partial}{\partial t}(2\pi R\lambda\Sigma R^2\Omega_K) &= v_r(R, t)2\pi R\Sigma(R, t)R^2\Omega_K(R) \\ &\quad - v_r(R + \lambda, t)2\pi(R + \lambda)\Sigma(R + \lambda, t) \\ &\quad \times (R + \lambda)^2\Omega_K(R + \lambda) + \frac{\partial G}{\partial R}\lambda, \end{aligned} \quad (1.32)$$

which reduces in the limit  $\lambda \rightarrow 0$  to

$$R\frac{\partial}{\partial t}(\Sigma R^2\Omega_K) + \frac{\partial}{\partial R}(R\Sigma v_r R^2\Omega_K) = \frac{1}{2\pi} \frac{\partial G}{\partial R}. \quad (1.33)$$

Using equations (1.21), (1.31) and (1.33) we obtain

$$\frac{\partial \Sigma}{\partial t} = \frac{3}{R} \frac{\partial}{\partial R} \left( \sqrt{R} \frac{\partial}{\partial R} (\nu \Sigma \sqrt{R}) \right), \quad (1.34)$$

which is the basic equation that describes the time evolution of the surface density in a Keplerian disc. An assumption of constant  $\nu$  enables a simple analytic solution. Adopting an initial mass distribution in the form

$$\Sigma(R, t = 0) = \frac{m}{2\pi R_0} \delta(R - R_0), \quad (1.35)$$

i.e. a ring of matter at radius  $R_0$ , Frank et al. (2002) derived an expression for the surface density

$$\Sigma(x, \tau) = \frac{m}{\pi R_0^2} \tau^{-1} x^{-\frac{1}{4}} e^{-\frac{(x^2+1)}{\tau}} I_{\frac{1}{4}}\left(\frac{2x}{\tau}\right), \quad (1.36)$$

where  $x = \frac{R}{R_0}$ ,  $\tau = 12\nu t R_0^{-2}$  and  $I_{\frac{1}{4}}$  is a modified Bessel function. The disc viscosity causes spreading of the ring on a time scale

$$t_{visc} \sim \frac{R^2}{\nu}. \quad (1.37)$$

After a long time,  $\tau > 1$ , the majority of the disc mass is accreted onto the central object. Angular momentum of the disc material is transferred outward to a large radii. This is the basic principle lying behind all accretion discs, either those around stellar black holes or black holes in AGNs.

## 1.4 Role of small-scale magnetic fields (MRI)

MHD turbulence is relevant to generate viscosity and drive the disc accretion. The onset of MHD turbulence is inevitable as soon as the gas and the magnetic field are coupled and that the Maxwell stress dominates plasma motions. Magneto-rotational instability is a linear instability. As such it can be understood analytically, but the non-linear turbulent state can be explored only with numerical

simulations. A number of codes have been developed: ZEUS (Stone & Norman 1992), HARM (Gammie et al. 2003), the general relativistic MHD (GRMHD) code of De Villiers & Hawley (2003), COSMOS++ (Anninos et al. 2005), and ATHENA (Stone et al. 2008). Energy advection plays a key role in hot accretion flows, and so it is important to ensure accurate conservation of energy by the numerical code. We use the numerical code HARM-2D for our simulations, hence, we are not able to investigate non-axisymmetric features. However, an axisymmetric model of MRI is a useful simplification of the general case of non-axisymmetric MRI because it can reveal interesting aspects of the studied system in a simplified manner (Masada & Sano 2008; Pino & Mahajan 2008).

Magneto-rotational instability is a feasible candidate for the explanation of the origin of turbulent flows in astrophysical accretion discs (Balbus & Hawley 1991). In a magnetised, perfectly conducting fluid, the magnetic forces cause that elements of the fluid behave as if they were connected with elastic springs.

In order to see this behaviour, consider the equations of motion for a fluid element in a circular motion with an angular velocity  $\vec{\Omega}$  which is, in general, the function of the distance from the rotation axis  $R$ . The centripetal force needed to keep the mass in its orbit is  $-R\Omega^2(R)$ . Since this force comes from the gravitational attraction of the point mass in the centre, the centripetal acceleration is  $-GM/R^2$ , where  $M$  is the central mass. Let us now conceive of small deviations from the circular motion of the orbiting mass element, caused by some perturbing force. It is convenient to transform the variables into a rotating frame moving with the orbiting mass element at the angular velocity  $\vec{\Omega}(R_0) = \vec{\Omega}_0$  (see figure 1.6), where the subscript 0 refers to the initial unperturbed orbit.

The relation between accelerations with respect to the rotation frame  $\vec{a}_R$  and with respect to the frame constant in space  $\vec{a}_C$  is

$$\vec{a}_C = \vec{a}_R + \dot{\vec{\Omega}}_R \times \vec{R} + 2\vec{\Omega} \times \vec{v}_R + \vec{\Omega} \times (\vec{\Omega} \times \vec{R}), \quad (1.38)$$

where  $\vec{v}_R$  is the velocity with respect to the rotating frame. In the frame constant in space the equations of motion are (see figure 1.6):

$$\begin{aligned} \ddot{X} &= -R\Omega^2(R) \cos(\Omega t) + f_X, \\ \ddot{Y} &= -R\Omega^2(R) \sin(\Omega t) + f_Y. \end{aligned} \quad (1.39)$$

Taking into account equation (1.38) and considering that  $\dot{\vec{\Omega}}_R = 0$ , we get equations of motion in the rotating frame:

$$\begin{aligned} \ddot{x} &= -R\Omega^2(R) + 2\Omega_0\dot{y} + \Omega_0^2 R + f_x = 2\Omega_0\dot{y} - xR\frac{d\Omega^2}{dR} + f_x, \\ \ddot{y} &= -2\Omega_0\dot{x} + f_y, \end{aligned} \quad (1.40)$$

where we used  $R[\Omega_0^2 - \Omega^2(R_0 + x)] \simeq -xR\frac{d\Omega^2}{dR}$  and we restricted ourselves to a small neighbourhood near  $R_0$ . We can set the external forces  $f_x$  and  $f_y$  to zero and search the solution with the time dependence  $e^{i\omega t}$ . Deriving equation (1.40) we obtain:

$$\ddot{x} = -4\Omega_0^2\dot{x} - \dot{x}R\frac{d\Omega^2}{dR}$$

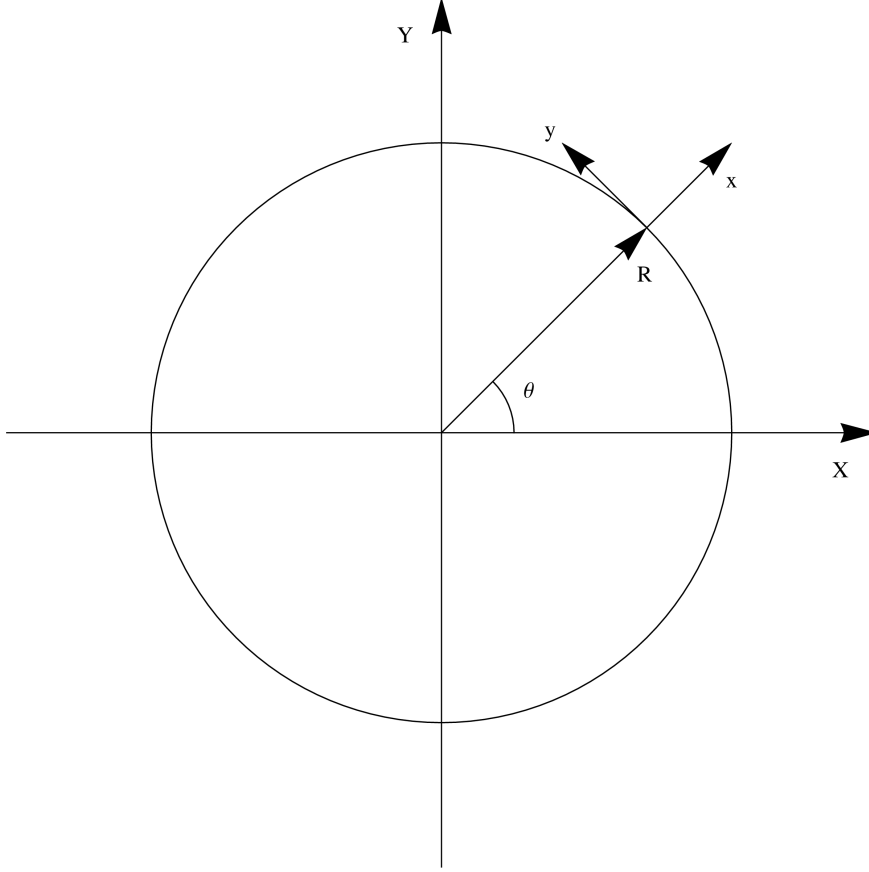


Figure 1.6: Rotating frame orbiting with angular velocity  $\Omega_0$ , denoted by lower-case letters, and the frame constant in space, denoted by upper-case letters.

$$\begin{aligned}
 -i\omega^3 x &= -4\Omega_0^2 i\omega x - i\omega x R \frac{d\Omega^2}{dR} \\
 \omega^2 &= 4\Omega_0^2 + R \frac{d\Omega^2}{dR} \equiv \kappa^2,
 \end{aligned}
 \tag{1.41}$$

where  $\kappa$  is the epicyclic frequency.

Consider now the equations of motion if the mass element is influenced by an external force:  $f_x = -Kx$ ,  $f_y = -Ky$ , where  $K$  is an arbitrary constant. This force could be exerted, for example, by a tight spring. Figure 1.7 schematically illustrates this situation. Then we solve two equations:

$$\ddot{x} = 2\Omega_0 \dot{y} - xR \frac{d\Omega^2}{dR} - Kx$$

and

$$\ddot{y} = -2\Omega_0 \dot{x} - Ky.
 \tag{1.42}$$

If we seek again the solution for the displacements  $x$  and  $y$  with the time dependence  $e^{i\omega t}$ , we get more complex equations for  $\omega$ :

$$-\omega^2 x = 2\Omega_0 i\omega y - xR \frac{d\Omega^2}{dR} - Kx$$

and

$$-\omega^2 y = -2\Omega_0 i \omega x - Ky. \quad (1.43)$$

From the second equation we can evaluate  $y$ :  $y = \frac{2\Omega_0 i \omega x}{\omega^2 - K}$  and solve the first equation:

$$\begin{aligned} \omega^2 &= \frac{4\Omega_0^2 \omega^2}{\omega^2 - K} + \left( K + R \frac{d\Omega^2}{dR} \right) \\ \omega^4 - (2K + \kappa^2)\omega^2 + K \left( K + R \frac{d\Omega^2}{dR} \right) &= 0, \end{aligned} \quad (1.44)$$

where we used the definition of  $\kappa$  in equation (1.41). Although the spring exerts an attractive force, it may destabilize. If we assume that the spring constant  $K$  is sufficiently weak, then the dominant balance will be between the final two terms on the left side of equation (1.44). A decreasing outward angular velocity profile will produce negative values for  $\omega^2$ , and both positive and negative imaginary values for  $\omega$ . The negative imaginary root results in an exponential growth of initially very small displacements. A weak spring, therefore, causes instability and a strong spring, on the other hand, produces oscillations.

If we want to understand how the MRI works, we must investigate the conditions inside a moving perfectly conducting fluid. This is usually a good approximation to astrophysical features. A moving conductor responds in order to eliminate the Lorentz force on free charges if permeated by a magnetic field  $\vec{B}$ . The magnetic force acts so as to locally rearrange these charges to produce an external electric field  $\vec{E} = -\vec{v} \times \vec{B}$ . Consequently, the direct Lorentz force on the charges,  $\vec{E} + \vec{v} \times \vec{B}$ , vanishes. In other words, the electric field in the local rest frame of moving charges vanishes. This induced electric field can now induce further changes in the magnetic field  $\vec{B}$  according to Faraday's law:

$$-\vec{\nabla} \times \vec{E} = \frac{\partial \vec{B}}{\partial t} \quad (1.45)$$

or

$$\vec{\nabla} \times (\vec{v} \times \vec{B}) = \frac{\partial \vec{B}}{\partial t}. \quad (1.46)$$

We can rewrite this equation if we realize that within the time interval  $\delta t$  the fluid makes a displacement  $\vec{\xi} = \vec{v} \delta t$ . Then we get

$$\delta \vec{B} = \vec{\nabla} \times (\vec{\xi} \times \vec{B}). \quad (1.47)$$

When we use the vector calculus identity and suppose that  $\vec{\xi}$  is a divergence-free displacement, we get

$$\begin{aligned} \vec{\nabla} \times (\vec{\xi} \times \vec{B}) &= \epsilon_{ijk} \frac{\partial}{\partial x_j} \epsilon_{klm} (\xi_l B_m) \\ &= (\delta_{il} \delta_{jm} - \delta_{im} \delta_{jl}) \frac{\partial}{\partial x_j} (\xi_l B_m) = \frac{\partial}{\partial x_m} (\xi_i B_m) - \frac{\partial}{\partial x_l} (\xi_l B_i) \\ &= (\vec{B} \cdot \vec{\nabla}) \vec{\xi} + \vec{\xi} (\vec{\nabla} \cdot \vec{B}) - \vec{B} (\vec{\nabla} \cdot \vec{\xi}) - (\vec{\xi} \cdot \vec{\nabla}) \vec{B} \\ &= (\vec{B} \cdot \vec{\nabla}) \vec{\xi} \end{aligned} \quad (1.48)$$

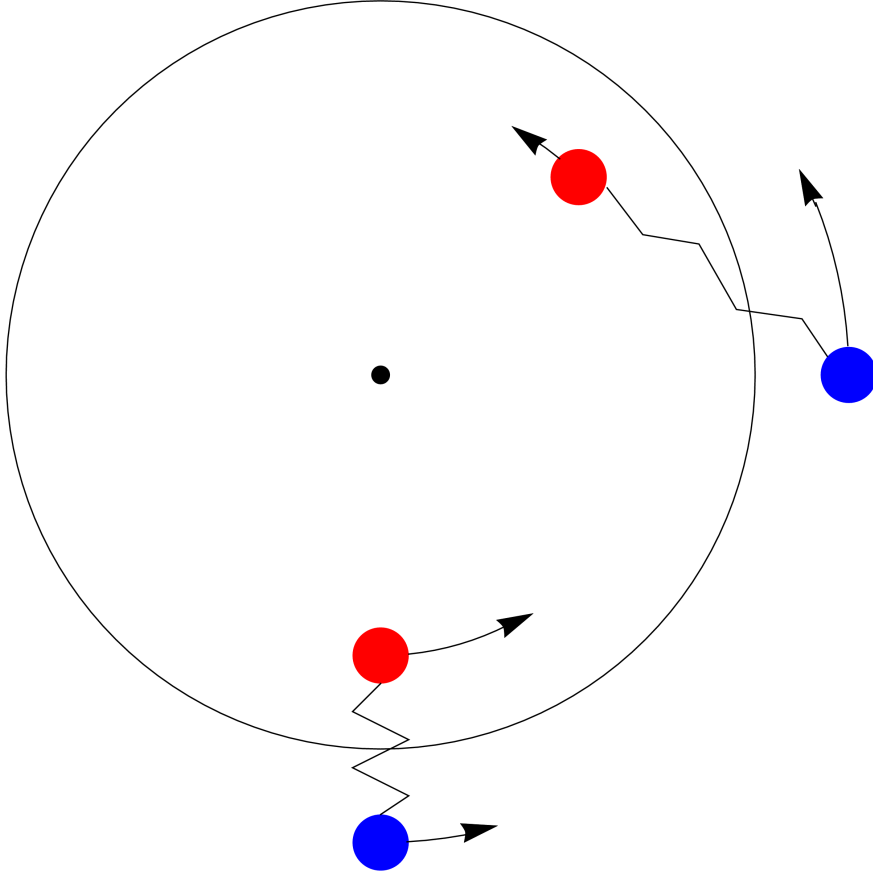


Figure 1.7: Two bodies orbiting the central object are connected by a tight spring: a useful analogy for the description of MRI. Since the inner body has a larger velocity than the outer body it causes bigger tense in the spring. Consequently, the inner body is decelerated and the outer body accelerated.

because  $\vec{\nabla} \cdot \vec{B} = 0$  thanks to Maxwell's equations and  $(\vec{\xi} \cdot \vec{\nabla})\vec{B} = 0$  because  $\vec{B}$  is assumed to be nearly constant. In order to get a better insight into the MRI, it is convenient to consider the case of uniform  $\vec{B}$  in vertical direction  $z$  and displacement  $\vec{\xi}$  which varies as  $e^{ikz}$ . Then we can write

$$\delta\vec{B} = ikB\vec{\xi}. \quad (1.49)$$

The magnetic force per unit volume is proportional to  $\vec{J} \times \vec{B}$  and Ampere's law gives  $\mu_0\vec{J} = \vec{\nabla} \times \vec{B}$  in the MHD approximation. The force per unit volume is, therefore,

$$\left(\frac{1}{\mu_0}\right) (\vec{\nabla} \times \vec{B}) \times \vec{B} = -\vec{\nabla} \left(\frac{B^2}{2\mu_0}\right) + \left(\frac{1}{\mu_0}\right) (\vec{B} \cdot \vec{\nabla})\vec{B}, \quad (1.50)$$

where we used the same vector calculus identity as in equation (1.48). It is worth emphasising that this equation is fully general with no assumptions about the strength or direction of the magnetic field. The first term on the right is analogous to a pressure gradient which can be neglected in this case because it

exerts no force in the plane of the disc (perpendicular to  $z$ ). The second term on the right acts like a magnetic tension force, analogous to a taut string. For a small disturbance  $\delta\vec{B}$ , it exerts following acceleration:

$$\left(\frac{1}{\mu_0\rho}\right)(\vec{B}\cdot\vec{\nabla})\delta\vec{B}=\left(\frac{ikB\delta\vec{B}}{\mu_0\rho}\right)=-\frac{k^2B^2}{\mu_0\rho}\vec{\xi}, \quad (1.51)$$

where we used equation (1.49). We see that the magnetic tension force causes a return force which is directly proportional to the displacement. All in all, this means that the oscillation frequency  $\omega$ , for small displacements in the plane of rotation of a disc in the presence of uniform magnetic field pointing in the vertical direction, satisfies an equation analogous to equation (1.44) (with constant  $K$  satisfying  $K=\frac{k^2B^2}{\mu_0\rho}$ ):

$$\omega^4-\left[2\left(\frac{k^2B^2}{\mu_0\rho}\right)+\kappa^2\right]\omega^2+\left(\frac{k^2B^2}{\mu_0\rho}\right)\left[\left(\frac{k^2B^2}{\mu_0\rho}\right)+R\frac{d\Omega^2}{dR}\right]=0. \quad (1.52)$$

If  $\frac{d\Omega^2}{dR}<0$ , there is an exponentially growing root of this equation for wavenumbers  $k$  which satisfy the condition  $\left(\frac{k^2B^2}{\mu_0\rho}\right)<-R\frac{d\Omega^2}{dR}$ , which corresponds to the onset of MRI. Since the magnetic field appears in equation (1.52) only as the product of  $kB$  then, even if  $B$  is very small, for very large wavenumbers  $k$  this magnetic tension can be important. This is the reason why the MRI is so sensitive to even very weak magnetic fields. Furthermore, it can be shown that the MRI is present regardless of the magnetic field geometry if the field is not too strong. In the case when the centripetal force is caused by the Newtonian gravitational force, we can write for an angular velocity

$$\Omega^2=\frac{GM}{R^3}, \quad (1.53)$$

where  $G$  is the gravitational constant,  $M$  is the central mass and  $R$  is the distance from the rotation axis. These discs are unstable to the MRI because  $R\frac{d\Omega^2}{dR}=-3\Omega^2<0$ .



## 2. Accretion tori: an overview of relevant aspects

In this section we highlight selected facts on accretion tori that are relevant for our subsequent investigations. Although the size of microquasars in our Galaxy and the size of quasars in AGNs are vastly different, it is thought that it is gravitational potential energy, released during accretion, that drives them both (Rees 1984; Karas & Šubr 2007). The presence of an accretion torus is an essential component of the unification scheme of active galactic nuclei (Antonucci 1993; Peterson 1997). According to this scenario, the torus connects inner regions with outer environment of the galaxy (Ferrarese & Merritt 2000). An accretion disc is evidenced in X-ray observations of AGNs (Fabian et al. 2004), where it provides the transport of material from outer parts of the nucleus to its centre where some fraction is accreted onto a black hole and some part is returned back via jets and winds.

An accretion disc is an important astrophysical phenomenon which is believed to play a key role for the full understanding of complex features taking place in active galactic nuclei. When the material of the disc approaches the event horizon of a black hole, an intense frictional heating and magnetic fields cause an X-ray emission. The large luminosity of quasars is being explained by the accretion of gas and dust onto supermassive black holes.

Several theoretical flavours of an accretion disc have been proposed. These solutions can be divided according to the geometrical thickness into thin discs and thick tori. The “standard” accretion disc model of Shakura-Sunayev is the example of a geometrically thin disc. A detailed exploration of thick accretion tori can be found, for example, in Pugliese & Montani (2015). The physics of accretion discs is not dependent on the scaling, hence, the same model parameters can be used both for stellar mass black holes and supermassive black holes (Karas & Šubr 2007). In this work we adopted Abramowicz et al. (1978) model of accretion torus which I describe in the next subsection.

### 2.1 Geometrically thick accretion tori

Before presenting basic equations describing the mass distribution inside a thick accretion torus, it is convenient to introduce the general relativistic von Zeipel’s theorem first (Abramowicz 1971; Tassoul 1978). This theorem sets sufficient and necessary conditions for the coincidence of isobaric and equidensity surfaces in the interior of an isolated, axially symmetric rotating mass of a perfect fluid in a steady state. An extension of the theorem to the magnetohydrodynamic regime has been discussed recently by (Zanotti & Pugliese 2015), who explored their structure both in the Newtonian and in the relativistic regimes. These authors approach the task by considering, separately, the case of a toroidal and of a poloidal magnetic field. While for the purely toroidal case (also adopted in our work) the von Zeipel theorem still provides an integrability condition, which is

satisfied, in the case of poloidal magnetic field one has to solve two additional partial differential equations. The treatment of the poloidal magnetic field is significantly more involved than that of toroidal magnetic fields. Let us adopt the following assumptions:

- a) The spacetime manifold of the body is asymptotically flat at radial infinity.
- b) The body and its manifold are stationary, and so a Killing vector field  $\eta$  (which is timelike at radial infinity and it has a unit length) exists there.
- c) The body and its manifold are axially symmetric, hence, there exists a Killing vector field  $\xi$ , which is spacelike at radial infinity and, furthermore, it is orthogonal to  $\eta$ .
- d) The body is made of a perfect fluid, which rotates only in the  $\xi$  direction and, therefore,

$$\mathcal{L}_\xi u = 0, \quad (2.1)$$

where  $\mathcal{L}$  denotes the Lie derivative and  $u$  denotes the four-velocity of the fluid.

For the rotating body we have

$$\xi^\mu p_{,\mu} = \eta^\mu p_{,\mu} = u^\mu p_{,\mu} = 0, \quad (2.2)$$

where a coma denotes the partial derivative. Considering the assumptions above we will show the validity of the following theorems:

- 1) The surfaces of constant density of the angular momentum per unit inertial mass  $l(r, \vartheta)$  and the surfaces of constant angular velocity of rotation  $\Omega(r, \vartheta)$  coincide with each other in the interior of the rotating body if and only if the body is barotropic ( $p$  is the pressure and  $\rho_0$  is the rest mass density):

$$p = p(\rho_0) \Leftrightarrow F(l, \Omega) = 0. \quad (2.3)$$

- 2) The surfaces of constant density of the angular momentum per baryon  $j$  and the surfaces of constant angular velocity of rotation  $\Omega$  coincide in the interior of the rotating body if the body is isentropic:

$$\sigma_{,\mu} = 0 \Rightarrow F(j, \Omega) = 0. \quad (2.4)$$

In order to prove these theorems it is convenient to use a coordinate system in which

$$\eta^\mu = \delta_t^\mu, \quad (2.5)$$

$$\xi^\mu = \delta_\varphi^\mu \quad (2.6)$$

and the spacetime interval can be written as

$$ds^2 = g_{tt}dt^2 + 2g_{t\varphi}d\varphi dt + g_{\varphi\varphi}d\varphi^2 + g_{AB}dA dB, \quad (2.7)$$

where  $A=(r, \vartheta)$  and  $B=(r, \vartheta)$ . We get the following expressions for the angular velocity of rotation, the density of angular momentum per baryon and the density of angular momentum per unit inertial mass in this coordinate system:

$$\Omega = \frac{u^\varphi}{u^t} = \frac{d\varphi}{dt}, \quad (2.8)$$

$$j = \frac{p + \rho_0}{n} u_\varphi, \quad (2.9)$$

$$l = -\frac{u_\varphi}{u_t}, \quad (2.10)$$

where  $n$  denotes the density of a baryon number. The energy-momentum tensor of an ideal fluid is

$$T_{\mu\nu} = (p + \rho_0)u_\mu u_\nu + pg_{\mu\nu}. \quad (2.11)$$

From the equation of the energy-momentum tensor conservation,  $T^\mu_{\nu;\mu} = 0$ , we get

$$(p + \rho_0)_{;\mu} u^\mu u_\nu + (p + \rho_0)(u^\mu_{;\mu} u_\nu + u^\mu u_{\nu;\mu}) + p_{;\mu} g^\mu_\nu = 0. \quad (2.12)$$

This equation can be rewritten as

$$(\rho_0 u^\mu)_{;\mu} u_\nu + p u^\mu_{;\mu} u_\nu + (p + \rho_0) u^\mu u_{\nu;\mu} + p_{;\mu} u^\mu u_\nu + p_{;\nu} = 0. \quad (2.13)$$

The first two terms on the left are equal to zero because of the validity of the continuity equation,  $(\rho_0 u^\mu)_{;\mu} = 0$ , assumptions of a steady state and the fact that  $\mathcal{L}_\xi u = 0$  thanks to which  $u^\mu_{;\mu} = 0$ . Thus, we obtain

$$(p + \rho_0) u^\mu u_{\nu;\mu} = -p_{;\nu} - u_\nu u^\mu p_{;\mu}. \quad (2.14)$$

Taking into account following equations:

$$u^\mu u_{\nu;\mu} = -u^\mu \Gamma^\sigma_{\mu\nu} u_\sigma = -\frac{1}{2} g_{\mu\rho,\nu} u^\mu u^\rho, \quad (2.15)$$

$$g_{\mu\rho} u^\mu u^\rho = -1 \Rightarrow (g_{\mu\rho} u^\mu u^\rho)_{;\nu} = 0, \quad (2.16)$$

which imply that

$$g_{\mu\rho,\nu} u^\mu u^\rho = -g_{\mu\rho} (u^\mu_{;\nu} u^\rho + u^\mu u^\rho_{;\nu}), \quad (2.17)$$

we get following expression:

$$u^\mu u_{\nu;\mu} = \frac{1}{2} (u^\mu_{;\nu} u_\mu + u_\rho u^\rho_{;\nu}) = u_t u^t_{;\nu} + u_\varphi u^\varphi_{;\nu}. \quad (2.18)$$

Thanks to the fact that  $u^\nu p_{;\nu} = 0$ , we can rewrite equation (2.14) and obtain

$$\begin{aligned} (p + \rho_0)^{-1} p_{;\nu} &= -u_t u^t_{;\nu} - u_\varphi u^\varphi_{;\nu} = -u_\varphi u^\varphi_{;\nu} - \frac{u_t u^t u^t_{;\nu} + u^t_{;\nu} - u^t_{;\nu}}{u^t} \\ &= \frac{u^t_{;\nu}}{u^t} - \frac{u^t u_\varphi u^t u^\varphi_{;\nu} - u^t u^\varphi u_\varphi u^t_{;\nu}}{(u^t)^2} \\ &= (\ln u^t)_{;\nu} - (u^t u_\varphi) \Omega_{;\nu}. \end{aligned} \quad (2.19)$$

Let us derive this equation and multiply the result by the completely antisymmetric tensor  $\epsilon^{\kappa\lambda\mu\nu}$ . Then we get

$$(p + \rho_0)^{-2} \rho_{0,\nu} p_{;\mu} \epsilon^{\kappa\lambda\mu\nu} = (u^t u_\varphi)_{;\nu} \Omega_{;\mu} \epsilon^{\kappa\lambda\mu\nu}. \quad (2.20)$$

From the last two equations we see that the gradients of  $\rho_0$ ,  $p$  and  $u^t$  are parallel in the case of the rigid rotation ( $\Omega_{;\mu} = 0$ ) and so the surfaces of their constant

values must coincide. It follows from equation (2.20) that the gradients of density and pressure are parallel if and only if

$$(u^t u_\varphi)_{,\nu} \Omega_{,\mu} \epsilon^{\kappa\lambda\mu\nu} = 0, \quad (2.21)$$

or equivalently written in another form

$$f(u^t u_\varphi, \Omega) = 0, \quad (2.22)$$

where  $f$  is the function of  $\Omega$  and  $u^t u_\varphi$  only. From the normalization condition for four-velocity,  $u^\mu u_\mu = -1$ , we obtain

$$u^t u_\varphi = -(\Omega - l^{-1})^{-1} \quad (2.23)$$

and

$$F(l, \Omega) = 0 \quad (2.24)$$

as a result of equations (2.22) and (2.23). One can see that we have just proven the statement (2.3). I will not demonstrate the proof of the second statement here (see Abramowicz (1971) for details). The most frequently used definitions of the specific angular momentum in the relativistic case are:

$$l \equiv -\frac{u_\varphi}{u^t}, \quad (2.25)$$

$$l_0 \equiv -u_\varphi, \quad (2.26)$$

$$l_* \equiv -u_\varphi u^t. \quad (2.27)$$

The relativistic angular velocity is defined by

$$\Omega \equiv \frac{u^\varphi}{u^t}. \quad (2.28)$$

From equations (2.25) and (2.28) it follows that

$$l = -\frac{g_{t\varphi} + \Omega g_{\varphi\varphi}}{g_{tt} + \Omega g_{t\varphi}}$$

and

$$\Omega = -\frac{g_{t\varphi} + l g_{tt}}{g_{\varphi\varphi} + l g_{t\varphi}}. \quad (2.29)$$

We will call the surfaces of constant  $l$  and  $\Omega$  the von Zeipel's cylinders. If the background gravitational field is known and the special form of the von Zeipel's formula (Abramowicz 1971) is assumed one can easily find the explicit form of the functions

$$l = l(r, \theta)$$

and

$$\Omega = \Omega(r, \theta) \quad (2.30)$$

by solving equation (2.29).

In the barotropic case the surfaces of  $l = \text{const.}$  and the surfaces of  $\Omega = \text{const.}$  coincide, hence, we can introduce the function

$$F \equiv (1 - \Omega l) \exp \int_{l_{in}}^l (1 - \Omega l)^{-1} \Omega dl, \quad (2.31)$$

where  $l_{in}$  denotes the value of  $l$  on the inner edge of the torus. The time component of the four-velocity,  $A \equiv u^t$ , is called the redshift factor and  $U \equiv u_t$  is energy of the fluid element per unit inertial mass. From the normalization condition for a four-velocity we get:

$$A = (-g_{tt} - 2\Omega g_{t\varphi} - g_{\varphi\varphi} \Omega^2)^{-\frac{1}{2}}, \quad (2.32)$$

$$U = (g_{\varphi\varphi} + 2l g_{t\varphi} + l^2 g_{tt})^{-\frac{1}{2}} (g_{t\varphi}^2 - g_{tt} g_{\varphi\varphi})^{\frac{1}{2}}, \quad (2.33)$$

$$AU = -(1 - \Omega l)^{-1}. \quad (2.34)$$

For details see (1) and (2) in Appendix. We can write the solution of the relativistic Euler equation (2.19) in the form

$$\frac{p_{,\mu}}{p + \epsilon} = (\ln A)_{,\mu} - \frac{l \Omega_{,\mu}}{1 - \Omega l}, \quad (2.35)$$

where  $\epsilon$  denotes the total energy density,  $\epsilon = \rho_0 + u$ , and  $u$  is the density of internal energy. Using equations (2.31) and (2.34) we obtain:

$$\begin{aligned} W - W_{in} &\equiv \ln(F A)_{in} - \ln(F A) = \ln A_{in} - \ln A - \ln(AU)_{in} + \ln(AU) \\ &\quad - \int_{l_{in}}^l (1 - \Omega l)^{-1} \Omega dl \\ &= \ln A_{in} - \ln A + \ln(1 - \Omega l)_{in} - \ln(1 - \Omega l) - \int_{l_{in}}^l (1 - \Omega l)^{-1} \Omega dl \\ &= \ln A_{in} - \ln A + \ln(1 - \Omega l)_{in} - \ln(1 - \Omega l) \\ &\quad - \int_{(\Omega l)_{in}}^{\Omega l} (1 - \Omega l)^{-1} d(\Omega l) + \int_{\Omega_{in}}^{\Omega} (1 - \Omega l)^{-1} l d\Omega \\ &= \ln A_{in} - \ln A + \int_{\Omega_{in}}^{\Omega} (1 - \Omega l)^{-1} l d\Omega = - \int_0^p \frac{dp}{p + \epsilon}, \end{aligned} \quad (2.36)$$

and

$$W - W_{in} = \ln U - \ln U_{in} - \int_{l_{in}}^l \frac{\Omega dl}{1 - \Omega l} = - \int_0^p \frac{dp}{p + \epsilon}, \quad (2.37)$$

where we used equation (2.35). The quantity  $W = W(p)$  is equal to the total potential energy in the Newtonian limit (expressed in units of  $c^2$ ). Therefore,  $W = 0$  at infinity. The isobaric (equipotential) surfaces are given by the equation  $W = \text{const.}$  For a known background gravitational field and a given von Zeipel's relation it is easy to determine the explicit form of the equation  $W(r, \theta) = \text{const.}$  from equations (2.30) and (2.37). Thus, the problem of constructing the model of the torus is completely solved. Figure 2.1 shows the equipressure surfaces for different positions of the inner edge of the torus.

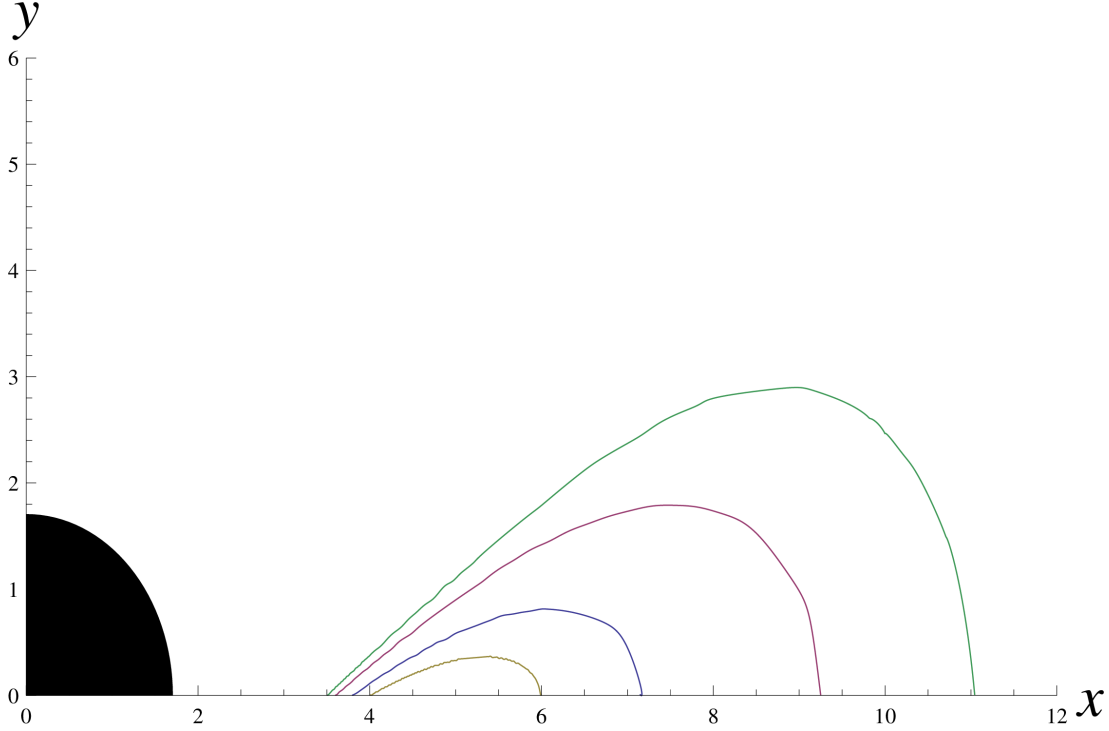


Figure 2.1: Equipressure surfaces obtained by solving equation (2.37) for the Kerr background with  $a = 0.5$ . The profile of specific angular momentum was set as  $l(R) = l_K(R_{\text{in}}) + 0.03(R - R_{\text{in}})$ , where  $l_K$  is the keplerian angular momentum. The inner edge is at  $R_{\text{in}} = 3.5, 3.6, 3.8, 4.0$ . Cartesian coordinates  $(x, y)$  are derived from Boyer-Lindquist coordinates,  $x^2 + y^2 = R^2(x = R \sin \vartheta, y = R \cos \vartheta)$  and scaled with units of  $R_g$ . Black circle denotes the black hole horizon.

Now we are ready to give explicit solutions for tori with following properties:

$$l = \text{const.} \quad (2.38)$$

or

$$l_* \equiv \frac{l}{1 - \Omega l} = \text{const.} \quad (2.39)$$

The second assumption was used by Fishbone & Moncrief (1976). In the case of  $l = \text{const.}$  it is easy to see from equation (2.37) that

$$W = -\ln[A(1 - \Omega l)] = \ln U. \quad (2.40)$$

In the case of  $l_* = \text{const.}$  we get

$$W = -\ln A + l_* \Omega. \quad (2.41)$$

(For details see Abramowicz et al. (1978)). In the case of  $l = \text{const.}$ , we obtain

$$W - W_{\text{in}} = \ln U - \ln U_{\text{in}} = - \int_0^P \frac{dp}{p + \rho_0 + u}. \quad (2.42)$$

## 2.2 Magnetised torus

Now we consider that the magnetic field is present inside the torus. In this case the energy-momentum tensor can be written as

$$T^{\mu\nu} = (w + b^2)u^\mu u^\nu + \left(p_g + \frac{1}{2}b^2\right)g^{\mu\nu} - b^\mu b^\nu, \quad (2.43)$$

where  $w$  is the specific enthalpy ( $w = \rho_0 + p_g + u$ ),  $p_g$  is the gas pressure and  $b^\mu$  is the projection of the magnetic field vector defined in equation (3.26). Our assumptions about the flow are the same as in the previous subsection ( $f_{,t} = f_{,\varphi} = 0$ ). We will also restrict ourselves in the cases of purely azimuthal magnetic fields satisfying  $b^r = b^\vartheta = 0$ . The covariant equations of ideal relativistic MHD are energy-momentum tensor conservation, continuity equation and Maxwell's equations. In our case the only non-trivial result follows from the energy-momentum tensor conservation  $T^{\mu\nu}_{;\nu} = 0$ . Contracting this equation with projection tensor  $h^\mu{}_\nu$  we obtain (see (10) in Appendix for details)

$$(w + b^2)u_\nu u^\nu_{;i} + (p_g + b^2)_{,i} - b_\nu b^\nu_{;i} = 0, \quad (2.44)$$

where  $i = r, \vartheta$ . We can rewrite this equation in terms of the angular velocity  $\Omega$  and the specific angular momentum  $l$ . Then we get (see (20) in Appendix)

$$(\ln |u_t|)_{,i} - \frac{\Omega}{1 - l\Omega} l_{,i} + \frac{p_{g,i}}{w} + \frac{(\mathcal{L}b^2)_{,i}}{2\mathcal{L}w} = 0, \quad (2.45)$$

where  $\mathcal{L}(r, \vartheta) \equiv g_{t\varphi}^2 - g_{tt}g_{\varphi\varphi}$ . When  $b^2 \rightarrow 0$  then equation (2.45) reduces to equation (2.35). For a barotropic equation of state ( $w = w(p_g)$ ), it follows from equation (2.45) that

$$d\left(\ln |u_t| + \int_0^{P_g} \frac{dp_g}{w}\right) - \frac{\Omega}{1 - l\Omega} dl + \frac{d(\mathcal{L}b^2)}{2\mathcal{L}w} = 0. \quad (2.46)$$

In the case of a non-magnetised torus, this equation implies that  $\Omega = \Omega(l)$  and, consequently, the surfaces of constant  $\Omega$  and  $l$  coincide (Abramowicz 1971). However, it does not have to be valid for the magnetised torus. Nevertheless, if we still assume that  $\Omega = \Omega(l)$ , for some reason, then we can rewrite equation (2.46) as

$$\ln |u_t| + \int_0^{P_g} \frac{dp_g}{w} - \int_0^l \frac{\Omega dl}{1 - \Omega l} + \int_0^{\tilde{P}_m} \frac{d\tilde{p}_m}{\tilde{w}} = const., \quad (2.47)$$

where  $\tilde{w} \equiv \mathcal{L}w$ ,  $\tilde{p}_m \equiv \mathcal{L}p_m$  and  $p_m = \frac{b^2}{2}$  is the magnetic pressure. The boundary conditions on the surface of the torus and also on its inner edge are

$$p_g = p_m = 0, u_t = u_{t_{in}}, l = l_{in}. \quad (2.48)$$

Hence, we can find the constant of integration as

$$const. = \ln |u_{t_{in}}| - \int_0^{l_{in}} \frac{\Omega dl}{1 - \Omega l}. \quad (2.49)$$

Let us assume that  $l$  reaches a constant value inside a torus. Then we can rewrite equation (2.47) into the following form:

$$W - W_{in} + \int_0^{P_g} \frac{dp_g}{w} + \int_0^{\tilde{P}_m} \frac{d\tilde{p}_m}{\tilde{w}} = 0. \quad (2.50)$$

If  $l$  is not a constant, we will solve

$$\ln |u_t| - \ln |u_{t_{in}}| + \int_0^{P_g} \frac{dp_g}{w} - \int_0^l \frac{\Omega dl}{1 - \Omega l} + \int_0^{\tilde{P}_m} \frac{d\tilde{p}_m}{\tilde{w}} = 0. \quad (2.51)$$

I show in Appendix (see (12) and (13)) that for the non-zero components of  $b^\mu$  the following expressions are valid:

$$b^\varphi = \pm \sqrt{\frac{2p_m}{\mathcal{A}}}$$

and

$$b^t = lb^\varphi, \quad (2.52)$$

where  $\mathcal{A} \equiv g_{\varphi\varphi} + 2lg_{t\varphi} + l^2g_{tt}$ .

### 2.3 Oscillation modes of relativistic tori

In this section I closely follow a comprehensive treatment of the linear modes of a hydrodynamic, non-self-gravitating, polytropic slender torus as was presented by Blaes et al. (2006). The results of that paper will be useful in Chapter 4 where we perturb the torus and let it evolve numerically. Then we compare the oscillation frequency, obtained from this numerical simulation for geometrically thick torus, with frequencies derived analytically by Blaes et al. (2006) for thin discs. By this comparison we will investigate the impact of inertial modes caused by finite torus thickness on the final oscillation mode. Theoretically, these inertial frequencies could cause that the torus would oscillate with frequency not allowed for thin discs or slender tori (Blaes et al. 2007; Horák 2008; Straub & Šrámková 2009).

Let us consider an equilibrium, axisymmetric torus in a state of a pure rotation. In this case the only non-zero components of a four-velocity are  $u^t$  and  $u^\varphi$ . The relativistic Euler equation can be written as (see (25) in Appendix)

$$-\frac{1}{2}U^2(\nabla g^{tt} - 2l\nabla g^{t\varphi} + l^2\nabla g^{\varphi\varphi}) = \frac{\nabla p}{p + \epsilon}. \quad (2.53)$$

The differential operator  $\nabla$  can be taken to be either  $\frac{\partial}{\partial r}$  or  $\frac{\partial}{\partial \theta}$ . The fluid orbits on a circular geodesic at the point where the pressure reaches its maximum. We see from equation (2.53) that the Keplerian specific angular momentum  $l_0$  satisfies the following condition at radius  $r_0$ :

$$(g^{tt}_{,r} - 2l_0g^{t\varphi}_{,r} + l_0^2g^{\varphi\varphi}_{,r})_0 = 0, \quad (2.54)$$

where subscript 0 refers to the point of pressure maximum. One can deduce from equation (2.54) that it is convenient to introduce an effective potential

$$\mathcal{U} \equiv g^{tt} - 2l_0 g^{t\varphi} + l_0^2 g^{\varphi\varphi}. \quad (2.55)$$

A test particle with a specific angular momentum  $l_0$  orbits on a circular geodesic at the extremum of  $\mathcal{U}$  which is located at the pressure maximum  $r_0$ . Radial and vertical epicyclic oscillations occur when the initial circular orbit is linearly perturbed. The squares of the corresponding frequencies, measured by an observer at infinity (Abramowicz et al. 2006), are (see (30) in Appendix for details):

$$\omega_r^2 = \frac{U_0^2}{A_0^2} \left( \frac{1}{2g_{rr}} \frac{\partial^2 \mathcal{U}}{\partial r^2} \right)_0$$

and

$$\omega_\theta^2 = \frac{U_0^2}{A_0^2} \left( \frac{1}{2g_{\theta\theta}} \frac{\partial^2 \mathcal{U}}{\partial \theta^2} \right)_0. \quad (2.56)$$

If we prescribe a polytropic equation of state, we can express the pressure and the density in terms of an auxiliary function  $f(r, \theta)$ :

$$p = p_0 f^{n+1}, \quad \rho = \rho_0 f^n. \quad (2.57)$$

Let us consider a slender torus inside which the ratio  $p_0/\rho_0$  is very small. By introducing local coordinates measured from the equilibrium point,

$$x \equiv \sqrt{g_{rr0}} \left( \frac{r - r_0}{r_0} \right), \quad y \equiv \sqrt{g_{\theta\theta0}} \left( \frac{\pi/2 - \theta}{r_0} \right), \quad (2.58)$$

Abramowicz et al. (2006) expanded equation (2.53) to show that

$$f = 1 - \frac{1}{\zeta^2} \left\{ \left[ \tilde{\omega}_r^2 - \frac{U_0^2}{A_0^2 \Omega_0^2 l_0} \left( \frac{g^{tt}_{,r} - l_0 g^{t\varphi}_{,r}}{g_{rr}} \frac{\partial l}{\partial r} \right)_0 \right] x^2 + \tilde{\omega}_\theta^2 y^2 \right\}, \quad (2.59)$$

where

$$\zeta^2 \equiv \frac{2(n+1)p_0}{\rho_0 A_0^2 r_0^2 \Omega_0^2} \quad (2.60)$$

is a dimensionless parameter which determines the thickness of the torus (for details see (41) in Appendix). We obtain a slender torus in the limit  $\zeta \rightarrow 0$ . The frequencies  $\tilde{\omega}_r$  and  $\tilde{\omega}_\theta$  are the epicyclic frequencies scaled by the angular velocity at the pressure maximum  $\Omega_0$ . Equation (2.59) can be written more simply. In order to show that let us follow Seguin (1975) and define the spatial vector

$$\vec{\gamma} \equiv AU^3[(1 + l\Omega)\nabla g^{t\varphi} - \Omega\nabla g^{tt} - l\nabla g^{\varphi\varphi}]. \quad (2.61)$$

If the fluid is barotropic then the surfaces of constant  $\Omega$  and  $l$  coincide (Abramowicz 1971). When we apply a curl on equation (2.53), it is then easy to see that the vector  $\vec{\gamma}$  is perpendicular to these level surfaces:

$$\vec{\gamma} \times \nabla l = 0. \quad (2.62)$$

The quantity

$$\kappa^2 \equiv \frac{1}{A^2} \vec{\gamma} \cdot \nabla l = \frac{1}{A^2} \left( \frac{\gamma_r}{g_{rr}} \frac{\partial l}{\partial r} + \frac{\gamma_\theta}{g_{\theta\theta}} \frac{\partial l}{\partial \theta} \right) \quad (2.63)$$

represents the characteristic squared frequency of inertial oscillations in the fluid due to the presence of an equilibrium specific angular momentum gradient. It follows from equations (2.54), (2.61) and (2.63) that

$$\kappa_0^2 \equiv \tilde{\kappa}_0^2 \Omega_0^2 = \frac{U_0^2}{l_0 A_0^2} \left( \frac{g^{tt}_{,r} - l_0 g^{t\varphi}_{,r}}{g_{rr}} \frac{\partial l}{\partial r} \right)_0 \quad (2.64)$$

at the point of the pressure maximum. Finally, equation (2.59) can be rewritten as

$$f = 1 - (\tilde{\omega}_r^2 - \tilde{\kappa}_0^2) \tilde{x}^2 - \tilde{\omega}_\theta^2 \tilde{y}^2, \quad (2.65)$$

where  $\tilde{x} \equiv \frac{x}{\xi}$  and  $\tilde{y} \equiv \frac{y}{\zeta}$ .

The dynamics of linear perturbations of the torus is described by equations which may be derived by linearising the relativistic continuity equation

$$\nabla_\alpha (\rho u^\alpha) = 0, \quad (2.66)$$

the relativistic Euler equation

$$u^\beta \nabla_\beta u^\alpha = - \frac{u^\alpha u^\mu + g^{\alpha\mu}}{\epsilon + p} \nabla_\mu p \quad (2.67)$$

and the equation of state. Since the equilibrium state is stationary and axisymmetric, we prescribe perturbation variables to vary with  $t$  and  $\varphi$  as  $\exp[i(m\varphi - \omega t)]$ . Ipser & Lindblom (1992) showed that the resulting perturbation equations can be combined into a single, second-order partial differential equation in terms of a single scalar perturbation variable which we define as

$$\mathcal{W} \equiv - \frac{\delta p}{\rho A \sigma}, \quad (2.68)$$

where  $\sigma \equiv \omega - m\Omega$ . It can be proved that equations (2.53) and (2.61) imply

$$\begin{aligned} - \frac{A\sigma\mathcal{W}}{\epsilon + p} \nabla p + \nabla(A\sigma\mathcal{W}) &= A\sigma\nabla\mathcal{W} + \mathcal{W}\sigma \left[ -\frac{l}{U}\gamma + U(A^2\Omega + g^{t\varphi})\nabla l \right] \\ &+ \mathcal{W}m \left[ \frac{1 - l\Omega}{U}\gamma + U(\Omega g^{t\varphi} - g^{\varphi\varphi})\nabla l \right]. \end{aligned} \quad (2.69)$$

If we use this equation and equation (2.62), it can be shown that  $r$  and  $\theta$  components of the Eulerian four-velocity perturbation are given by

$$\begin{aligned} \delta \vec{u} &= \frac{i\rho}{\epsilon + p} \nabla \mathcal{W} + \frac{i}{A^2(\sigma^2 - \kappa^2)} \left( \frac{\rho}{\epsilon + p} \right) \\ &\{ \gamma(\nabla l \cdot \nabla \mathcal{W}) + \sigma A U \mathcal{W} [\sigma(A^2\Omega + g^{t\varphi}) + m(\Omega g^{t\varphi} - g^{\varphi\varphi})] \nabla l \} \end{aligned} \quad (2.70)$$

and the azimuthal component is

$$\begin{aligned} \delta u_\varphi = & \frac{\rho}{\epsilon + p} AU(\sigma l + m\Omega l - m)\mathcal{W} + \frac{U^2}{A(\sigma^2 - \kappa^2)} \left( \frac{\rho}{\epsilon + p} \right) \nabla l \cdot \{A\sigma \nabla \mathcal{W} \\ & + \mathcal{W}U[\sigma(A^2\Omega + g^{t\varphi}) + m(\Omega g^{t\varphi} - g^{\varphi\varphi})]\nabla l\}. \end{aligned} \quad (2.71)$$

Adding the linearised continuity equation,

$$\begin{aligned} i\frac{\sigma^2 A^2 \rho^2 n}{(n+1)p}\mathcal{W} - i(\sigma l + m\Omega l - m)\rho(g^{\varphi\varphi} - g^{t\varphi}\Omega)\delta u_\varphi + \frac{1}{\sqrt{-g}}\frac{\partial}{\partial r}[\sqrt{-g}\rho g^{rr}\delta u_r] \\ + \frac{1}{\sqrt{-g}}\frac{\partial}{\partial \theta}[\sqrt{-g}\rho g^{\theta\theta}\delta u_\theta] = 0, \end{aligned} \quad (2.72)$$

we get the complete set of equations. In the limit of a slender torus,  $r$  and  $\theta$  derivatives of  $\mathcal{W}$  become dominant in equations (2.70) and (2.71). Hence, it imply

$$\delta u_r \sim i\frac{\sigma_0^2}{\sigma_0^2 - \kappa_0^2}\frac{\partial \mathcal{W}}{\partial r}, \delta u_\theta \sim i\frac{\partial \mathcal{W}}{\partial \theta}$$

and

$$\delta u_\varphi \sim \frac{U_0^2 \sigma_0}{\sigma_0^2 - \kappa_0^2} g_0^{rr} \left( \frac{\partial l}{\partial r} \right)_0 \frac{\partial \mathcal{W}}{\partial r}. \quad (2.73)$$

Substituting into the linearised continuity equation, transforming coordinates from  $r$  and  $\theta$  to the local, scaled coordinates  $\tilde{x}$  and  $\tilde{y}$  and taking the slender torus limit  $\zeta \rightarrow 0$ , we obtain

$$\frac{\tilde{\sigma}_0^2}{\tilde{\sigma}_0^2 - \tilde{\kappa}_0^2} \frac{\partial}{\partial \tilde{x}} \left( f^n \frac{\partial \mathcal{W}}{\partial \tilde{x}} \right) + \frac{\partial}{\partial \tilde{y}} \left( f^n \frac{\partial \mathcal{W}}{\partial \tilde{y}} \right) + 2n\tilde{\sigma}_0^2 f^{n-1} \mathcal{W} = 0, \quad (2.74)$$

where  $\tilde{\sigma}_0 \equiv \frac{\sigma_0}{\Omega_0} \equiv \frac{(\omega - m\Omega_0)}{\Omega_0}$ . We solve this equation together with the boundary condition which says that the Lagrangian perturbation in pressure vanishes at the unperturbed surface:

$$\Delta p_{f=0} = (\delta p + \xi^\alpha \nabla_\alpha p)_{f=0} = 0, \quad (2.75)$$

where  $\xi^\alpha$  is the Lagrangian displacement vector. Using the gauge choice  $\xi^\alpha u_\alpha = 0$ , the  $r$  and  $\theta$  components are given by

$$\vec{\xi} = \frac{i}{A\sigma} \delta \vec{u}. \quad (2.76)$$

The boundary condition may be written as

$$\left( f^n \left[ \frac{\tilde{\sigma}_0^2}{\tilde{\sigma}_0^2 - \tilde{\kappa}_0^2} \frac{\partial f}{\partial \tilde{x}} \frac{\partial \mathcal{W}}{\partial \tilde{x}} + \frac{1}{\tilde{\sigma}_0} \frac{\partial f}{\partial \tilde{y}} \frac{\partial \mathcal{W}}{\partial \tilde{y}} + 2\tilde{\sigma}_0 \mathcal{W} \right] \right)_{f=0} = 0 \quad (2.77)$$

in the slender torus limit.

It is worth noticing that equations (2.65), (2.74) and (2.77) describe a global eigenvalue problem for modes of the relativistic, polytropic slender torus. All the interesting effects reduce to three characteristic frequencies: the radial epicyclic

frequency  $\tilde{\omega}_r$ , the vertical epicyclic frequency  $\tilde{\omega}_\theta$  and the characteristic frequency of inertial modes at the pressure maximum  $\tilde{\kappa}_0$ . Abramowicz et al. (2006) showed that the slender torus always admits incompressible modes corresponding to global oscillations of the entire torus at the epicyclic frequencies of the external space-time:

$$\mathcal{W}_r = \tilde{x}, \tilde{\sigma}_0^2 = \tilde{\omega}_r^2 \quad (2.78)$$

and

$$\mathcal{W}_\theta = \tilde{y}, \tilde{\sigma}_0^2 = \tilde{\omega}_\theta^2. \quad (2.79)$$

The fluid velocity for these modes is spatially constant over a torus cross-section. The remaining modes are of three general types: surface gravity waves, internal inertial waves and acoustic waves. The last two classes are easily revealed in a Wentzel-Kramers-Brillouin (WKB) analysis of equation (2.74). Assuming the  $\tilde{x} - \tilde{y}$  dependence proportional to  $\exp\{i[\int \tilde{k}_x(\tilde{x})d\tilde{x} + \int \tilde{k}_y(\tilde{y})d\tilde{y}]\}$  and taking the high wavenumber limit  $\tilde{k} \equiv \sqrt{\tilde{k}_x^2 + \tilde{k}_y^2} \rightarrow \infty$ , we obtain the local dispersion relation

$$\tilde{\sigma}_0^4 - (\tilde{k}^2 \tilde{c}_S^2 + \tilde{\kappa}_0^2) \sigma_0^2 + \tilde{k}_y^2 \tilde{c}_S^2 \tilde{\kappa}_0^2 = 0, \quad (2.80)$$

where

$$\tilde{c}_S \equiv \frac{c_S}{\zeta A_0 r_0 \Omega_0} = c_S \sqrt{\frac{\rho_0}{2(n+1)p_0}} \quad (2.81)$$

is a scaled local sound speed. From this dispersion relation we can obtain two solutions describing the high-wavenumber behaviour for acoustic and inertial waves:

$$\tilde{\sigma}_0^2 = \tilde{k}^2 \tilde{c}_S^2 \quad (2.82)$$

and

$$\tilde{\sigma}_0^2 = \frac{\tilde{k}_y^2 \tilde{\kappa}_0^2}{\tilde{k}^2}. \quad (2.83)$$

This justifies our claim that  $\tilde{\kappa}_0$  is the characteristic frequency of inertial oscillations in the fluid. According to the equilibrium equation (2.65), the surfaces of constant density and pressure have a perfectly elliptical cross-section in  $(\tilde{x}, \tilde{y})$  coordinates. The slender torus equilibrium is therefore perfectly reflection symmetric around  $\tilde{x} = 0$  and  $\tilde{y} = 0$ . Hence, all the slender torus modes can be assigned a definite parity  $P_x$  and  $P_y$  with respect to each of these reflections. Positive  $P_x$  or  $P_y$  correspond to eigenfunctions in  $W$  which are even in  $\tilde{x}$  or  $\tilde{y}$  while negative parities correspond to eigenfunctions in  $W$  which are odd in these variables. Generally, thicker tori remain reflection symmetric around the equatorial plane and, consequently, their modes will keep a definite  $P_y$ . On the other hand, well-defined  $P_x$  exists only in the slender torus limit.

Blaes (1985) showed that the equation (2.74) becomes separable and solved the complete eigenvalue problem. The eigenfunctions and eigenfrequencies can be written as

$$\mathcal{W}_{jk} = C_{jk} \eta^k G_j(k+n, k+1, \eta^2) \cos(k\theta)$$

or

$$\mathcal{W}_{jk} = C_{jk} \eta^k G_j(k+n, k+1, \eta^2) \sin(k\theta) \quad (2.84)$$

and

$$\tilde{\sigma}_0^2 = \frac{1}{n}(2j^2 + 2jn + 2jk + nk), \quad (2.85)$$

where  $C_{jk}$  is a normalization constant,  $j$  and  $k$  are non-negative integers and  $G_j$  is a  $j$ -th order Jacobi polynomial. The zero frequency,  $j = k = 0$ , mode is the corotation mode. The modes with  $j = 0$ ,  $k = 1$  correspond to the global radial and vertical epicyclic oscillations of the entire torus. Other modes with  $j = 0$  have frequencies which are independent of the polytropic equation of state, and represent surface gravity waves. Modes with  $k = 0$  and  $j \neq 0$  are compressible breathing modes where the torus cross-section expands and contracts. All the other modes have a mixed acoustic/surface gravity wave character.

### 2.3.1 The lowest order modes of the general problem

The zero corotation frequency and epicyclic modes are always present in a general torus configuration. One can find additional modes by following the idea that the Taylor expansion of the solution for  $W$  around the pressure maximum will generally diverge as the surface  $f = 0$  is approached, which is the consequence of the structure of the partial differential equation (2.74). A finite solution that is able to satisfy the surface boundary condition (2.77), will therefore probably involve a truncation of the Taylor expansion, i.e. include only finite polynomials in  $\tilde{x}$  and  $\tilde{y}$ . Since we know that the modes must be odd or even, we try an eigenfunction of the form

$$\mathcal{W} = a\tilde{x}\tilde{y}, \quad (2.86)$$

where  $a$  is a constant. This function is odd in  $\tilde{x}$  and also in  $\tilde{y}$ . Furthermore, it obviously satisfies the boundary condition (2.77). It gives two modes, with eigenfrequencies determined by the partial differential equation (2.74):

$$\tilde{\sigma}_0^2 = \frac{1}{2} \left( \tilde{\omega}_r^2 + \tilde{\omega}_\theta^2 \pm [(\tilde{\omega}_r^2 + \tilde{\omega}_\theta^2)^2 - 4\tilde{\kappa}_0^2\tilde{\omega}_\theta^2]^{\frac{1}{2}} \right). \quad (2.87)$$

We can go further by trying an eigenfunction of the form

$$\mathcal{W} = a + b\tilde{x}^2 + c\tilde{y}^2, \quad (2.88)$$

which is even in both  $\tilde{x}$  and  $\tilde{y}$ . In this expression  $a$ ,  $b$  and  $c$  are constants amongst which one is arbitrary. If we substitute this function into equation (2.74) and equate coefficients of 1,  $\tilde{x}$  and  $\tilde{y}$ , we end with three linear homogeneous equations for  $a$ ,  $b$  and  $c$ . Setting the determinant of coefficients to zero we obtain the eigenfrequencies of the zero corotation frequency mode (for which  $b = c = 0$ ) as well as

$$\tilde{\sigma}_0^2 = \frac{1}{2n} \{ (2n+1)(\tilde{\omega}_r^2 + \tilde{\omega}_\theta^2) - (n+1)\tilde{\kappa}_0^2 \pm [((2n+1)(\tilde{\omega}_\theta^2 - \tilde{\omega}_r^2) + (n+1)\tilde{\kappa}_0^2)^2 + 4\tilde{\omega}_\theta^2(\tilde{\omega}_r^2 - \tilde{\kappa}_0^2)]^{\frac{1}{2}} \}. \quad (2.89)$$

The frequency corresponding to the upper sign in the above equation blows up in the incompressible limit ( $n \rightarrow 0$ ), revealing that it is in general an acoustic

$f_0^2$	0	(+,+,0,0)
$f_1^2$	$\omega_r^2$	(-,+,0,1)
$f_2^2$	$\omega_\theta^2$	(+,-,0,1)
$f_3^2$	$\{\omega_r^2 + \omega_\theta^2 \pm [(\omega_r^2 + \omega_\theta^2)^2 - 4\kappa_0^2 \omega_\theta^2]^{\frac{1}{2}}\}/2$	(-, -, 0, 2)
$f_4^2$	$\{(2n+1)(\omega_r^2 + \omega_\theta^2) - (n+1)\kappa_0^2 - [((2n+1)(\omega_\theta^2 - \omega_r^2) + (n+1)\kappa_0^2)^2 + 4\omega_\theta^2(\omega_r^2 - \kappa_0^2)]^{\frac{1}{2}}\}/(2n)$	(+,+,0,2)
$f_5^2$	$\{(2n+1)(\omega_r^2 + \omega_\theta^2) - (n+1)\kappa_0^2 + [((2n+1)(\omega_\theta^2 - \omega_r^2) + (n+1)\kappa_0^2)^2 + 4\omega_\theta^2(\omega_r^2 - \kappa_0^2)]^{\frac{1}{2}}\}/(2n)$	(+,+,1,0)

Table 2.1: Eigenfrequencies of the lowest order modes of the general polytropic slender torus. In the first column there are frequencies  $\sigma_0^2$  for various  $(P_x, P_y, j, k)$  whose values are expressed in the third column.

$f_0^2$	0	(+,+,0,0)
$f_1^2$	$\omega_r^2$	(-,+,0,1)
$f_2^2$	$\omega_\theta^2$	(+,-,0,1)
$f_3^2$	$\omega_r^2 + \omega_\theta^2$	(-, -, 0, 2)
$f_4^2$	$\{(2n+1)(\omega_r^2 + \omega_\theta^2) - [4n(n+1)(\omega_\theta^2 - \omega_r^2)^2 + (\omega_r^2 + \omega_\theta^2)^2]^{\frac{1}{2}}\}/(2n)$	(+,+,0,2)
$f_5^2$	$\{(2n+1)(\omega_r^2 + \omega_\theta^2) + [4n(n+1)(\omega_\theta^2 - \omega_r^2)^2 + (\omega_r^2 + \omega_\theta^2)^2]^{\frac{1}{2}}\}/(2n)$	(+,+,1,0)
$f_6^2$	$\{(4n+3)\omega_r^2 + (2n+1)\omega_\theta^2 - [4n^2(\omega_\theta^2 - \omega_r^2)^2 + 4n(\omega_\theta^2 - \omega_r^2)(\omega_\theta^2 - 3\omega_r^2) + (\omega_\theta^2 + 3\omega_r^2)^2]^{\frac{1}{2}}\}/(2n)$	(-,+,0,3)
$f_7^2$	$\{(4n+3)\omega_r^2 + (2n+1)\omega_\theta^2 + [4n^2(\omega_\theta^2 - \omega_r^2)^2 + 4n(\omega_\theta^2 - \omega_r^2)(\omega_\theta^2 - 3\omega_r^2) + (\omega_\theta^2 + 3\omega_r^2)^2]^{\frac{1}{2}}\}/(2n)$	(-,+,1,1)
$f_8^2$	$\{(4n+3)\omega_\theta^2 + (2n+1)\omega_r^2 - [4n^2(\omega_\theta^2 - \omega_r^2)^2 + 4n(\omega_r^2 - \omega_\theta^2)(\omega_r^2 - 3\omega_\theta^2) + (\omega_r^2 + 3\omega_\theta^2)^2]^{\frac{1}{2}}\}/(2n)$	(+,-,0,3)
$f_9^2$	$\{(4n+3)\omega_\theta^2 + (2n+1)\omega_r^2 + [4n^2(\omega_\theta^2 - \omega_r^2)^2 + 4n(\omega_r^2 - \omega_\theta^2)(\omega_r^2 - 3\omega_\theta^2) + (\omega_r^2 + 3\omega_\theta^2)^2]^{\frac{1}{2}}\}/(2n)$	(+,-,1,1)
$f_{10}^2$	$\{(4n+3)(\omega_r^2 + \omega_\theta^2) - [4n(n+3)(\omega_\theta^2 - \omega_r^2)^2 + 9(\omega_r^2 + \omega_\theta^2)^2]^{\frac{1}{2}}\}/(2n)$	(-, -, 0, 4)
$f_{11}^2$	$\{(4n+3)(\omega_r^2 + \omega_\theta^2) + [4n(n+3)(\omega_\theta^2 - \omega_r^2)^2 + 9(\omega_r^2 + \omega_\theta^2)^2]^{\frac{1}{2}}\}/(2n)$	(-, -, 1, 2)

Table 2.2: Eigenfrequencies of the lowest order modes of the constant specific angular momentum slender torus. In the first column there are frequencies  $\sigma_0^2$  for various  $(P_x, P_y, j, k)$  whose values are expressed in the third column.

mode. Actually, it reduces to the acoustic ( $j = 1, k = 0$ ) mode in the limit of a torus with a constant specific angular momentum in the Newtonian  $\frac{1}{r}$  potential.

Table 2.1 shows the frequencies of all the lowest order modes of a general slender torus. Figure 2.2 shows the poloidal velocity fields for these modes while table 2.2 expresses the frequencies of modes for the special case of a constant specific angular momentum. Although it is still quite far from the Keplerian limit, the velocity fields show what happens in that case. The cross-mode frequency becomes degenerate with  $\omega_\theta$  in that limit, consisting of opposite vertical oscillations on either radial side of the pressure maximum. The breathing mode becomes degenerate with the lowest order vertical acoustic wave, as its velocity field becomes largely vertical. The inertial and plus modes consist largely of radial motions in the Keplerian limit, and become degenerate with  $\omega_r$ .

It is certain that the above procedure can be extended to calculate even higher order modes. In the special case of constant specific angular momentum tori, the dispersion relation remains quadratic for modes of quite high order. Nevertheless, higher order modes result in dispersion relations which are polynomials of cubic and higher order, and have to be solved numerically. The first step to do that is

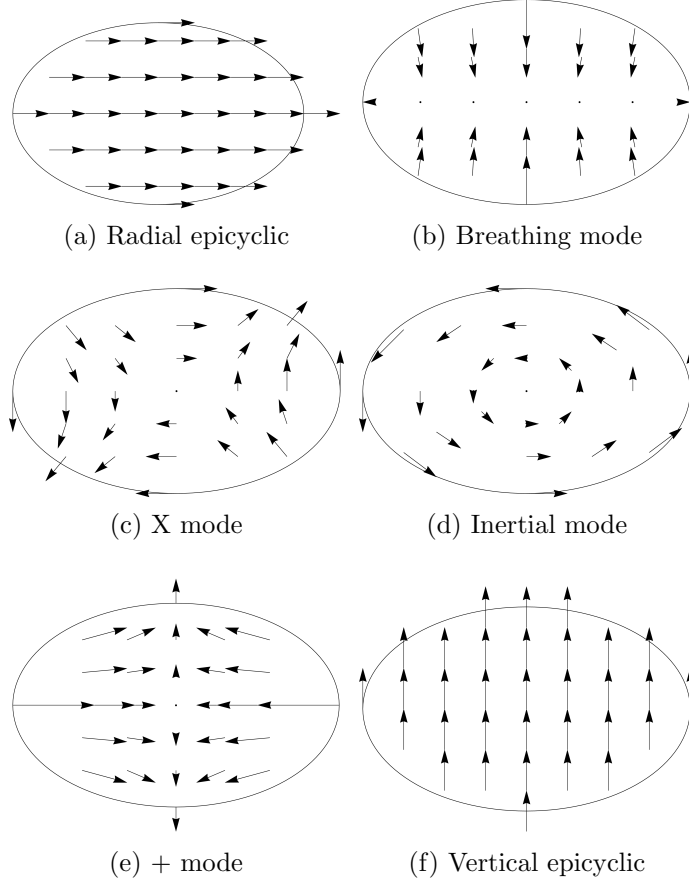


Figure 2.2: Poloidal velocity fields,  $\delta u_x$ ,  $\delta u_y$ , of the lowest order, nontrivial slender torus modes. The oval represents the poloidal cross-section of the slender torus. The arrows represent the direction and magnitude of the displacement vectors characteristic for each of the six corresponding modes.

to substitute the power-series expansion

$$\mathcal{W}(\tilde{x}, \tilde{y}) = \sum_{i,l=0}^{\infty} \mathcal{W}_{il} \tilde{x}^i \tilde{y}^l \quad (2.90)$$

in equation (2.74) and evaluate coefficients of  $\tilde{x}^i \tilde{y}^l$ . We obtain the following set of algebraic equations:

$$\begin{aligned} & \frac{\tilde{\sigma}_0^2}{\tilde{\sigma}_0^2 - \tilde{\kappa}_0^2} [(i+1)(i+2)\mathcal{W}_{i+2,l} - (\tilde{\omega}_r^2 - \tilde{\kappa}_0^2)i(i-1)\mathcal{W}_{il} \\ & - \tilde{\omega}_\theta^2(i+1)(i+2)\mathcal{W}_{i+2,l-2}] + (l+1)(l+2)\mathcal{W}_{i,l+2} \\ & - (\tilde{\omega}_r^2 - \tilde{\kappa}_0^2)(l+1)(l+2)\mathcal{W}_{i-2,l+2} - \tilde{\omega}_\theta^2 l(l-1)\mathcal{W}_{il} \\ & - 2n \frac{\tilde{\sigma}_0^2}{\tilde{\sigma}_0^2 - \tilde{\kappa}_0^2} (\tilde{\omega}_r^2 - \tilde{\kappa}_0^2)i\mathcal{W}_{il} - 2n\tilde{\omega}_\theta^2 l\mathcal{W}_{il} + 2n\tilde{\sigma}_0^2 \mathcal{W}_{il} = 0, \end{aligned} \quad (2.91)$$

which can be rewritten into matrix equation  $\mathbf{A}(\tilde{\sigma}_0)\mathcal{W} = 0$ , defining the matrix  $\mathbf{A}$ . Equation (2.91) can be solved using basis vectors for  $i = i_1 + 2(I - 1)$  and  $l = l_1 + 2(L - 1)$ , where  $I = 1, \dots, I_{max}$ ,  $L = 1, \dots, L_{max}$ . Here  $i_1 = 0$  for even  $P_x$  and 1 for odd  $P_x$ , while  $l_1 = 0$  for even  $P_y$  and 1 for odd  $P_y$ .

# 3. Method: General Relativistic MHD for axisymmetric accretion

In astrophysics, as opposed to other branches of physics, we cannot influence the object of our study, hence, we can do only observations and not experiments. However, we can substitute experiments by analytical calculations and numerical simulations. Real physical systems are enormously complex and, therefore, analytical calculations are limited to the simplest cases with many approximations taken into account. Numerical simulations have also some limitations, but together with observations and analytical calculations they offer a relevant tool for investigating astrophysical phenomena.

In this chapter I present theoretical and numerical schemes for 2D GRMHD model of accretion. These schemes are adopted in the HARM-2D code developed by (Gammie et al. 2003) which we used for our own simulations, based on solving GRMHD equations for magnetised tori, presented in Chapter 4. HARM is a program that solves hyperbolic partial differential equations in a conservative form using high-resolution shock-capturing techniques. It was configured to solve the relativistic magnetohydrodynamical equations of motion on a stationary black hole spacetime. We added new features into this code, e.g., we set the initial conditions to suit our torus models, the parameters of the Kerr spacetime background are evolved due to the accreted matter feedback, and repetitive disturbances of the torus may be applied.

## 3.1 Theoretical framework for magnetised 2D models

The evolution equations in the conservative scheme can be written as (Tóth 1998)

$$\partial_t \vec{U}(\vec{P}) + \partial_i \vec{F}^i(\vec{P}) = \vec{S}(\vec{P}), \quad (3.1)$$

where  $\vec{U}$  represents the vector of “conserved” variables, such as particle number density, energy density and momentum density. The vector  $\vec{F}$  denotes fluxes,  $\vec{S}$  is the vector of source terms that does not involve derivatives of  $\vec{P}$  and, therefore, it does not affect the characteristic structure of the system and  $\partial_i$  represents the spatial derivatives ( $i = 1,2,3$ ). In the case when  $\vec{S} = \vec{0}$ , the meaning of the conserved variables is obvious because the change rate of the integral of  $\vec{U}$  over the volume depends only on fluxes at boundaries, according to the divergence theorem.  $\vec{P}$  is the vector of “primitive” variables (rest-mass density, internal energy density, components of velocity and magnetic field). Fluxes and conserved variables depend on  $\vec{P}$ . Conservative numerical schemes advance  $\vec{U}$  and then calculate  $\vec{P}(\vec{U})$  once or twice per time step depending on the order of the particular scheme.

The conserved quantities are trivially related to the primitive variables in nonrelativistic conservative MHD schemes. The forward transformation,  $\vec{P} \rightarrow$

$\vec{U}$ , and also the inverse transformation,  $\vec{U} \rightarrow \vec{P}$ , have a closed-form solution. However,  $\vec{U}(\vec{P})$  is a complicated non-linear relation in GRMHD and the inverse transformation has no closed-form solution and, therefore, it must be treated numerically.

We adopt geometrized units,  $c = G = 1$ , throughout the whole chapter (unless stated otherwise) and assume the metric of the signature  $-, +, +, +$ . We will also use the following numbering of coordinates:  $(t, r, \vartheta, \varphi) \rightarrow (0, 1, 2, 3)$ .

The normal observer's (Zero Angular Momentum Observer) four-velocity is

$$n_\mu = (-\alpha, 0, 0, 0) \quad (3.2)$$

in coordinates  $t, x_1, x_2, x_3$ . For the lapse function  $\alpha$  one can write

$$\alpha^2 = -\frac{1}{g^{tt}}. \quad (3.3)$$

It is not trivial to see that  $\alpha$  in equation (3.2) has the meaning of the lapse function which is usually defined as

$$\alpha^2 \equiv -g_{t\varphi}\omega - g_{tt}, \quad (3.4)$$

where

$$\omega \equiv -\frac{g_{t\varphi}}{g_{\varphi\varphi}}. \quad (3.5)$$

Let us show at this place that the  $\alpha$  in equation (3.3) is the lapse function defined in equation (3.4). The contravariant indices of the normal observer's four-velocity can be written as

$$n^\mu = (n^t, 0, 0, n^\varphi), \quad (3.6)$$

where  $n^\varphi = n^t\omega$ . From the normalization condition for a four-velocity,

$$g_{\mu\nu}n^\mu n^\nu = -1, \quad (3.7)$$

it follows that

$$n^t = \sqrt{-\frac{1}{g_{tt} + g_{t\varphi}\omega}}. \quad (3.8)$$

For the covariant indices one can write

$$n_t = g_{t\mu}n^\mu = g_{tt}n^t + g_{t\varphi}n^t\omega \quad (3.9)$$

and

$$n_\varphi = g_{\varphi\mu}n^\mu = g_{\varphi\varphi}n^t\omega. \quad (3.10)$$

Using the definition of the lapse function in equation (3.4) we can rewrite equation (3.9) as

$$n_t = -\alpha^2 n^t. \quad (3.11)$$

Realizing that  $n^t = n_t g^{tt}$  we obtain

$$\alpha = \sqrt{-\frac{n_t}{n^t}} = \sqrt{-\frac{1}{g^{tt}}}. \quad (3.12)$$

We have just showed that equation (3.3) is consistent with the definition of the lapse function (3.4).

The dynamics of an ideal fluid can be described by its four-velocity  $u^\mu$ , rest mass density  $\rho_0$ , internal energy per unit proper volume  $u$  and pressure  $p$ . Electromagnetic field is characterized by the antisymmetric field tensor  $F^{\mu\nu}$  and its dual which is defined as (Gammie et al. 2003)

$$*F^{\mu\nu} \equiv \frac{1}{2}\epsilon^{\mu\nu\kappa\lambda}F_{\kappa\lambda}, \quad (3.13)$$

where  $\epsilon^{\mu\nu\kappa\lambda} \equiv -\frac{1}{\sqrt{-g}}[\mu\nu\kappa\lambda]$  is the Levi-Cevita tensor. Imposing the ideal MHD condition

$$u_\mu F^{\mu\nu} = 0, \quad (3.14)$$

which says that the Lorentz force vanishes in the rest frame of the fluid, the magnetic field tensor retains only three independent components. Accordingly, it is convenient to describe the magnetic field by the magnetic field four-vector  $\tilde{B}^\mu \equiv -n_\nu *F^{\mu\nu}$ . The vector  $\tilde{B}^\mu$  is related to the magnetic field vector  $B^i$  according to the relation

$$B^i \equiv *F^{it} = \frac{\tilde{B}^i}{\alpha}. \quad (3.15)$$

We can define projection tensors

$$h_{\mu\nu} \equiv g_{\mu\nu} + u_\mu u_\nu, \quad (3.16)$$

which projects to the space perpendicular to the four-velocity  $u_\mu$ , and

$$j_{\mu\nu} \equiv g_{\mu\nu} + n_\mu n_\nu, \quad (3.17)$$

which projects to the space perpendicular to the normal observer's four-velocity  $n^\mu$ . The set of GRMHD equations is given by

$$T^\mu_{\nu;\mu} = 0, \quad (3.18)$$

representing the conservation of the energy-momentum tensor, together with the conservation of the particle number,

$$(\rho_0 u^\mu)_{;\mu} = 0, \quad (3.19)$$

and Maxwell's equations

$$*F^{\mu\nu}_{;\nu} = 0. \quad (3.20)$$

We consider that the pressure  $p$  and the density of internal energy  $u$  satisfy the gamma law ( $\Gamma$ -law) with the equation of state

$$p = (\Gamma - 1)u. \quad (3.21)$$

Let us switch our attention to the issue what should our energy-momentum tensor look like. First of all, it is obvious that it consists of two parts:

$$T^{\mu\nu} = T^{\mu\nu}_{fluid} + T^{\mu\nu}_{elmag}. \quad (3.22)$$

In a general meaning, the electromagnetic part of the energy-momentum tensor is defined as follows:

$$T_{elmag}^{\mu\nu} \equiv F^{\mu\lambda} F_{\lambda}^{\nu} - \frac{1}{4} g^{\mu\nu} F^{\lambda\delta} F_{\lambda\delta}. \quad (3.23)$$

Moreover,  $*F^{\mu\nu}$  can be taken instead of  $F^{\mu\nu}$  in this definition. For the dual of the electromagnetic field tensor we can write:  $*F^{\mu\nu} = (n^{\mu} \tilde{B}^{\nu} - n^{\nu} \tilde{B}^{\mu})$ . Taking into account the above assumptions we get the following relation for the electromagnetic part of the energy-momentum tensor:

$$T_{elmag}^{\mu\nu} = \frac{(n^{\mu} \tilde{B}^{\lambda} - n^{\lambda} \tilde{B}^{\mu})(n^{\nu} \tilde{B}_{\lambda} - n^{\lambda} \tilde{B}_{\nu})(-n_{\mu} u^{\mu})(-n_{\nu} u^{\nu})}{\gamma \cdot \gamma} - \frac{1}{4} g^{\mu\nu} \frac{(n^{\lambda} \tilde{B}^{\delta} - n^{\delta} \tilde{B}^{\lambda})(n_{\lambda} \tilde{B}_{\delta} - n_{\delta} \tilde{B}_{\lambda})(-n_{\lambda} u^{\lambda})(-n^{\lambda} u_{\lambda})}{\gamma \cdot \gamma}, \quad (3.24)$$

where we used the expression for the Lorenz factor of the flow measured in the normal observer's frame

$$\gamma \equiv -n_{\mu} u^{\mu}. \quad (3.25)$$

Generally, it is possible to put some additional constant in equation (3.24) but it has no impact (the right hand side of the equation of conservation is zero), hence, we do not write it here. Using the identity  $\tilde{B}^{\mu} n_{\mu} = 0$  we can rewrite equation (3.24) as

$$T_{elmag}^{\mu\nu} = b^2 u^{\mu} u^{\nu} + \frac{1}{2} g^{\mu\nu} b^2 - b^{\mu} b^{\nu}, \quad (3.26)$$

where  $b^{\mu} \equiv h^{\mu}_{\nu} \frac{\tilde{B}^{\nu}}{\gamma}$  (see (42) in Appendix for further details). We can write the following prescription for the energy-momentum tensor of an ideal fluid:

$$T_{fluid}^{\mu\nu} = (\rho_0 + u + p) u^{\mu} u^{\nu} + p g^{\mu\nu} \quad (3.27)$$

and, consequently, the energy-momentum tensor of an ideal magnetised fluid is

$$T^{\mu\nu} = (w + b^2) u^{\mu} u^{\nu} + \left( p + \frac{b^2}{2} \right) g^{\mu\nu} - b^{\mu} b^{\nu}, \quad (3.28)$$

where  $w \equiv \rho_0 + u + p$ . Hereafter the primitive variables are:  $\rho_0, u, \tilde{B}^i$  and  $\tilde{u}^i \equiv j^i_{\mu} u^{\mu}$ . Adopting  $\tilde{u}^i$  is numerically convenient because it ranges from  $-\infty$  to  $+\infty$ . Note that  $\tilde{u}^t = 0$ . Our goal is to express conservation laws in terms of conserved variables  $\vec{U}$ , fluxes  $\vec{F}$  and source terms  $\vec{S}$ . It is easy to see that

$$T^{\mu}_{\nu;\mu} = 0 \Rightarrow \sqrt{\frac{1}{-g}} (\sqrt{-g} T^{\mu}_{\nu})_{;\mu} = -\Gamma_{\nu\rho\sigma} T^{\rho\sigma}, \quad (3.29)$$

which can be readily rewritten as

$$\partial_t (\sqrt{-g} T^t_{\mu}) + \partial_i (\sqrt{-g} T^i_{\mu}) = -\sqrt{-g} T^{\kappa}_{\lambda} \Gamma^{\lambda}_{\mu\kappa}. \quad (3.30)$$

The associated conserved variable is  $\sqrt{-g} T^t_{\mu}$ , however, it is convenient for future purposes to introduce a new conserved variable  $Q_{\mu}$ ,

$$Q_{\mu} \equiv -n_{\nu} T^{\nu}_{\mu} = \alpha T^t_{\mu}, \quad (3.31)$$

which characterizes the energy and momentum densities in the normal observer's frame. We get from the Maxwell's equations (note that  $*F^{\mu\nu} = \tilde{B}^\nu n^\mu - \tilde{B}^\mu n^\nu$ ):

$$*F^{0i}_{;i} = B^i_{;i} = 0, \quad (3.32)$$

which is the condition of the zero magnetic field divergence, and

$$*F^{i\mu}_{;\mu} = *F^{i0}_{;0} + *F^{ij}_{;j} = (n^i \tilde{B}^0 - n^0 \tilde{B}^i)_{;0} + (n^i \tilde{B}^j - n^j \tilde{B}^i)_{;j} = 0. \quad (3.33)$$

It follows from the last equation that

$$\left(\frac{\tilde{B}^i}{\alpha}\right)_{;t} + (n^i \tilde{B}^j - n^j \tilde{B}^i)_{;j} = 0$$

and

$$\partial_t(\sqrt{-g}B^i) = -\partial_j[\sqrt{-g}(u^i b^j - u^j b^i)], \quad (3.34)$$

where we used  $\tilde{B}^i = \gamma b^\mu h^i{}_\mu = \gamma b^i$  and  $\gamma \equiv -n_\mu u^\mu = -n_t u^t$  (in the normal observer's frame). Finally, there is the particle number conservation law

$$\partial_t(\sqrt{-g}\rho_0 u^t) = -\partial_j(\sqrt{-g}\rho_0 u^j). \quad (3.35)$$

The conserved variable for this equation is  $\sqrt{-g}\rho_0 u^t$  but, as in the previous case, it is convenient to introduce a new conserved variable  $D$  which we define as  $D \equiv -\rho_0 n_\mu u^\mu = \rho_0 \alpha u^t = \gamma \rho_0$ . This variable represents the mass density measured by the normal observer. We have 8 conserved variables so far:  $Q_\mu$ ,  $D$  and  $\tilde{B}^i$ . The transformation  $U(P)$  is already known:

$$p = (\Gamma - 1)u, \quad (3.36)$$

$$w = \rho_0 + u + p, \quad (3.37)$$

$$\gamma = (1 + g_{ij}\tilde{u}^i\tilde{u}^j), \quad (3.38)$$

$$u^\mu = \left(\frac{\gamma}{\alpha}, \tilde{u}^i - \alpha\gamma g^{ti}\right) \quad (3.39)$$

and

$$b^\mu = h^\mu{}_\nu \frac{\tilde{B}^\nu}{\gamma}. \quad (3.40)$$

Then we can evaluate  $D$  and  $Q_\mu$ :

$$D = \gamma\rho_0, \quad (3.41)$$

$$Q_\mu = \gamma(w + b^2)u_\mu - \left(p + \frac{b^2}{2}\right)n_\mu + (n_\nu b^\nu)b_\mu. \quad (3.42)$$

$D$ ,  $Q_\mu$  and  $\tilde{B}^i$  are both conserved and primitive variables. It will be useful to use following identities later in this chapter:

$$b^2 = \frac{1}{\gamma^2}[\tilde{B}^2 + (\tilde{B}^\mu u_\mu)^2] \quad (3.43)$$

and

$$n_\mu b^\mu = -u_\mu \tilde{B}^\mu. \quad (3.44)$$

We have the set of five equations that need to be solved (one for  $D$  and four for  $Q_\mu$ ). In order to solve these equations, it is convenient to evaluate some scalars from the conserved variables so that we would reduce the dimensionality of our set of equations. We will calculate following scalars:  $D$ ,  $Q_\mu \tilde{B}^\mu$ ,  $Q^\mu n_\mu$  and  $\tilde{Q}^2$ , where  $\tilde{Q}^\nu \equiv j^\nu_\mu Q^\mu$ . Moreover, we will use definitions  $\mathcal{W} \equiv w\gamma^2$  and  $v^i \equiv \frac{\tilde{u}^i}{\gamma}$ . Adopting these new variables leads to the significant simplification of equations and to the more robust numerical scheme.

Evaluating the above mentioned scalars (for details see (44) and (45) in Appendix) we get:

$$\tilde{B}^\mu Q_\mu = \frac{W}{\gamma}(u_\mu \tilde{B}^\mu), \quad (3.45)$$

$$Q_\mu n^\mu = -\frac{\tilde{B}^2}{2}(1+v^2) + \frac{(\tilde{B}^\mu Q_\mu)^2}{2W^2} - W + p. \quad (3.46)$$

One can easily see that

$$\tilde{Q}^\mu \tilde{Q}_\mu = (Q^\mu + n^\mu Q^\nu n_\nu)(Q_\mu + n_\mu n_\nu Q^\nu) = Q^2 + (n_\mu Q^\mu)^2. \quad (3.47)$$

In order to get the expression for  $\tilde{Q}^2$  we must evaluate  $(n_\mu Q^\mu)^2$  and  $Q^2$ . The first term can be obtained from eq. (3.46) by a simple multiplication:

$$\begin{aligned} (n_\mu Q^\mu)^2 &= \frac{\tilde{B}^4}{4}(1+v^2)^2 + \frac{(\tilde{B}^\mu Q_\mu)^4}{4W^4} + (p-W)^2 \\ &\quad - (1+v^2)\frac{\tilde{B}^2(\tilde{B}^\mu Q_\mu)^2}{2W^2} - \tilde{B}^2(1+v^2)(p-W) + \frac{(\tilde{B}^\mu Q_\mu)^2}{W^2}(p-W). \end{aligned} \quad (3.48)$$

For the second term,  $Q^2$ , one can write

$$\begin{aligned} Q_\mu Q^\mu &= -W^2(1-v^2) + 2Wp - p^2 + \tilde{B}^2 \left( -\frac{W}{\gamma^2} + p(1+v^2) - \frac{(\tilde{B}^\mu Q_\mu)^2}{2W^2\gamma^2} \right) \\ &\quad + \frac{(\tilde{B}^\mu Q_\mu)^2\gamma^2}{W^2} \left( -\frac{W}{\gamma^2} + p(v^2-1) \right) - \frac{1}{4\gamma^4} \left( \tilde{B}^4 + \frac{(\tilde{B}^\mu Q_\mu)^4\gamma^4}{W^4} \right). \end{aligned} \quad (3.49)$$

See (46) in Appendix for further details. If we put equations (3.49) and (3.48) into equation (3.47), we find the expression for  $\tilde{Q}^2$ :

$$\tilde{Q}^2 = v^2(\tilde{B}^2 + W)^2 - \frac{(Q_\mu \tilde{B}^\mu)^2(\tilde{B}^2 + 2W)}{W^2}. \quad (3.50)$$

The square of the velocity  $v^2$  can be derived from equation (3.50) as

$$v^2 = \frac{\tilde{Q}^2 W^2 + (Q_\mu \tilde{B}^\mu)^2(\tilde{B}^2 + 2W)}{(\tilde{B}^2 + W)^2 W^2}. \quad (3.51)$$

Various methods can be applied in order to get the final solution. The  $1D_W$  scheme solves one non-linear algebraic equation (3.46), which is a function of  $W$ , while equation (3.51) is used to eliminate  $v^2$ . When we already know  $v^2$  and  $W$ , it is straightforward to find  $w$ ,  $\rho_0$  and  $u$ .

Finally, we need to find  $\tilde{u}^i$ . It is useful to evaluate  $\tilde{Q}^i$  first:

$$\begin{aligned}
\tilde{Q}^\mu &\equiv j^{\mu\nu} Q_\nu = \gamma(w + b^2)j^{\mu\nu}u_\nu + (n_\mu b^\mu)b_\nu j^{\mu\nu} \\
&= \frac{1}{\gamma}(W + \tilde{B}^2)\tilde{u}^\mu + \frac{(\tilde{B}^\mu u_\mu)^2}{\gamma}u_\nu j^{\mu\nu} + (u_\mu \tilde{B}^\mu)^2 n^\mu - \frac{u_\mu \tilde{B}^\mu}{\gamma}h^\mu{}_\nu \tilde{B}^\nu \\
&= \frac{1}{\gamma}(W + \tilde{B}^2)\tilde{u}^\mu - \frac{(u_\nu \tilde{B}^\nu)}{\gamma}\tilde{B}^\mu.
\end{aligned} \tag{3.52}$$

Now, if we take into account equation (3.45), we obtain the expression for  $\tilde{u}^i$ :

$$\tilde{u}^i = \frac{\gamma}{W + \tilde{B}^2} \left( \tilde{Q}^i + \frac{(Q_\mu \tilde{B}^\mu) \tilde{B}^i}{W} \right). \tag{3.53}$$

Equation (3.46), which is solved in  $1D_W$  scheme, includes a quotient of polynomials in  $W$ . This can be the source of numerical pathologies near roots. A feasible approach to the elimination of such problems is to solve two simpler equations (equations (3.46) and (3.50)) simultaneously for  $W$  and  $v^2$ . We call this method the  $2D$  scheme because it involves solving a two-dimensional algebraic system.

Using  $v^2$  instead of  $\tilde{u}^2$  or  $\gamma$  is suitable in this method, because equations (3.46) and (3.50) are linear just in  $v^2$  and not in  $\tilde{u}^2$  or  $\gamma$ . The linear dependence on  $v^2$  increases the rate of convergence for this quantity and it also guarantees good behaviour in the vicinity of a root.

## 3.2 Numerical scheme for magnetised 2D models

Several techniques were developed to integrate GRMHD equations numerically. The first choice we can do is to choose between conservative and non-conservative schemes. The conservative scheme is adopted in the HARM code. An undisputed advantage of this scheme is that, in one dimension, total variation stable schemes are guaranteed to converge to a weak solution by the Lax-Wendroff theorem (Lax & Wendroff 1960) and by a theorem of LeVeque (LeVeque 1997). While no such guarantee is available for multidimensional flows, this is a reassuring starting point. Furthermore, we are assured that the conservative scheme will satisfy the jump conditions at discontinuities in an arbitrary number of dimensions.

The conservative scheme updates a set of conserved variables at every time step. The vector of these conserved variables is defined as

$$\vec{U} \equiv \sqrt{-g}(\rho u^t, T^t, T^i, B^i). \quad (3.54)$$

These variables are updated by using fluxes  $\vec{F}$ . It is also necessary to select a set of primitive variables, which are interpolated so as to model the flow within computational zones. It is useful to pick out variables with a simple physical interpretation:

$$\vec{P} = (\rho, u, v^i, B^i), \quad (3.55)$$

where  $v^i = \frac{u^i}{u^t}$  is the 3-velocity. The functions  $\vec{U}(\vec{P})$  and  $\vec{F}(\vec{P})$  are analytic but the inverse operations are not. Furthermore, there is no simple expression for  $\vec{F}(\vec{U})$ .

Since we update  $\vec{U}$  instead of  $\vec{P}$ , we must solve  $\vec{P}(\vec{U})$  at the end of each time step. We use the multidimensional Newton-Raphson routine which takes the value of  $\vec{P}$  from the previous time step as an new initial guess. Since  $B^i$  can be obtained analytically, only five equations remain to be solved. The Newton-Raphson method requires an expensive computation of the Jacobian  $\frac{\partial \vec{U}}{\partial \vec{P}}$ , which is usually evaluated by numerical derivatives. This is not only expensive but it is a possible source of numerical noise too.

The evaluation of  $\vec{P}(\vec{U})$  is the crucial point of this numerical scheme. We use a MUSCL-type scheme with ‘‘HLL’’ fluxes (Harten et al. 1983) in order to evaluate  $\vec{F}$ . The fluxes are defined at zone faces. A slope-limited linear extrapolation from the zone centre gives the values of primitive variables at the right-hand and left-hand sides of every zone interface. The monotonized central limiter, the van Leer limiter and the minmod limiter are implemented in the HARM code.

Generally, a set of conservation laws with some additional source terms can be written as

$$\partial_t \vec{U} + \partial_i \vec{F}^i(\vec{U}) = \vec{S}(\vec{U}), \quad (3.56)$$

where  $\vec{U}$ ,  $\vec{F}$  and  $\vec{S}$  are vectors of conserved variables, fluxes and source terms. Symbol  $\partial_i$  represents the spatial derivative in direction  $i$  and the summation is implied over  $i = 1, 2, 3$ .

## TVD Lax-Friedrichs scheme

Total variation diminishing (TVD) schemes belong to the most popular methods for solving a hyperbolic set of PDEs. Although these schemes were developed and used mainly for compressible hydrodynamic simulations, their application to MHD is quite recent. Several variations and generalizations of TVD schemes exist, for example, the total variation bounded (TVB) or the essentially non-oscillatory (ENO) method, however, these are not discussed in this chapter. A number of variants occur even within the TVD family. Naturally, we concentrate on the simplest versions. The simplest TVD method is based on the first order Lax-Friedrichs scheme, which discretizes a conservation law according to the formula

$$\vec{U}_j^{n+1} = \vec{U}_j^n - \frac{\Delta t}{\Delta x} \left( \vec{F}_{j+\frac{1}{2}} - \vec{F}_{j-\frac{1}{2}} \right) + \frac{1}{2} \left( \vec{\phi}_{j+\frac{1}{2}} - \vec{\phi}_{j-\frac{1}{2}} \right), \quad (3.57)$$

where

$$\vec{F}_{j+\frac{1}{2}} = \frac{\vec{F}_j + \vec{F}_{j+1}}{2} \quad (3.58)$$

and

$$\vec{\phi}_{j+\frac{1}{2}} = \vec{U}_{j+1} - \vec{U}_j. \quad (3.59)$$

The last two terms in equation (3.57) add numerical diffusion that corresponds to the term  $\eta \nabla^2 \vec{U}$  with the diffusion coefficient  $\eta \propto \frac{(\Delta x)^2}{\Delta t}$ . Therefore, the Lax-Friedrichs scheme is only first order accurate. It can be also shown that the scheme is conditionally stable for Courant number  $C < 1$ . The numerical diffusion can be reduced using a diffusive flux

$$\vec{\phi}_{j+\frac{1}{2}} = \frac{\Delta t}{\Delta x} c_{j+\frac{1}{2}}^{max} (\vec{U}_{j+1} - \vec{U}_j), \quad (3.60)$$

where the local Courant number  $C = c_{j+\frac{1}{2}}^{max} \frac{\Delta t}{\Delta x}$  ( $c^{max}$  denotes the fastest wave speed) is used as a coefficient for the artificial diffusion. The scheme we have just described is the first order TVD Lax-Friedrichs scheme.

Another way to look at the numerical flux term  $\vec{\phi}$  is to realize that it modifies the centred flux difference formula to a one-sided upwinded difference formula, at least for a single linear equation like the continuity equation  $\frac{\partial \rho}{\partial t} + \nabla \cdot (\rho v) = 0$ . The maximum wave speed is  $c^{max} = |v|$  for a fixed velocity, hence, we can write:

$$\begin{aligned} \rho_j^{n+1} &= \rho_j^n - \frac{\Delta t}{2\Delta x} [(\rho v)_{j+1} - (\rho v)_{j-1}] + \frac{\Delta t}{2\Delta x} |v| (\rho_{j+1} - 2\rho_j + \rho_{j-1}) \\ &= \rho_j^n - \frac{\Delta t}{\Delta x} \begin{cases} (\rho v)_j - (\rho v)_{j-1} & \text{for } v \geq 0 \\ (\rho v)_{j+1} - (\rho v)_j & \text{for } v < 0. \end{cases} \end{aligned} \quad (3.61)$$

Using the upwinded difference formula is a feasible approach to solve the advection equation and, in general, hyperbolic equations because the physical information should propagate from the upstream direction.

Second order spatial accuracy can be achieved by the linear approximation of  $\vec{U}$  and the corresponding fluxes at the boundary interfaces. The value of  $\vec{U}$  at

the interface  $x_{j+\frac{1}{2}}$  can be linearly extrapolated from the left and right cell centre values as

$$\vec{U}_{j+\frac{1}{2}}^L = \vec{U}_j^n + \frac{1}{2} \overline{\Delta \vec{U}}_j^n$$

and

$$\vec{U}_{j+\frac{1}{2}}^R = \vec{U}_{j+1}^n - \frac{1}{2} \overline{\Delta \vec{U}}_{j+1}^n, \quad (3.62)$$

where the limited slopes  $\overline{\Delta \vec{U}}$  will be defined later. The fluxes at the cell interface are calculated as

$$\vec{F}_{j+\frac{1}{2}} = \frac{\vec{F}(\vec{U}_{j+\frac{1}{2}}^L) + \vec{F}(\vec{U}_{j+\frac{1}{2}}^R)}{2}, \quad (3.63)$$

$$\vec{\phi}_{j+\frac{1}{2}} = \frac{\Delta t}{\Delta x} c_{j+\frac{1}{2}}^{max} \left( \vec{U}_{j+\frac{1}{2}}^R - \vec{U}_{j+\frac{1}{2}}^L \right). \quad (3.64)$$

The diffusive flux  $\vec{\phi}$  is reduced because the difference between left and right extrapolations is proportional to  $(\Delta x)^2$  for a smoothly varying  $U$ . It still provides a proper upwinding for the flux difference formula. The maximum propagation speed can be defined as  $c_{j+\frac{1}{2}}^{max} = \max[c^{max}(\vec{U}_{j+\frac{1}{2}}^R), c^{max}(\vec{U}_{j+\frac{1}{2}}^L)]$ .

Temporally second order accuracy for the explicit time stepping can be achieved using two step Runge-Kutta discretization or a predictor-corrector scheme. Hancock's predictor step is probably the best choice. First a time centred

$$\vec{U}_j^{n+\frac{1}{2}} = \vec{U}_j^n - \frac{\Delta t}{2\Delta x} \left[ \vec{F}(\vec{U}_j^n + \frac{1}{2} \overline{\Delta \vec{U}}_j^n) - \vec{F}(\vec{U}_j^n - \frac{1}{2} \overline{\Delta \vec{U}}_j^n) \right] \quad (3.65)$$

is calculated and then it is used for the evaluation of linear extrapolations

$$\vec{U}_{j+\frac{1}{2}}^L = \vec{U}_j^{n+\frac{1}{2}} + \frac{1}{2} \overline{\Delta \vec{U}}_j^n$$

and

$$\vec{U}_{j+\frac{1}{2}}^R = \vec{U}_{j+1}^{n+\frac{1}{2}} - \frac{1}{2} \overline{\Delta \vec{U}}_{j+1}^n. \quad (3.66)$$

This is the spatially and temporally second order TVDLF scheme which is stable for the Courant number  $C < 1$ . Contributions of source terms can be easily added to the right hand side of equation (3.65). In multidimensional simulations  $\vec{U}^L$  and  $\vec{U}^R$  extrapolations should be determined for each interface, and the flux contributions can be added at the same time, however, this usually requires the Courant number  $C < 0.5$ .

## TVD-MUSCL scheme

The TVD-MUSCL scheme (MUSCL means the Monotonic Upstream Scheme for Conservation Laws) differs from the TVDLF scheme in such a way that the upwinding is applied for characteristic variables rather than for the conserved

variables. The characteristic variables  $\vec{r}^k$  are certain linear combination of the conserved variables that form the right eigenvectors of the matrix  $\frac{\partial \vec{F}}{\partial \vec{U}}$ , i.e.

$$\frac{\partial \vec{F}}{\partial \vec{U}} \vec{r}^k = c^k \vec{r}^k, \quad (3.67)$$

where  $c^k$  is the eigenvalue corresponding to the  $k$ -th eigenvector. For the linear system of hyperbolic PDEs, the characteristic waves consist of components  $\vec{r}^k$  that travel at the speed  $c^k$ . Hyperbolicity ensures that the eigenvectors and eigenvalues are real and form a complete orthogonal base. The normalized left eigenvectors  $\vec{l}^k$  are related to the right eigenvectors by the orthogonality relation  $\vec{l}^k \cdot \vec{r}^m = \delta_{k,m}$ . Now we can write for the numerical diffusive flux vector  $\vec{\phi}$ :

$$\vec{\phi} = \frac{\Delta t}{\Delta x} \sum_k \vec{r}^k |c^k| \vec{l}^k \cdot (\vec{U}^R - \vec{U}^L), \quad (3.68)$$

where  $\vec{r}^k$ ,  $c^k$ ,  $\vec{l}^k$  are calculated for the mean  $\vec{U}_{j+\frac{1}{2}}^{LR}$  state. The scalar product of the  $k$ -th left eigenvector with the term  $\vec{U}^R - \vec{U}^L$  determines the jump in the  $k$ -th characteristic variable, while the multiplication by  $\vec{r}^k$  transforms the result back to the conserved variables. The advantage in comparison with the much simpler TVDLF flux is the usage of the eigenvalue  $c^k$  instead of the largest eigenvalue  $c^{max}$ . Therefore, the upwinding is accurate for every characteristic variable, which causes the reduction of numerical diffusion. On the other hand, the left and right eigenvectors need to be calculated for each cell interface, which makes the computation quite demanding for the GRMHD equations.

## Slope limiters

The slopes of conserved variables  $\Delta \vec{U}$  are limited by the slope limiters  $\overline{\Delta \vec{U}}$  in the second order TVDLF and TVD-MUSCL schemes. The slope limiter is required to ensure the TVD property for the schemes. A lot of versions of slope limiters satisfy conditions for TVD property and second order accuracy for smooth solutions. Here we define only three of them: the minmod limiter, the van Leer limiter and the superbee limiter. We use the van Leer limiter in our computations that is defined as

$$\overline{\Delta \vec{U}}_j \equiv \text{minmod}(2\Delta \vec{U}_{j-\frac{1}{2}}, 2\Delta \vec{U}_{j+\frac{1}{2}}, \frac{1}{2}\Delta \vec{U}_{j-\frac{1}{2}} + \frac{1}{2}\Delta \vec{U}_{j+\frac{1}{2}}). \quad (3.69)$$

The definition of the minmod limiter is

$$\overline{\Delta \vec{U}}_j \equiv \text{minmod}(\Delta \vec{U}_{j-\frac{1}{2}}, \Delta \vec{U}_{j+\frac{1}{2}}) \quad (3.70)$$

and for the superbee limiter we can write

$$\overline{\Delta \vec{U}}_j \equiv s \max[0, \min(2|\Delta \vec{U}_{j+\frac{1}{2}}|, s\Delta \vec{U}_{j-\frac{1}{2}}), \min(|\Delta \vec{U}_{j+\frac{1}{2}}|, 2s\Delta \vec{U}_{j-\frac{1}{2}})], \quad (3.71)$$

where  $\Delta\vec{U}_{j+\frac{1}{2}} = \vec{U}_{j+1} - \vec{U}_j$ ,  $s = \text{sgn}(\Delta\vec{U}_{j+\frac{1}{2}})$  and generalized minmod function for argument  $n > 1$  is

$$\text{minmod}(w_1, w_2, \dots, w_n) \equiv \text{sgn}(w_1) \max[0, \min(|w_1|, \text{sgn}(w_1)w_2, \dots, \text{sgn}(w_1)w_n)]. \quad (3.72)$$

According to its definition, the minmod function takes the argument with the smallest modulus when all the arguments have the same sign and otherwise it is zero. The minmod limiter is rather diffusive, while the superbee limiter can sharpen smooth waves into discontinuities. In fact, the minmod and superbee limiters are most and least diffusive amongst all acceptable symmetric two-variable slope limiters. The van Leer limiter is between those two and it is often used as a good compromise.

# 4. Results: oscillations and destruction of magnetised tori

## 4.1 Toroidal magnetic field and the runaway instability

Toroidal equilibria of perfect fluid in permanent rotation were introduced a long time ago as an initial step on the way towards an astrophysically realistic description of accretion of gaseous material onto a black hole in active galactic nuclei and black hole binaries (Fishbone & Moncrief 1976; Abramowicz et al. 1978; Pugliese et al. 2013). These axially symmetric and stationary solutions are subject to various types of instability (Abramowicz & Fragile 2013). Here we concentrate on a global type of instability caused by an overflow of material over the cusp of a critical equipotential surface (Daigne & Mochkovitch 1997; Abramowicz et al. 1998; Korobkin et al. 2013). It was suggested that this may lead to specific features that should be observable in the radiation emitted from an accreting black-hole system (Zanotti et al. 2003). Our discussion in this section has been based on and it slightly expands the article Hamerský & Karas (2013).

The effect of the mentioned instability can be catastrophic under certain conditions. In particular, a black-hole torus becomes runaway unstable if the angular momentum profile within the torus does not rise sufficiently fast with radius (Abramowicz et al. 1998; Lu et al. 2000). The role of general relativity effects on the runaway mechanism was studied in Font & Daigne (2002) in the context of gamma-ray burst sources. These authors found that by allowing the mass of the black hole to grow by accretion, the disc becomes unstable. However, the parameter space of the problem is much richer than what could be taken into account in early works. For example, the self-gravity of the fluid tends to act against the stability of non-accreting tori (Goodman & Narayan 1988; Masuda et al. 1998; Montero et al. 2010; Korobkin et al. 2011). Furthermore, the spin parameter can play a role for accretion onto a rotating black hole. In astrophysically realistic models, an interplay of mutually competing effects have to be taken into account.

The role of magnetic fields is known to be essential for accretion. Even the Rayleigh-stable tori (Seguin 1975) with a radially increasing profile,  $dl/dR > 0$ , become dynamically unstable because of turbulence in the presence of a weak magnetic field (Balbus & Hawley 1991). Here we aim to clarify the simpler question of the global stability of a rotationally symmetric black-hole accretion tori, taking into account the effect of a large-scale (organized) magnetic field that obeys the same axial symmetry. Komissarov (2006) has developed a suitable analytical (toy) model of such a magnetised torus described by a polytropic equation of state in Kerr metric. In this model the magnetic field only enters the equilibrium solution for the torus as an additional pressure-like term (Pugliese & Montani 2013).

We employed this solution as an initial configuration, which we then perturbed

and evolved numerically by the HARM code (Gammie et al. 2003). A complementary approach in the context of gamma-ray bursts has been developed in Barkov & Baushev (2011), who adopted the same initial configuration of an axially symmetric magnetised torus, which they evolved taking self-gravity and neutrino cooling mechanisms into account. Although the basic idea behind the runaway instability has been well-known since the early papers (Abramowicz et al. 1983; Wilson 1984) — it is connected with the existence of the innermost stable circular orbit around black holes in general relativity — an interplay of different effects makes the discussion rather complex, and so simplified models have their value for understanding the runaway mechanism in astrophysically realistic systems.

Assuming axial symmetry is a useful simplification to explore the origin of runaway instability, although it is a far too strong constraint for any realistic model of an accreting system. Moreover, a purely toroidal structure of the magnetic field and complete negligence of radiative cooling are an over-simplification, which we adopt in this chapter. However, these assumptions allow us to concentrate on the particular type of the above-mentioned relativistic instability while non-axisymmetric modes are suppressed. It also helps us to proceed systematically through the parameter space of the model to reveal the dependence on black-hole spin and the magnetic field strength as they act concurrently within the relativistic scheme. In this respect our work is complementary to three-dimensional simulations (Korobkin et al. 2013; McKinney et al. 2012), which are more complete and, at the same time, more difficult to comprehend.

In sec. 4.1.1 we summarize our approach to magnetised tori and the numerical scheme used in our simulations. Then we present our results by comparing properties of magnetised and non-magnetised accretion tori that are subject to a weak perturbation from the equilibrium state. In sec. 5 we discuss our results and give a brief conclusion.

### 4.1.1 Initial configuration of the torus

Let us first assume the non-magnetised Abramowicz et al. (1978) model of accretion torus ( $l = \text{const.}$ ) with the polytropic equation of state:

$$\begin{aligned} p_g &= \kappa \rho_0^\gamma, \\ u &= \frac{p_g}{\gamma - 1}. \end{aligned} \quad (4.1)$$

For the special choice of  $\gamma = \frac{4}{3}$  and arbitrary  $\kappa$  ( $\kappa = 10^{-2}$  in our simulations), we can solve the right hand side of equation (2.42) analytically and write the result as

$$\ln U - \ln U_{in} = -\ln \left( 1 + 4\kappa^{\frac{3}{4}} p_g^{\frac{1}{4}} \right). \quad (4.2)$$

In our approach we need to express thermodynamical variables as a function of the metric only. Consequently, we rewrite the last equation into following form:

$$p_g = \left( \frac{U_{in}}{U} - 1 \right)^4 \frac{1}{4^4 \kappa^3}. \quad (4.3)$$

From equation (4.3) we can obtain the value of pressure at each point of the torus and via equations (4.1) the rest mass density and density of internal energy too.

If we want to prescribe magnetic field in the torus, we must solve equation (2.50) that is more complicated compared to equation (2.42). Indeed, we could solve this equation numerically but it would be a next possible source of numerical noise. Therefore, we impose the relation between both integrals in equation (2.50) so that

$$\int_0^{P_g} \frac{dp_g}{w} = C \cdot \int_0^{\tilde{P}_m} \frac{d\tilde{p}_m}{\tilde{w}}, \quad (4.4)$$

where  $C$  is a constant that sets the mutual relation between hydrodynamic and magnetic effects. Since  $C$  determines the mutual relation between the hydrodynamic and the magnetic pressure components, its value indirectly influences also the magnetization ratio  $\beta \equiv \frac{P_g}{P_m}$  (the equipartition state is reached for  $\beta$  near unity, whereas  $\beta \gg 1$  represents a sub-equipartition magnetic field). The solution of the first integral is already known and so the equation (2.50) reduces to

$$\ln \left( \frac{U_{in}}{U} \right) = \left( 1 + \frac{1}{C} \right) \ln \left( 1 + 4\kappa^{\frac{3}{4}} p_g^{\frac{1}{4}} \right), \quad (4.5)$$

from which it follows that

$$p_g = \left[ \left( \frac{U_{in}}{U} \right)^{\frac{C}{C+1}} - 1 \right]^4 \frac{1}{4^4 \kappa^3}. \quad (4.6)$$

Since we need to know the magnetic pressure at each point of the torus, we must impose the dependence of  $\tilde{p}_m$  on  $\tilde{w}$ . From equation (2.46) it is obvious that the last term is a total differential and so one can write

$$\tilde{p}_m = K_m \tilde{w}^\eta, \quad (4.7)$$

where  $K_m$  and  $\eta$  are constants. Now it is easy to see that

$$\int_0^{\tilde{P}_m} \frac{d\tilde{p}_m}{\tilde{w}} = \frac{\eta}{\eta-1} K_m^{\frac{1}{\eta}} \tilde{p}_m^{\frac{\eta-1}{\eta}}. \quad (4.8)$$

Since we have analytically evaluated both integrals, we can rewrite  $\tilde{p}_m$  in terms of  $p_g$ . We get following expression:

$$\tilde{p}_m = \left[ \frac{1}{const.} \frac{\eta-1}{\eta} K_m^{-\frac{1}{\eta}} \ln \left( 1 + \frac{p_g^{\frac{1}{4}}}{\frac{1}{4} \cdot \kappa^{-\frac{3}{4}}} \right) \right]^{\frac{\eta}{\eta-1}}. \quad (4.9)$$

One can see that there are three free parameters:  $C$ ,  $\eta$  and  $K_m$ . We must be very careful which values of these parameters we take. For some special choices of these parameters we can get too big gradients of magnetic field which cause a numerical noise. In our computations we adopted these values:  $C = 100$ ,  $\eta = \frac{4}{3}$ . Changing the value of  $K_m$  we were getting different ratios of thermodynamical pressure to magnetic pressure  $\beta$ .

So far, we assumed that the angular momentum density is constant inside the torus. Unless this condition is fulfilled we have to solve equation (2.51). This leads to the solution for the gas pressure in the form

$$p_g = A\kappa^{-3} \left[ \left( \frac{u_{t_{\text{in}}}}{u_t} \exp \int_0^l \frac{\Omega dl}{1 - \Omega l} \right)^{\tilde{C}} - 1 \right]^4, \quad (4.10)$$

where  $A = 0.0039$  and  $\tilde{C} = C/(1+C)$  are constants, and  $p_g = \kappa\rho^\gamma$  is the assumed form of equation of state with the polytropic index  $\gamma = 4/3$  (Abramowicz & Fragile 2013).

We focus on critical tori that develop the relativistic cusp at the inner edge,  $R = R_{\text{in}}$ , where the angular momentum is equal to the Keplerian angular momentum at the corresponding radius in the common equatorial plane of the black hole and the torus ( $\vartheta = \pi/2$ ). The mass accretion can either bring the system out of the critical configuration and stabilise it with an updated set of model parameters and a modified profile of angular momentum, or the accretion process continues in a runaway mode and leads to a complete destruction of the torus. An exemplary profile of such a torus is shown in Figure 4.1, where contours of constant mass density are constructed from the analytical form of the solution (4.10). The contours are over-plotted on top of the colour-coded density structure. The black hole is located towards the left side of the plot; the coordinates are defined in such a way that the entire left edge of the plot corresponds to the location of the outer horizon at  $r = r_+$ . The bottom panel shows the same configuration in Boyer-Lindquist coordinates  $(r, \vartheta)$ . The torus surface extends from the inner rim at  $r = 4.5$  up to the outer boundary at  $r = 8.4$  in the equatorial plane,  $y = 0$ . The right edge is at  $x = 15$ ; Cartesian coordinates are derived from Boyer-Lindquist coordinates,  $x^2 + y^2 = r^2$  ( $x = r \sin \vartheta$ ,  $y = r \cos \vartheta$ ) and scaled with units of  $GM_\bullet/c^2$ . The colour bar is scaled logarithmically with values of normalized rest-mass density  $\rho(x, y)$  relative to its maximum value  $\rho_c$  at the torus centre ( $x = R_c = 6.3$ ,  $y = 0$ ). In the bottom panel the horizon is located at  $\sqrt{x^2 + y^2} = 1.95$ , so it is hidden behind the left border of the graph.

We notice that the constant density and pressure contours from eq. (4.10) correspond accurately to the colour scale of the image. Since the latter is based on a direct output from the numerical code, we can be confident that the computed structure and the necessary transformations of the coordinates are correct. This is a reassuring check before we embark on the time evolution of a perturbed configuration, where the analytical calculation is not available.

Let us note that the HARM code (Gammie et al. 2003) defines radial and latitudinal coordinates in a way that helps resolving the plunging region near above the black-hole horizon. On the other hand, the sharp inner cusp of the critical configuration is revealed more clearly in standard Boyer-Lindquist coordinates. Figure 4.1 compares the torus structure in both types of coordinates.

### 4.1.2 Time evolution of perturbed torus

We assume that the above-described initial stationary state is pushed out of equilibrium. This leads to the capture of a small amount of material by the

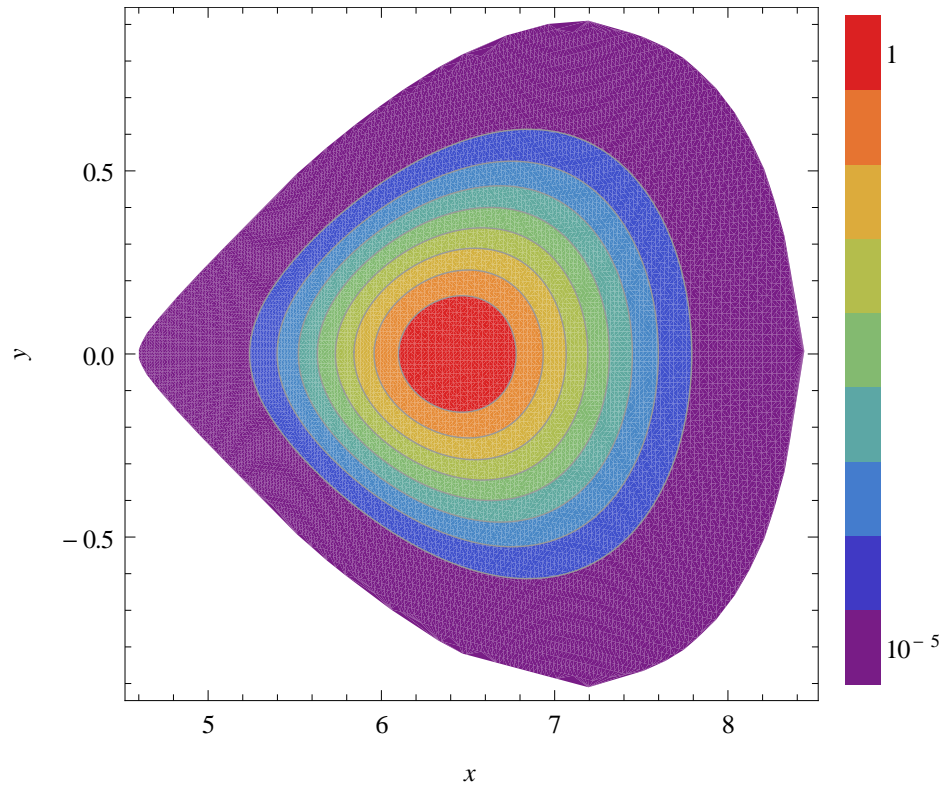
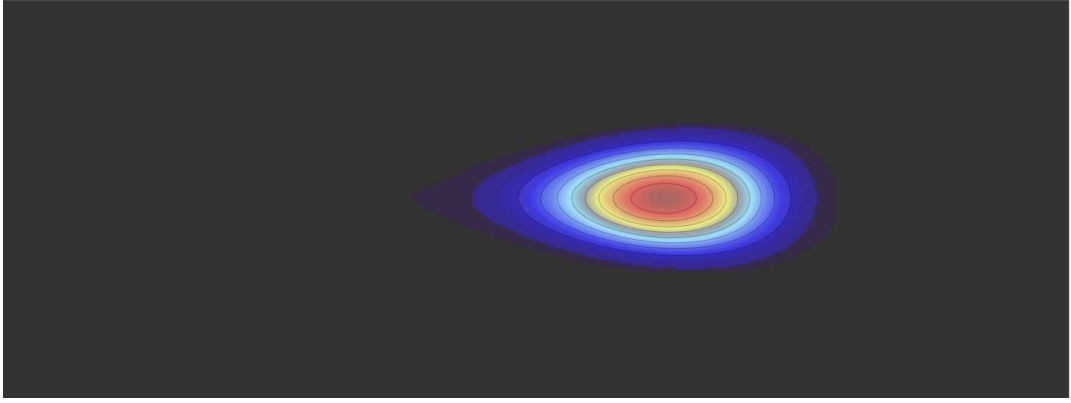


Figure 4.1: Stationary distribution of mass across the meridional section of the equilibrium non-magnetised torus in Kerr metric ( $a = 0.3$ ; the case of a purely hydrodynamical torus). The top panel shows the shape and the density structure in the poloidal coordinates as defined in the HARM code (Gammie et al. 2003), and the same configuration is drawn for Boyer-Lindquist coordinates in the bottom panel. See the text for details.

black hole, which increases the black-hole mass, and so the accretion occurs. Abramowicz et al. (1998) argued that tori with radially increasing angular momentum density are more stable. Therefore, we started with  $q > 0$  (see Figure 4.2) and concentrated on the influence of the magnetic field on the accretion rate.

The algorithm of the numerical experiment proceeds as follows. At the initial step the mass of the black hole was increased by a small amount, typically by about few percent. After the time step  $\delta t$ , the elementary mass  $\delta M$  and angular momentum  $\delta L = l(R_{\text{in}}) \delta M$  are accreted across the horizon,  $r = r_+ \equiv [1 + \sqrt{1 - a^2}] GM_{\bullet}/c^2$ . The mass increase  $\delta M$  is computed as a difference of the mass of torus  $M_{\text{d}} = \int_{\mathcal{V}} \rho d\mathcal{V}$  at  $t$  and  $t + \delta t$ , where  $d\mathcal{V} = u^t \sqrt{-g} d^3x$  is taken over the spatial volume occupied by the torus. The corresponding elementary spin increase is  $\delta a = l \delta M / (M_{\bullet} + \delta M)$ . Therefore, at each step of the simulation we updated the model parameters by the corresponding low values of mass and angular momentum changes:  $M_{\bullet} \rightarrow M_{\bullet} + \delta M$ ,  $a \rightarrow a + \delta a$ . The inner cusp moves accordingly.

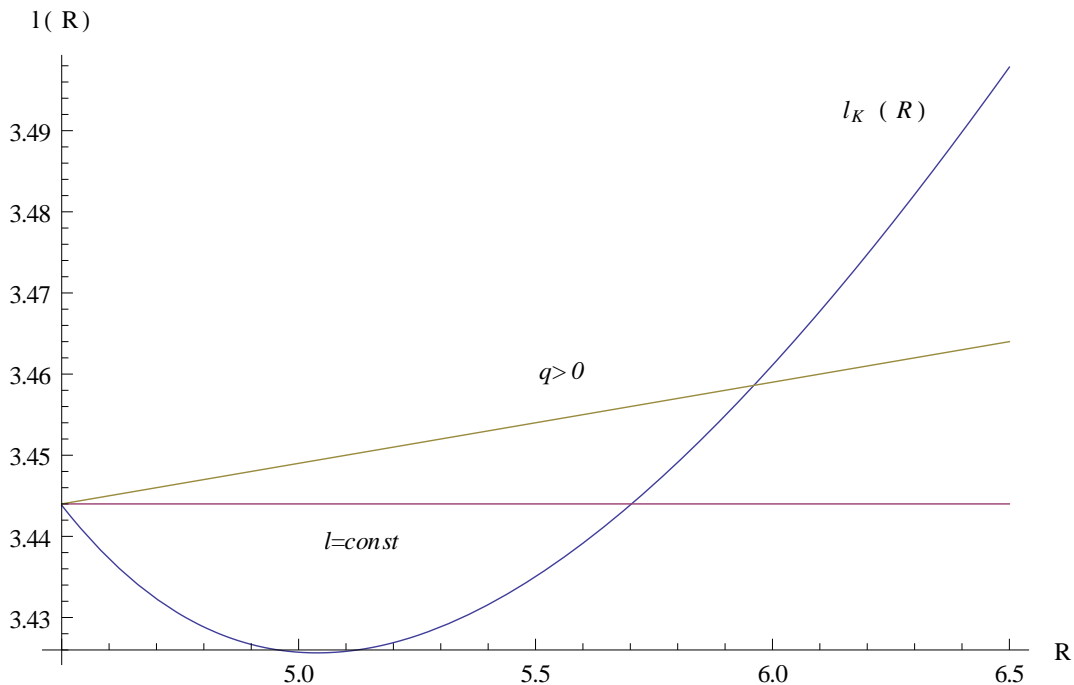


Figure 4.2: Schematic graph of the angular momentum radial profile of the material inside the accretion torus. At the inner edge ( $R_{\text{in}} = 4.5GM_{\bullet}/c^2$ ) of the matter configuration the angular momentum is equal to the Keplerian value,  $l = l_{\text{K}}(R_{\text{in}})$ . The relativistic Keplerian angular momentum distribution first decreases with the radius, passes through a minimum, and then grows  $\propto R^{1/2}$  asymptotically at large radii. The constant value,  $l = \text{const}$ , corresponds to the marginally stable configuration, which has been often discussed in the context of geometrically thick discs. The radially growing profile ( $q > 0$ ) improves the stability of the accretion flow.

We employed geometrized units, setting the speed of light and the gravitational constant equal to unity,  $c = G = 1$ . This implies the scaling of various

quantities with the central black-hole mass  $M_\bullet$ . However, the mass as well as the spin parameter evolve gradually (adiabatically) as the accretion of material proceeds from the torus,  $M_\bullet \equiv M_\bullet(t)$ ,  $a \equiv a(t)$ . Corresponding quantities in physical units are obtained by the following conversions:

$$\frac{M^{\text{phys}}}{M_\odot^{\text{phys}}} = \frac{M}{1.477 \times 10^5 \text{cm}}, \quad a^{\text{phys}} = ca, \quad R^{\text{phys}} = R. \quad (4.11)$$

Also,

$$\frac{a}{M} = \frac{a^{\text{phys}}}{GM^{\text{phys}}/c}, \quad \frac{R}{M} = \frac{R^{\text{phys}}}{GM^{\text{phys}}/c^2}. \quad (4.12)$$

To obtain the frequency in physical units [Hz], one uses the relation  $\kappa^{\text{phys}} = c\kappa$ . The geometrized frequencies are scaled by  $M^{-1}$ . Therefore, their numerical values must be multiplied by the factor

$$\frac{c}{2\pi M} = (3.231 \times 10^4 \text{Hz}) \left( \frac{M}{M_\odot} \right)^{-1} \quad (4.13)$$

to find the frequency in [Hz].

Figure 4.3 shows the dependence of the torus mass on time for different values  $\beta$  of the ratio between thermodynamical and magnetic pressure (plasma parameter),  $\beta \equiv P_g/P_m$ , for a torus with the radially increasing distribution of angular momentum,  $l(R) = l_{K,R=R_{\text{in}}}[1 + \epsilon(R - R_{\text{in}})]^q$  with  $q > 0$ ,  $0 < \epsilon \ll 1$ . This means that the reference level of the angular momentum density is set to  $l = \text{const} = l_K(R_{\text{in}})$ , motivated by the standard theory of thick accretion discs, where the constant value is a limit for stability. A radially growing profile then helps to stabilise the configuration.

Unless stated otherwise, we set  $q = 1$ ,  $\epsilon = 0.03/l(R_{\text{in}})$  for definiteness of examples in the simulations. At the inner edge of the torus the angular momentum equals the Keplerian value, and for higher radii it grows to super-Keplerian rotation, taking into account the specific shape of the relativistic Keplerian angular momentum (Abramowicz & Fragile 2013). Furthermore, following the von Zeipel theorem, in the vertical direction along the constant  $R = \text{const}$  surface within the torus, the angular momentum is defined by its value in the equatorial plane. The topology of these surfaces is cylindrical except for relativistic deviations that are important only at very small radii (Chakrabarti 1991).

From the graph we see that the amount of accreted mass is generally larger for smaller  $\beta$ . The plot also shows that the overall gradually decreasing trend is superposed with fast oscillations. After the initial drop of the torus mass (given by the magnitude of the initial perturbation,  $\delta M \simeq 0.01M_\bullet$ ) phases of enhanced accretion change with phases of diminished or zero accretion.

The oscillatory behaviour can be readily traced by the position of the torus centre, which we discuss below. It resembles the eigenfrequency modes that were proposed as a model for quasi-periodic oscillations in some X-ray binaries (Rezzolla et al. 2003; Montero & Zanotti 2012). A similar accretion history is found also for higher spin values, i.e., closer to extreme rotation, although we always assumed  $|a| < 1$  (we did not consider the possibility of a naked singularity, but see Stuchlík et al., 2011 for a recent discussion of such a possibility).

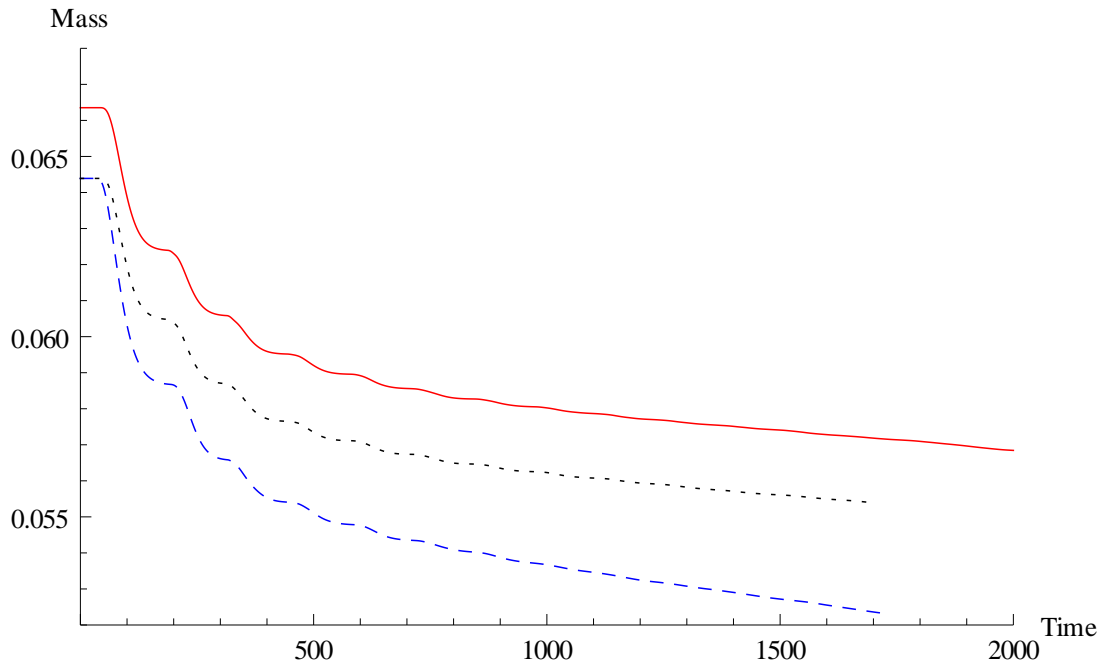
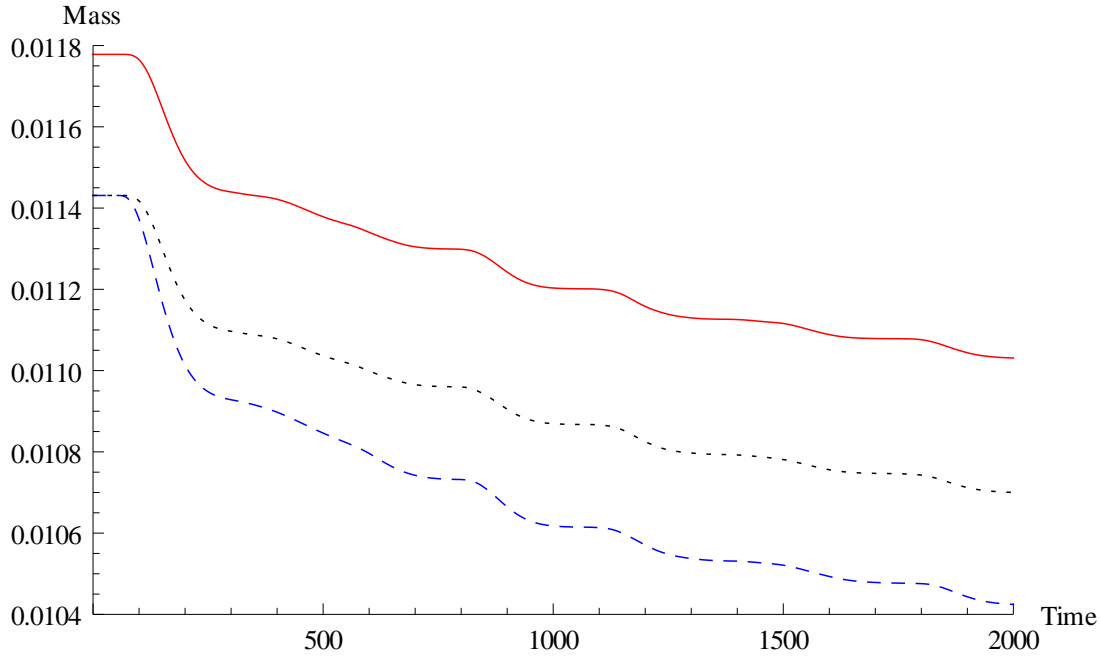


Figure 4.3: Torus mass,  $M_d(t)$ , relative to the black-hole mass as a function of time. The initial rapid accretion rate results in a drop of  $M_d$  that becomes partially stabilised during the subsequent evolution. Time is given in dimensionless units of  $GM_\bullet/c^3$ . The orbital period is close to its Keplerian value near the inner edge, i.e. about  $\Delta t(R) \simeq 100$  for the material near  $R = R_{\text{in}}$ . Top panel: The case of spin  $a = 0.1$  is shown for different values of magnetisation parameters  $\beta = 3$  (dashed),  $\beta = 80$  (dotted), and  $\beta \rightarrow \infty$  (i.e. a non-magnetised case; solid line). Bottom panel: as above, but for  $a = 0.9$ .

Figure 4.4 shows levels of mass density at different time moments. Four frames exhibit the changing torus structure during the accretion process. (a) The first frame corresponds to the initial equilibrium state; no mass overflow takes place and the mass distribution just fills the critical surface. (b) The next frame shows the perturbed configuration where the inner edge is pushed slightly outwards, which pushes the torus out of its initial steady-state. (c) The third frame captures the moment when the accretion drops, and finally, (d) in the last frame the mass transfer onto the black hole is completely interrupted, although the configuration is not exactly stable (accretion is then restored and the cycle continues). We carried out these simulations for a different angular momentum dependence on radius to reveal the above-mentioned effect of the  $l(R)$  profile.

Figure 4.5 is complementary to Fig. 4.3. In Figure 4.5 we compare several cases of different angular momentum profiles, as characterised by the slope  $q$ . One can see that the accretion rate is higher than in the previous example. This plot also confirms that for higher  $q$  the amount of accreted mass is diminished, in agreement with prior studies. In fact, for cases with indices  $q = 0.6$  and  $q = 0.8$  almost the whole torus is accreted. For  $q = 1.0$ , almost 96% of the initial torus mass is accreted, while for  $q = 1.1$  it becomes 88% of the initial mass. Generally, it is not possible to make a direct comparison of accretion properties amongst cases with different spin values because the properties of the spacetime are different. Therefore, marginally stable and marginally bounded orbits have different positions. Figure 4.6 compares the accretion rate for the case of  $a = 0.5$  and  $q = 1.0$  for different positions of the inner torus edge and, consequently, different positions of the torus centre  $r_c$ . It is evident that the amount of accreted mass increase with decreasing  $r_c$ . We also followed the oscillations of the point of maximal mass density inside the torus (the torus centre); it shows a behaviour consistent with the above-described evolution of the accreted mass.

Figure 4.7 studies the dependence of accretion rate by plotting the half-mass accretion time as a function of  $q$  and  $\beta$ . Furthermore, Figure 4.8 compares the magnetised vs. non-magnetised tori for the same spin ( $a = 0.3$ ). In the top panel we show the time dependence of the radial coordinate of the point with the highest mass density  $R = R_c$  (hence the highest pressure) of these two tori, and in the bottom panel the dependence of the highest mass density is captured as a function of time. In the limit of a non-magnetised slender torus ( $R_c \gg 1$ ) these oscillations correspond to the situation that has been treated previously by analytical methods (Blaes et al. 2006). Although the amplitude of  $R_c$  oscillations is quite small in these examples (because the oscillations were initiated by a weak perturbation and the torus centre is relatively far from the black hole), the outer layers of the torus are affected more significantly and can be accreted across the inner edge.

Let us note that in these simulations we neglected self-gravitation of the torus (Goodman & Narayan 1988; Karas et al. 2004). However, when the mass and angular momentum are accreted by the black hole, its parameters  $M$  and  $a$  are obviously changed. Hence, even for non-selfgravitating tori we need to update the parameters of Kerr space-time metric to achieve a consistent description. In our scheme we changed  $M$  and  $a$  at each time step, according to accreted mass and

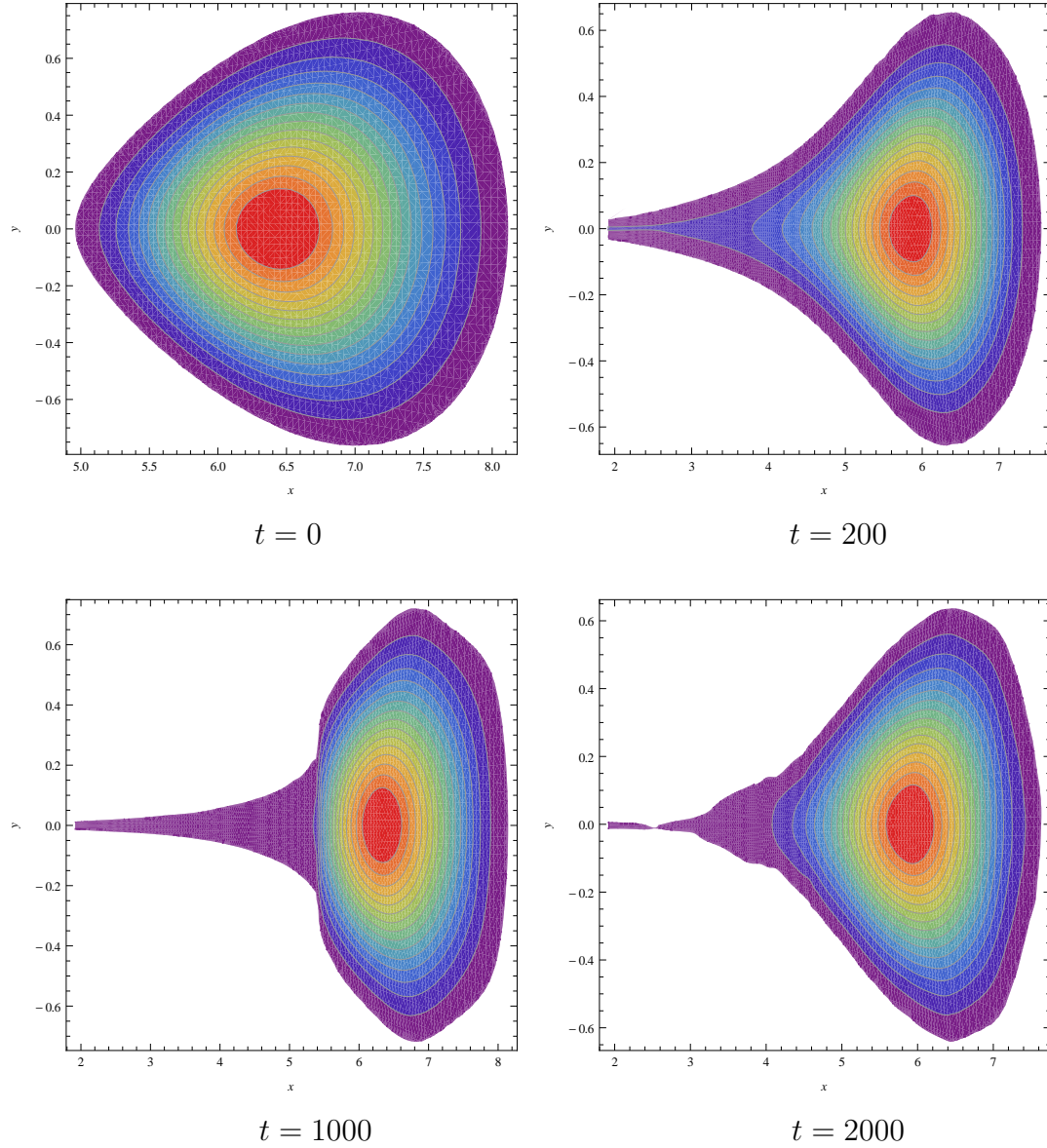


Figure 4.4: Time evolution of density levels in four snapshots of the poloidal section  $(x, y)$  across the accretion torus ( $x = 0$  is the symmetry axis). This example starts from the critical equilibrium configuration, which is perturbed at the initial moment of time. At this moment the Keplerian orbital time at the inner cusp,  $R = 5GM_{\bullet}/c^2$ , corresponds to  $T_{\text{Kep}} = 70GM_{\bullet}/c^3$ . Subsequently, accretion across the inner edge takes place onto the black hole (the outer horizon is at the left side of the panel). This process proceeds in an oscillatory manner, interchanging the phases of fast and diminishing accretion rate. The plasma magnetization parameter is set to  $\beta = 25$  (sub-equipartition pressure of the magnetic field), the black-hole spin  $a = 0.1$  (slow rotation of the black hole) in this example. The same colour scale as in Fig. 4.1. Geometrized units are used, where the length is scaled with respect to the gravitational radius,  $GM_{\bullet}/c^2$ , and time is scaled by  $GM_{\bullet}/c^3$ .

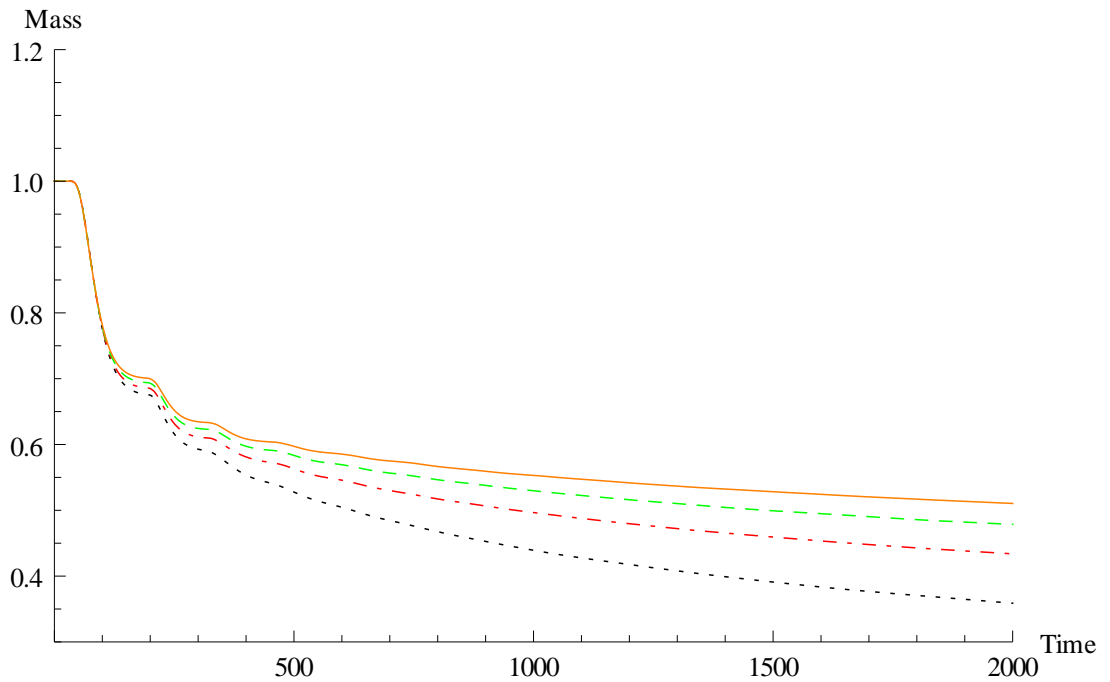
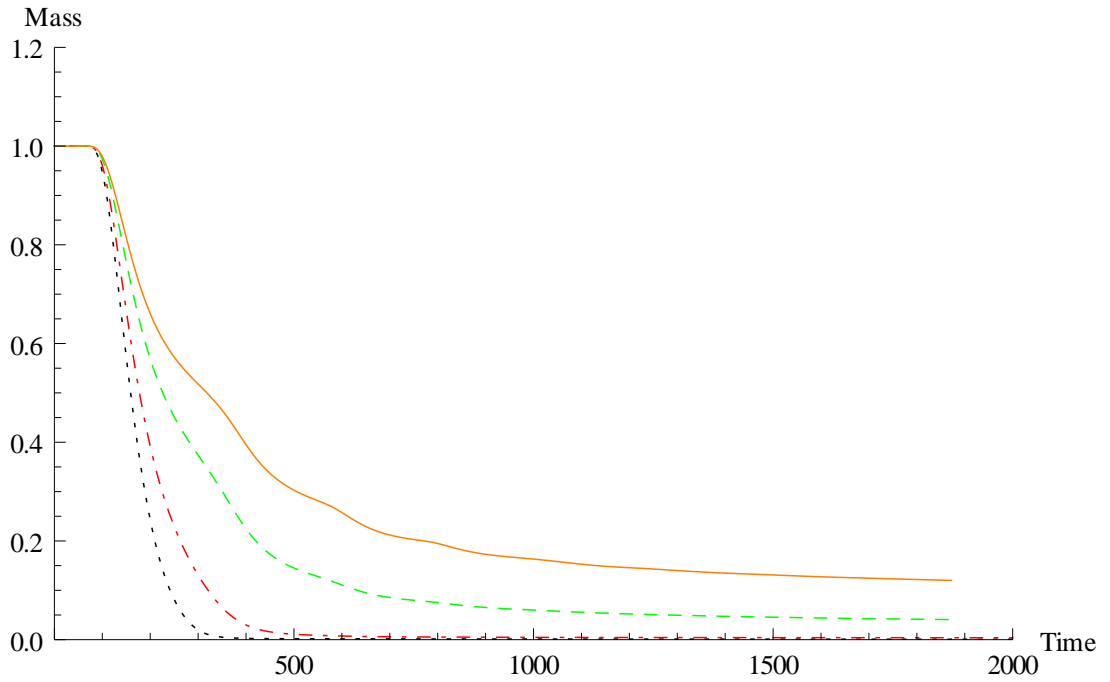


Figure 4.5:  $M_d(t)$ , mass of the torus, normalized with respect to the starting mass at the initial moment of the simulation,  $M_d(0)$ , is plotted as a function of time for different values of  $q = 0.6$  (dotted),  $0.8$  (dot-dashed),  $1.0$  (dashed),  $1.1$  (solid). Top panel:  $a = 0.3$ ; bottom panel:  $a = 0.9$ . For small  $q$  and small  $a$  the torus is unstable and its mass becomes quickly accreted onto the black hole, whereas higher values of the slope of the angular momentum distribution and fast spin of the black hole tend to stabilise the system against the initial perturbation (accretion stops at a certain moment).

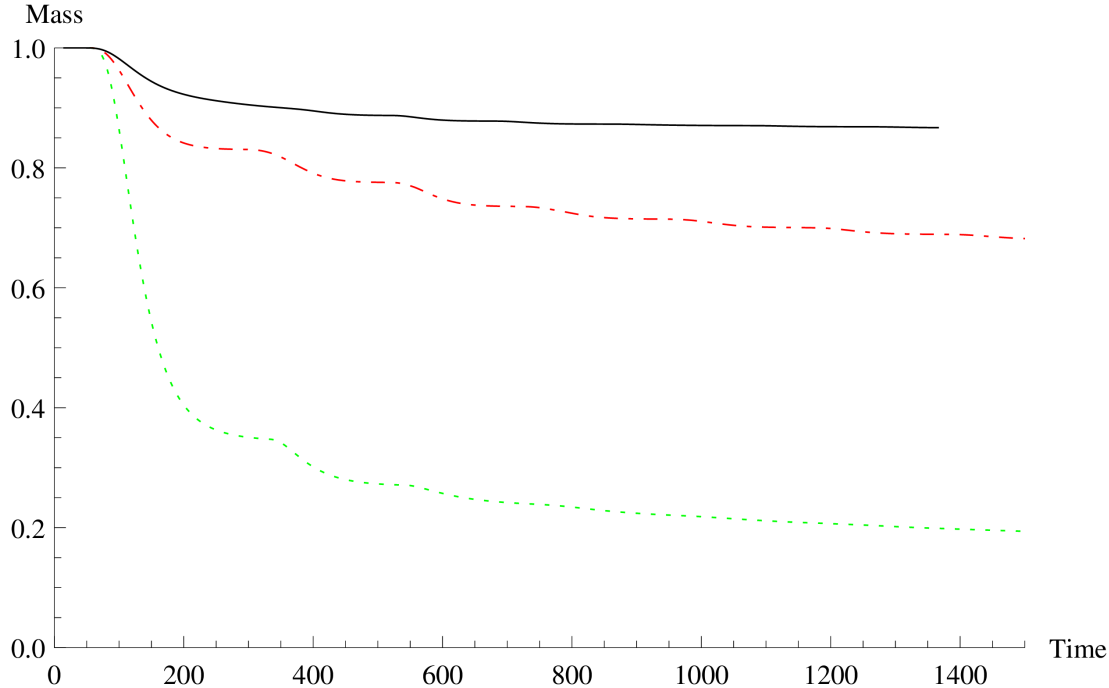


Figure 4.6:  $M_d(t)$ , mass of the torus, normalized with respect to the starting mass at the initial moment of the simulation,  $M_d(0)$ , is plotted as a function of time for different values of torus centre position:  $r_c = 5.45$  (dotted), 5.86 (dot-dashed), 6.13 (solid). The model parameters are:  $a = 0.5$ ,  $q = 1.0$ , marginally stable orbit is  $r_{ms} = 4.25$ . Coordinates are expressed in geometrized units ( $G = c = M_\bullet = 1$ ).

its angular momentum content. Then we can watch how this updating influences the accretion process, namely, oscillations of the torus centre, torus mass, and other characteristics. Figure 4.9 plots the dependence of the central mass density on time for a  $l(R) \propto R^q$  profile for the non-magnetised case. In an analogous way, we examined the role of different initial perturbations  $\delta M(t = 0)$ .

From these illustrations one can deduce that for a sufficiently steep slope  $q$  the torus becomes stabilised with respect to runaway accretion. The steeper  $q$ , the longer oscillation period. The (weak) initial perturbation does not significantly influence the oscillation period, only the oscillation amplitude is affected. Qualitatively identical conclusions are obtained for a slightly different value of the polytropic gas index. As mentioned above, the results presented here were computed for  $\gamma = 4/3$ ; we also computed the same set of plots for  $\gamma = 5/3$  with very similar results, while the model is more sensitive to relatively weak variations of  $q$ .

Finally, two additional plots reveal the changing parameters of the torus and the black hole in the course of accretion. Figure 4.10 compares the positions of the torus cusp and the torus centre as functions of the accreted mass, computed by integrating  $\Delta M_d(t) = \int_{t'=0}^t \delta M(t')$ , for different initial values of spin  $a = 0.3$ , 0.5, and 0.7.

The Kerr metric parameters  $M_\bullet$  and  $a$  are evolved during the accretion process (the initial spin values are given with the curves). The broken curve shows

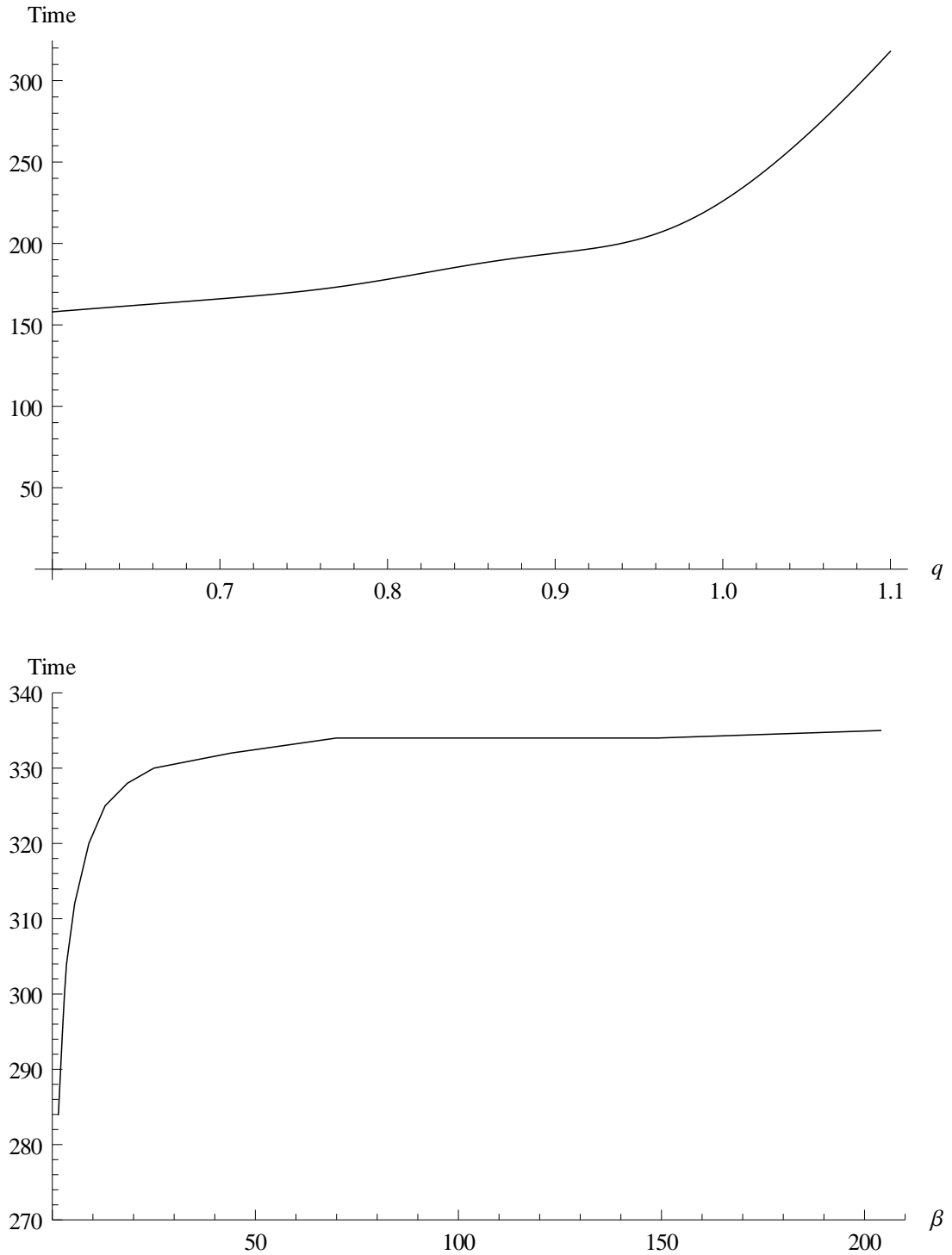


Figure 4.7: Top panel: time to accrete half of the total mass of the torus as a function of  $q$  (plasma parameter  $\beta = 3$ ). In agreement with the graph of  $M_d(t)$  in Fig. 4.5 we notice a higher rate of accretion (shorter accretion half-time) for lower values of  $q$ . Bottom panel: the dependence of accretion half-time on the plasma magnetization parameter  $\beta$  is shown; the power-law index of the angular momentum radial profile is set to a fixed value  $q = 1.1$ .

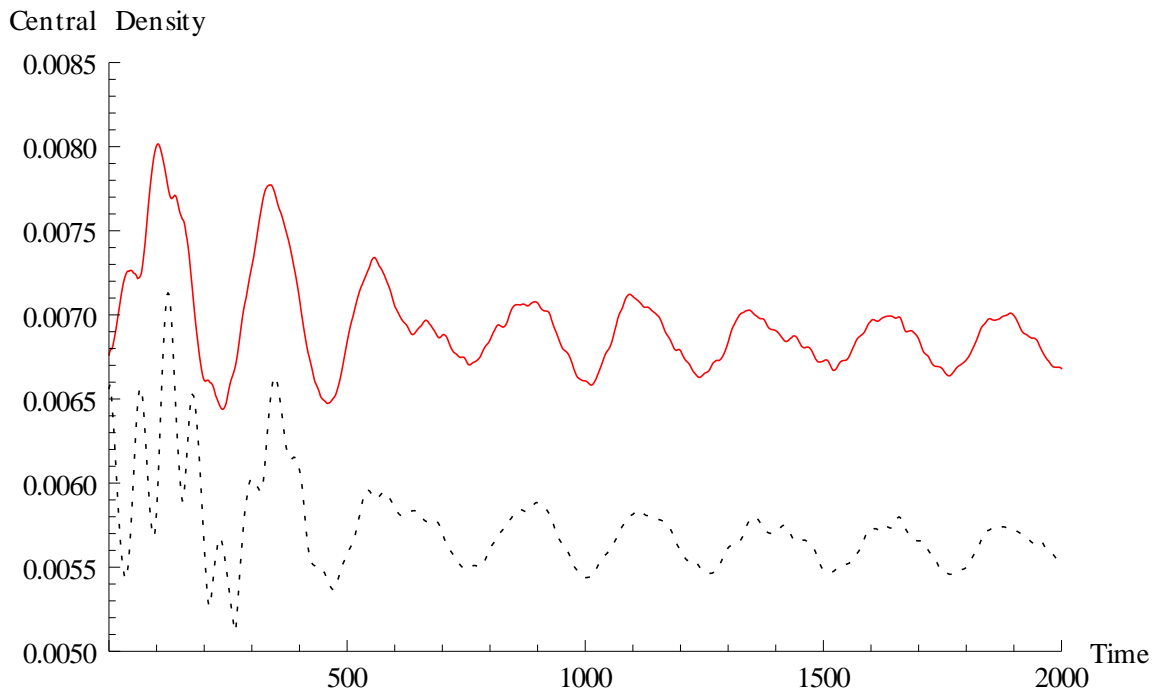
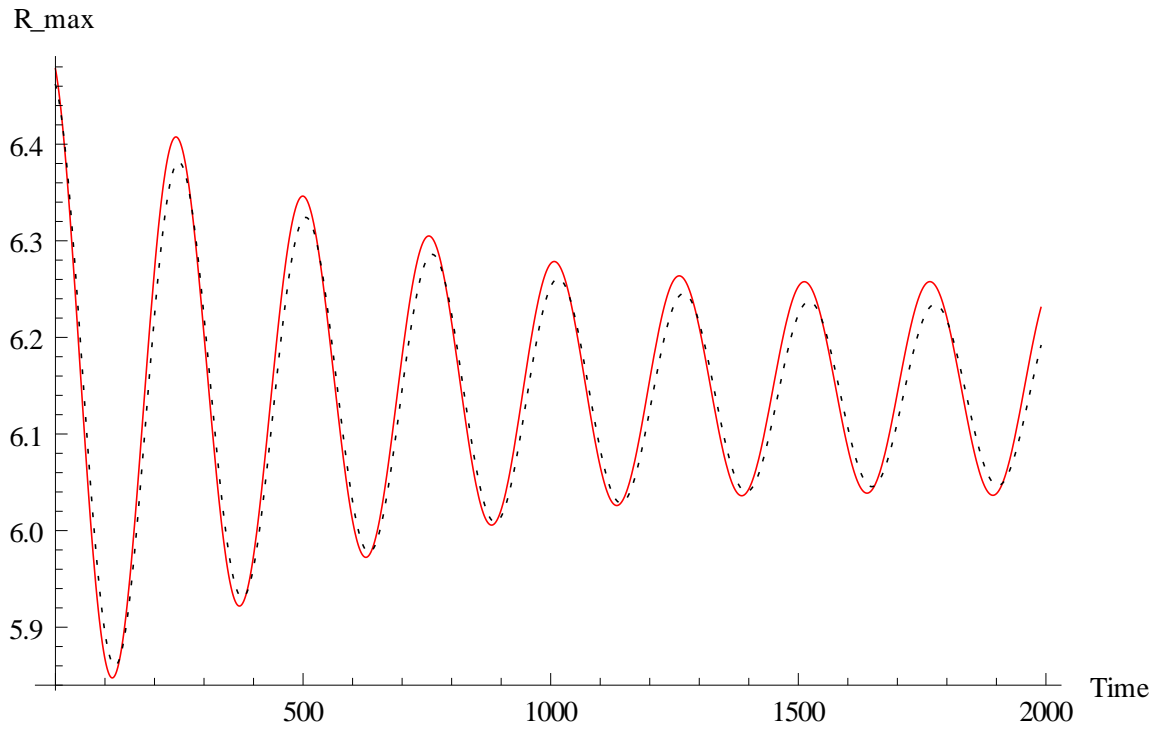


Figure 4.8: Oscillation of the torus centre  $R = R_c$  (top panel; radius is expressed in geometrized units  $GM_\bullet/c^2$  on the vertical axis), and of the central density  $\rho = \rho_c$  (bottom panel); density is relative to its peak value at the centre,  $\rho_c = \rho(R_c)$ . The solid line is for a non-magnetised case ( $\beta \gg 1$ ), the dotted line denotes the magnetised configuration ( $\beta = 3$ ).

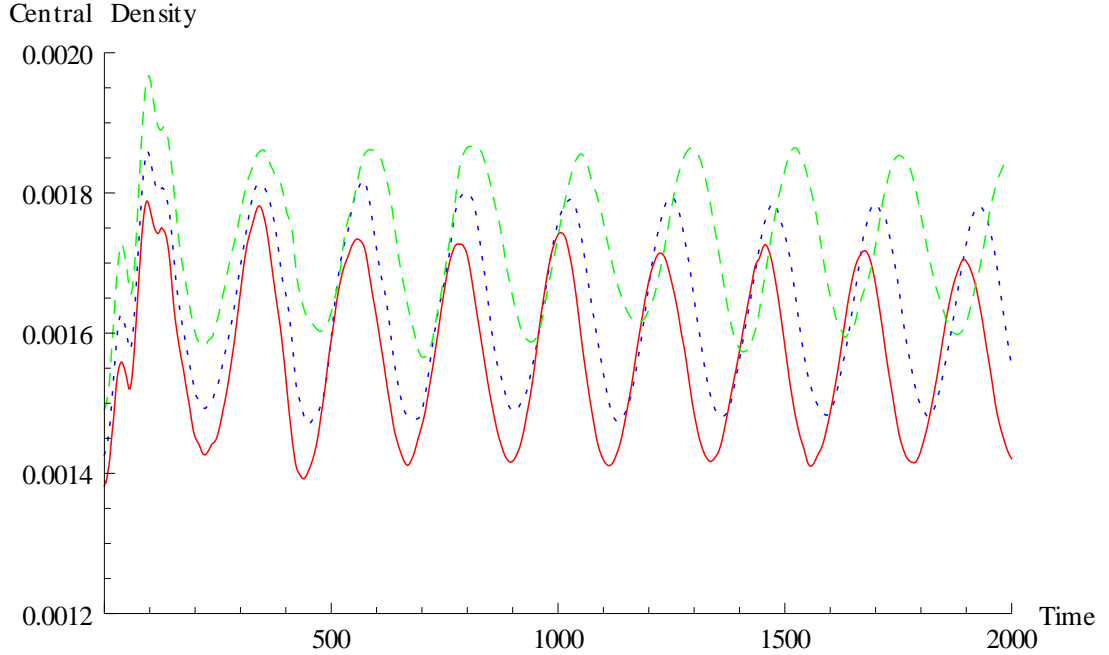


Figure 4.9: Central mass density for the fixed angular momentum  $a = 0.5$  of the black hole and varying index of the angular momentum profile of matter in the torus:  $q = 0.9, 1.0,$  and  $1.1$ . Vanishing magnetisation ( $\beta \gg 1$ ) in this example.

the dependence while the material with Keplerian angular momentum near the inner edge is accreted; the corresponding solid curve shows this dependence for a slightly lower angular momentum than the previous case at the inner edge: the angular-momentum values are for  $a = 0.3 \rightarrow l = 3.444$  (resp.  $3.15$ ), for  $a = 0.5 \rightarrow l = 3.263$  ( $2.936$ ); and for  $a = 0.7 \rightarrow l = 2.952$  ( $2.657$ ). The case of growing  $R_{\text{cusp}}(\Delta M_{\text{d}})$  generally corresponds to the receding inner edge, therefore to a shrinking volume of the torus, and so gradually increasing rate of mass accretion. Hence, the impact of increasing the black-hole mass is stronger than the effect of increasing the spin. In this case updating the metric parameters results in tori that tend to be more unstable. The mutual relation between the two radii, i.e.  $R_{\text{cusp}}$  vs.  $R_{\text{c}}$ , provides information about the size of the torus as it changes by losing material onto the black hole and moving in radius, while the black hole grows.

Naturally, the mean centre of the torus,  $R = R_{\text{c}}$ , moves along with the above-mentioned gradual evolution of the inner cusp,  $R = R_{\text{cusp}}$ , by the mass transfer from the torus onto the black hole. The torus centre obviously satisfies  $R_{\text{c}}(t) > R_{\text{cusp}}(t) > r_{+}(t)$  at each moment of the evolution. However, the exact mutual relation between these radii depends on details of the particular case, namely, the density and the angular momentum distribution within the torus. Therefore, both the mean  $R_{\text{c}}$  and the mean  $R_{\text{cusp}}$  can either approach the centre or recede towards a larger distance, depending on whether the torus shrinks and eventually becomes accreted onto the black hole (which is the case of runaway accretion) or if the partially accreted structure becomes stabilised against more mass transfer and stays away from the black hole. Naturally, the centre radius is influenced

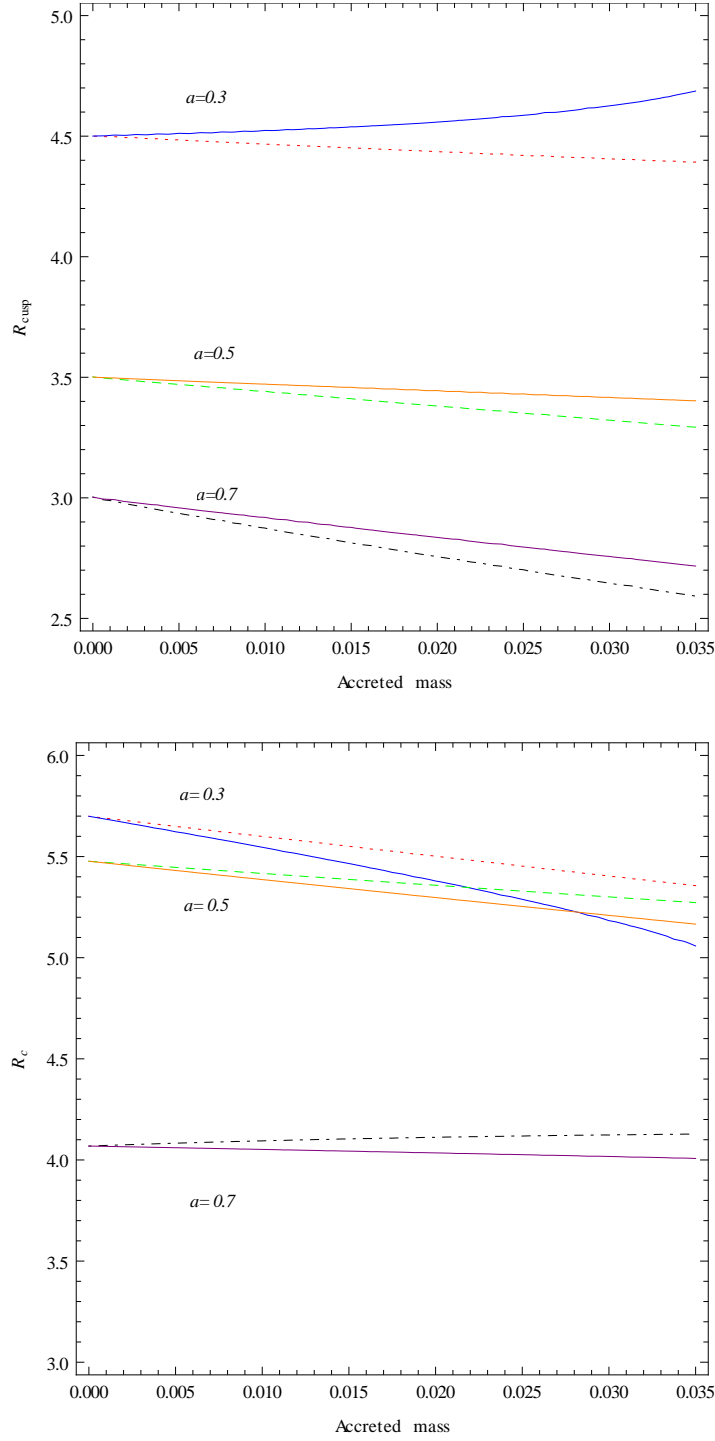


Figure 4.10: Evolution of the characteristic radii during the process of mass transfer from the accretion torus onto the black hole. Top panel: the mean radius  $R = R_{\text{cusp}}(t)$  of the cusp (i.e. the inner edge of the critical overflowing configuration) as a function of the mass accreted from the torus onto the black hole. Bottom panel: the dependence of the torus centre on the accreted mass for the same set of parameters (and the same notation of line types) as in the top panel.

also by the fact that the black hole itself evolves its mass and spin.

Figure 4.11 shows the oscillation frequency of the torus, as determined from a sequence of our numerical solutions with different position of the torus centre. The frequency varies gradually in this graph, along with the black-hole dimensionless spin  $a$ . Again, this change can be seen as a result of accretion of the material from the torus onto the black hole, which modifies the model parameters including the black-hole spin and the torus centre (as well as the corresponding torus mass,  $M_d$ , and other characteristics of the system, as explained above). This dependence allows us to unambiguously identify the relevant oscillation mode. We confirm a very precise agreement between the resulting curve in Fig. 4.11 and the theoretical formula for the radial epicyclic oscillation  $\kappa \equiv \kappa(M_\bullet, a)$ , see eq. (2.105) in Kato et al. (2008). The difference between the numerically determined value and the analytical formula for the radial epicyclic frequency is less than 1 per cent, and so the two dependencies are practically indistinguishable in the plot.

Naturally, to achieve a consistent solution, the parameters need to be evolved during the accretion process. Nevertheless, we checked that the above-mentioned point about the metric parameters does not influence the oscillation period of a globally stable configuration, i.e., until the perturbation itself remains weak.

In other words, while the position of the torus centre and the magnitude of central density differ at a level of several percent between different simulations, the agreement about the oscillation frequency is typically one order of magnitude better.

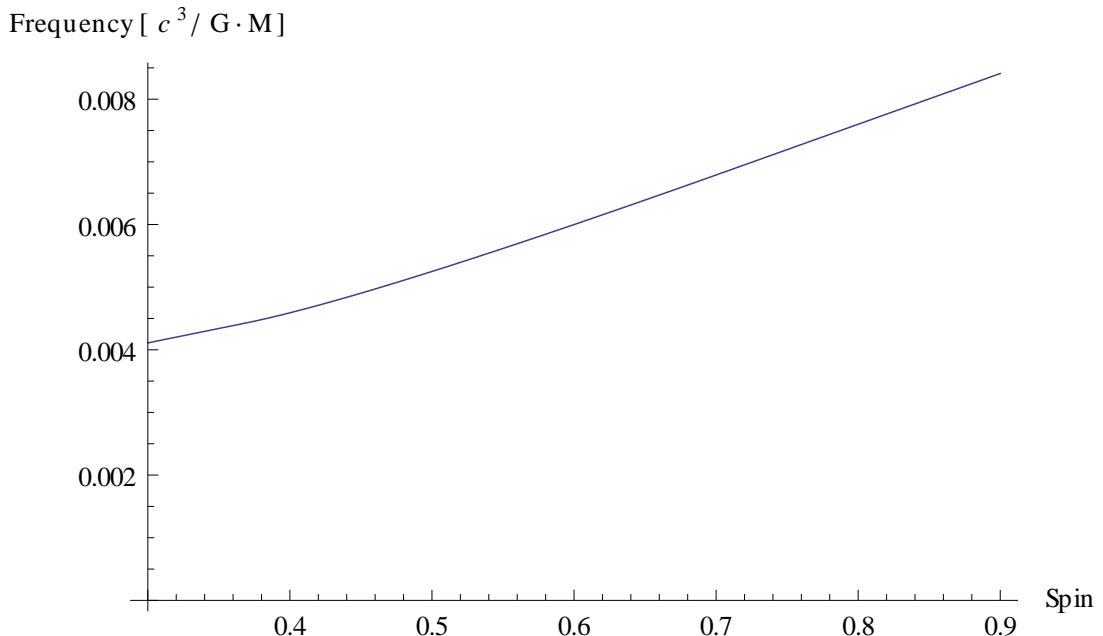


Figure 4.11: Oscillation frequency of the torus as a function of the black-hole dimensionless spin  $a$  from the numerical simulation (assuming  $0 \leq a \leq 1$ ,  $q = 1$ ). Different runs differ from each other by the radial position of the centre of the accretion torus, and therefore the oscillation frequency also varies. The functional dependence agrees with the radial epicyclic mode.

We recall a useful scheme (see Tab. 1 in Font & Daigne (2002)) that summarises a competing role of different agents that influence the stability of geometrically thick accretion tori near black holes. These are partly real physical effects (such as the angular momentum profile of the accreted material, rotation of the black hole, and self-gravity), and partly reflect the impact of approximations that are employed to describe the system (such as the Newtonian versus pseudo-Newtonian versus general-relativistic models). As mentioned above, radially growing angular momentum and fast rotation of the black hole tend to stabilise the system against the runaway instability, while self-gravity acts instead against stability. Therefore we can also include the magnetic field as another ingredient into the discussion of stability. However, as demonstrated also above in this chapter, with the increasing number of different factors and the interplay of mechanisms taken into account, the whole picture becomes more complicated than when one had restricted the discussion to the competition of just two or three degrees of freedom. In the end the outcome of the analysis can depend on detailed values of the parameters, e.g.  $q$  vs.  $a$ . Moreover, especially the magnetic field can develop different geometrical structures on vastly different scales, and so it may be difficult or impossible to characterise the role of magnetic field on the runaway stability in a simple way.

In our highly simplified scheme we showed that the effect of the toroidal test magnetic field (embedded in a prescribed manner into the polytropic fluid) just adds to the internal pressure of the fluid. Hence it basically enhances the instability in a similar way as any other contribution that can enhance the pressure above the equilibrium value.

## 4.2 A magnetised black hole torus disrupted by stellar fly-by

### 4.2.1 Introduction

In cores of galaxies, supermassive black holes (SMBHs) are immersed in a complex environment of gas and dust, stars, and stellar remnants in mutual interaction (Krolik 1999; Seth et al. 2008). Dust and diluted gas form a toroidal structure and an accretion disc extending from parsec-scales down to the innermost regions where the characteristic size is comparable to the gravitational radius  $R_g$  (Kato et al. 2008; Abramowicz & Fragile 2013).<sup>1</sup> In the following section we examine selected aspects of the problem following Hamerský & Karas (2015).

The presence of a geometrically and optically thick dusty torus is an essential component of the unification scheme of active galactic nuclei (Antonucci 1993; Urry & Padovani 1995; Peterson 1997). According to this scenario, the torus connects the inner regions (where temperature grows, dust evaporates, and an accretion disc/torus is made of plasma; Czerny & Hryniewicz (2011)) with outer environment of the galaxy ( $M$ - $\sigma$  relation proves that a link exists between the galactic bulge and the central black hole; Ferrarese & Merritt (2000), Gebhardt et al. (2000)).

Here we will concentrate on the inner region, where a standard accretion disc (Shakura & Sunyaev 1973) or a slim disc (Abramowicz et al. 1988) transport matter further down at a gradually growing temperature towards the black hole horizon. A gaseous accretion disc is evidenced in X-ray observations of active galactic nuclei (Fabian et al. 2004; Livio & Koekemoer 2011), where it acts as an agent through which the material is transported from the outskirts of the nucleus to the centre, and then partly down onto the black hole and partly it is returned back to the environment in the form of outflows via winds and collimated jets. Furthermore, star-disc collisions have been proposed as a viable mechanism for rapid metallicity enrichment of nuclear gas in some quasars (Artymowicz et al. 1993). Over the course of four decades, the accretion process has been explored in the context of supermassive as well as stellar-mass black holes (Begelman 1999; Karas & Šubr 2007).

The accretion disc/torus is not present in every galaxy, or the accretion flow may proceed only at a certain range of radii and then it is disrupted. In fact, the evidence for truncation of the inner accretion flow has been reported in several cases (Quataert et al. 1999; Svoboda et al. 2010). In low-luminosity galactic nuclei and, in particular, in the centre of the Milky Way, density of the interstellar matter is very low, the accretion rate is very small and the accretion disc does not exist in its standard form, at least during the under-luminous stage of the system. This is likely caused by a combination of lack of material near the black hole and the other circumstances that can disrupt the accretion flow. However, truncation of the inner torus may occur even in luminous AGN (Done et al. 2000; Lu et al.

---

<sup>1</sup> $R_g$  is proportional to the mass  $M_\bullet$  of the central black hole, typically  $R_g \equiv GM_\bullet/c^2 \doteq 1.48 \times 10^{11} M_6 \text{ cm}$  with  $M_6$  being the central mass of the supermassive black hole in units of  $10^6 M_\odot$  ( $c$  the speed of light in vacuum,  $G$  the gravitational constant).

2000; Matt et al. 2005). In this context it is also relevant to explore the fate of an initial stationary state of an equilibrium disc or a torus when it is disturbed out of its initial state beyond the level of small perturbations. While the role of embedded stars as an agent of the disruption has been discussed in great detail (Karas & Šubr 2001), here we consider a perturbation that is directed in a primarily vertical direction (perpendicular to the initially toroidal magnetic field), as for a star crossing the disc on an inclined trajectory.

Milky Way’s nucleus is currently inactive, however, a case has been made for vigorous accretion activity during its recent history (Sunyaev et al. 1993; Czerny et al. 2013). Since then, an accretion disc might have ceased because of declining supply of material, or it could have been disrupted by a passing stars from the nuclear star cluster (NSC).

NSCs are tentatively present in majority ( $\sim 75\%$ ) of all galaxies in the local Universe on length-scale (the half-light radius) of the order of a few parsecs (Carollo et al. 2002; Schödel et al. 2014). Several mechanisms operate in these dense stellar clusters, where they bring stars towards the SMBH. These include the long-term effect of dynamical friction and the gradual loss of orbital energy (Syer et al. 1991; Karas & Šubr 2001, 2007; Alexander & Hopman 2003), as well as direct collisions (Dale et al. 2009) and resonance mechanisms that set stars on highly eccentric ( $e \gtrsim 0.9$ ) plunging trajectories with pericentre  $R_p$  near the black hole (Alexander & Hopman 2003). The shortest relevant time-scale is the Keplerian period at the corresponding distance from SMBH,

$$T_K \simeq 0.3 \times 10^2 M_6 \left( \frac{R_p}{R_g} \right)^{3/2} (1 - e^2)^{-3/2} \text{ [s]}, \quad (4.14)$$

whereas the star–disc hydrodynamical collisions influence the trajectory on time-scales typically  $\sim 10^4$  times longer (Syer et al. 1991; Karas & Šubr 2001).

Repetitive interactions between stars and a SMBH accretion disc have been proposed as a promising mechanism to create clouds in AGN Broad-Line Regions (Zurek et al. 1994; Wang et al. 2012)<sup>2</sup>, and to sustain the magnetic field dynamo in inner regions of the accretion disc (Pariiev & Colgate 2007). Star–disc collisions can operate at sufficient frequency to explain power output of these sources. Stars transit across the disc slab, perturb the accretion flow and twist the large scale magnetic field to which the plasma is embedded. According to the latter scenario, as a star passes through the accretion disc it shocks and heats up its material, which then expands and lifts a fraction of the toroidal magnetic flux captured in an expanding plume.

Previously we discussed a model of the critical (Roche-lobe overflowing) inner accretion disc, which under certain conditions becomes runaway unstable (Abramowicz et al. 1998; Hamerský & Karas 2013). Part of its material becomes rapidly (‘runaway’) accreted onto the black hole and, depending on detailed circumstances and parameter values, the torus may either stabilize itself or it may disappear completely. The initial flow is naturally constrained by

---

<sup>2</sup>In this scenario the “clouds” acquire the shape of elongated “cometary” tails extending several scale heights above the disc plane.

the profile of angular momentum and the additional pressure due to magnetization (Hamerský & Karas 2013). The model agrees very well with the idea of large-scale magnetic fields that seem to be plausible in objects where accretion discs coexist with jets and outflows (Koide et al. 2000; Reynolds et al. 2006; Bisnovatyi-Kogan et al. 2013).

In this section we study a toy-model for a (magnetised) gaseous inner torus that is disturbed from its equilibrium state by an external influence. The suggested interpretation of the perturbation in terms of a stellar transit gives us a tentative scenario, where the material is pushed out in the vertical direction, nevertheless, a different origin of the perturbation is possible. As an initial state we assume the perfect-fluid torus embedded into a purely toroidal magnetic field near a rotating black hole (Komissarov 2006). While small perturbations lead to small oscillations at frequencies close to those expected from the linear perturbation theory (Okazaki et al. 1987; Abramowicz et al. 2006; Dai et al. 2010), large distortions (those beyond the validity of the standard linear perturbation analysis) may cause a partial or complete destruction of the torus. While weakly forced small perturbations have been studied in great detail (Lee et al. 2004; Pétri 2005; Bakala et al. 2012; Fu & Lai 2012), here we imagine that an abrupt excitation can occur when a stellar body hits the torus and pushes material along its inclined trajectory. The magnetic field structure is evolved from its initial organised form and contributes to the evolution of the fluid structure.

A number of other papers have discussed the role of long-term orbital evolution of NSC stars interacting with an embedded accretion disc/dusty torus, taking into account variety of secular effects that contribute to the gradual orbital decay: namely, dynamical interaction with other stars of a dense star cluster (Rauch 1995; Šubr et al. 2004; Just et al. 2012), oscillations of orbital eccentricity of stars induced by self-gravity of the torus or a stellar ring (Karas & Šubr 2007; Chang 2009), and losses by gravitational waves (Narayan 2000; Karas & Šubr 2001). Let us note that these results do not concentrate on the innermost regions of the accretion flow. Instead, they consider more distant areas (such as the Broad-Line Region) where most of the stars of a dense NSC are supposed to cross the accretion disc, while effects of General Relativity are not important. Nonetheless, a fraction of stars gradually sink to the central black hole, and so it is relevant to explore the induced perturbation imposed on the inner disc by such a star orbiting close to the SMBH, just above the tidal radius.

We think that it is interesting to realise that the mechanism of star–disc hydrodynamical interaction during transits of stars across the disc slab, originally envisioned as the origin of Broad-Line Region, can also deliver material of the inner disc into the corona very near to the black hole. This is relevant in the context of an ongoing debate about the evidence for highly compact coronae in some objects (Mosquera et al. 2013; Gardner & Done 2014).

We employ a two-dimensional scheme (HARM-2D code; Gammie et al. (2003)) which serves us as an exemplary test-bed and allows us to explore the parameter space. Depending on the model set-up, we examine qualitatively different cases when the perturbed material is either captured by the black hole or it becomes unbound and ejected from the system.

The section is organised as follows. We test the code by imposing a small density perturbation to the initial configuration and following its oscillatory evolution in time (sec. 4.2.2). We compare the numerically determined frequency of relevant modes with an analytical estimation. Then we explore the effect of a more significant disturbance to the initial state. We imagine that a certain amount of material is pushed out of the equatorial plane in a roughly vertical direction by a star transmitting the torus along a Keplerian orbit (sec. 4.2.2). We follow the expelled material, which falls towards the black hole or emerges away from the system. Finally, we discuss the results in sec. 5.

## 4.2.2 Triggered oscillations and outflows

### Oscillations of thick tori with various profile of angular momentum

Small oscillations about the equilibrium figure are generally stable and they become gradually attenuated until they trim to a new balance. On the other hand, disruption of a large magnitude applied near the torus centre can drive a significant amount of material out of equilibrium. This may result in a partial or complete deconstruction of the initial torus, which is beyond the applicability of the perturbation approach. Despite the fact that only a test-bed situation is considered in this work, we can observe transition from the oscillatory behaviour to the emergence of coupled outflow/accretion state where the initially imposed magnetic field influences the fraction of released vs. captured mass. Following such a large perturbation, a new equilibrium of the fluid does not have to be adjusted near the initial state, and also the large-scale magnetic field changes its structure.

Gravitational field is described by the Kerr metric line element (Kato et al. 2008)

$$ds^2 = -\Delta\Sigma\mathcal{A}^{-1}dt^2 + \mathcal{A}\Sigma^{-1}\sin^2\vartheta\left(d\phi - \omega_K dt\right)^2 + \Sigma\Delta^{-1}dr^2 + \Sigma d\vartheta^2, \quad (4.15)$$

where Boyer-Lindquist spheroidal coordinates  $(t, r, \vartheta, \phi)$  and geometrized units are used ( $c = G = 1$ ),  $\Delta = r^2 - 2M_\bullet r + a^2$ ,  $\Sigma = r^2 + a^2 \cos^2 \vartheta$ ,  $\mathcal{A} = (r^2 + a^2)^2 - \Delta a^2 \sin^2 \vartheta$ , and  $\omega_K = 2M_\bullet ar/\mathcal{A}$  are known functions of the spatial coordinates  $r$  and  $\vartheta$ . The specific rotational angular momentum (spin) is denoted  $a$ , i.e. the Kerr parameter; hereafter, to simplify notation, we will make  $a$  dimensionless by scaling with  $M_\bullet$  ( $|a| \leq 1$ ).

We adopt the description of tori as magnetised ideal fluid with the energy-momentum tensor (Anile 1989)

$$T^{\mu\nu} = (w + b^2) u^\mu u^\nu + (p_g + \frac{1}{2}b^2) g^{\mu\nu} - b^\mu b^\nu, \quad (4.16)$$

where  $w$  is the specific enthalpy,  $p_g$  is the gas pressure, and  $b^\mu$  is the projection of the magnetic field vector ( $b^2 = b^\mu b_\mu$ ). The evolution equations are obtained from the conservation of energy-momentum tensor. When setting all velocities zero

except of  $u^t$  and  $u^\varphi$ , one obtains the Euler equation for purely axially rotating fluid (Abramowicz et al. (1978); Abramowicz & Fragile (2013))

$$\ln |u_t| - \ln |u_{t_{\text{in}}}| + \int_0^{P_g} \frac{dp}{w} - \int_0^l \frac{\Omega dl}{1 - \Omega l} + \int_0^{\tilde{P}_m} \frac{d\tilde{p}_m}{\tilde{w}} = 0, \quad (4.17)$$

where  $u_t$  is the covariant component of the four-velocity (subscript ‘‘in’’ corresponds to the inner edge of the torus),  $\Omega = u^\varphi/u^t$  is the angular velocity and  $l = -u_\varphi/u_t$  is the angular momentum density,  $w = \rho + p_g + u$  is the specific enthalpy and  $\rho$ ,  $p_g$ ,  $u$  are rest mass density, gas pressure and internal energy density. Gas pressure  $p_g$  with magnetic pressure  $p_m = \frac{1}{2}b^2$  contribute to the total pressure  $p(\rho) = p_g + p_m$ . The tilde denotes rescaled quantities, i.e.,  $\tilde{w} \equiv \mathcal{L}w$ ,  $\tilde{p}_m \equiv \mathcal{L}p_m$ , where  $\mathcal{L}(r, \vartheta; a) \equiv g_{t\varphi}^2 - g_{tt} g_{\varphi\varphi}$  is a combination of metric terms (known functions of radius, latitude, and the spin parameter of the Kerr metric).

Assuming a polytropic equation of state, eq. (4.17) can be integrated to obtain the structure of equipotential surfaces of the equilibrium configuration. Komissarov (2006) found a solution of eq. (4.17) with the non-zero last term on the left hand side. The magnetic field is represented by four-vector  $b^\mu$  that obeys

$$b^\varphi = \pm \sqrt{\frac{2p_m}{\mathcal{A}}}, \quad b^t = lb^\varphi, \quad (4.18)$$

with  $\mathcal{A}(r, \vartheta) \equiv g_{\varphi\varphi} + 2lg_{t\varphi} + l^2g_{tt}$ .

The intrinsic eigenfrequencies of slender, non-self-gravitating, polytropic tori with an arbitrary profile of specific angular momentum, orbiting in an axisymmetric spacetime with the reflection symmetry, were derived for all the low-order modes (Blaes et al. 2006). Further down we will compare these frequencies against numerical results.

### Case of an initially small perturbation of density: subsequent oscillations of the torus

As an initial state for numerical experiments we adopt the stationary magnetised torus that has been perturbed by a small departure of the density distribution from the equilibrium solution. The latter is further enhanced by a star crossing the torus on an inclined trajectory repetitively at a suitable radius, as detailed below. For the initial state we assume that the purely toroidal magnetic field permeates the torus (Komissarov 2006). Obviously, a non-magnetised torus is a special case for  $\beta \rightarrow \infty$ . On the other hand, we do not exaggerate the magnetization over the equipartition between magnetic and pressure forces. We released tori with various thicknesses from the equilibrium configuration by imposing an initial density perturbation. To excite oscillations we prescribed a density profile inside the torus that was slightly different from the equilibrium solution in one quadrant (see figure 4.12). Cartesian coordinates  $x, y$  are derived from Boyer-Lindquist coordinates,  $x^2 + y^2 = R^2$  ( $x = R \sin \vartheta$ ,  $y = R \cos \vartheta$ ) and scaled with units of  $R_g$ .

As the initial perturbation we adopt a lower-density region (a horizontal stripe above the equatorial plane) which pushes the initial torus slightly out of equilibrium balance. The exact shape of the perturbed region is not essential for the

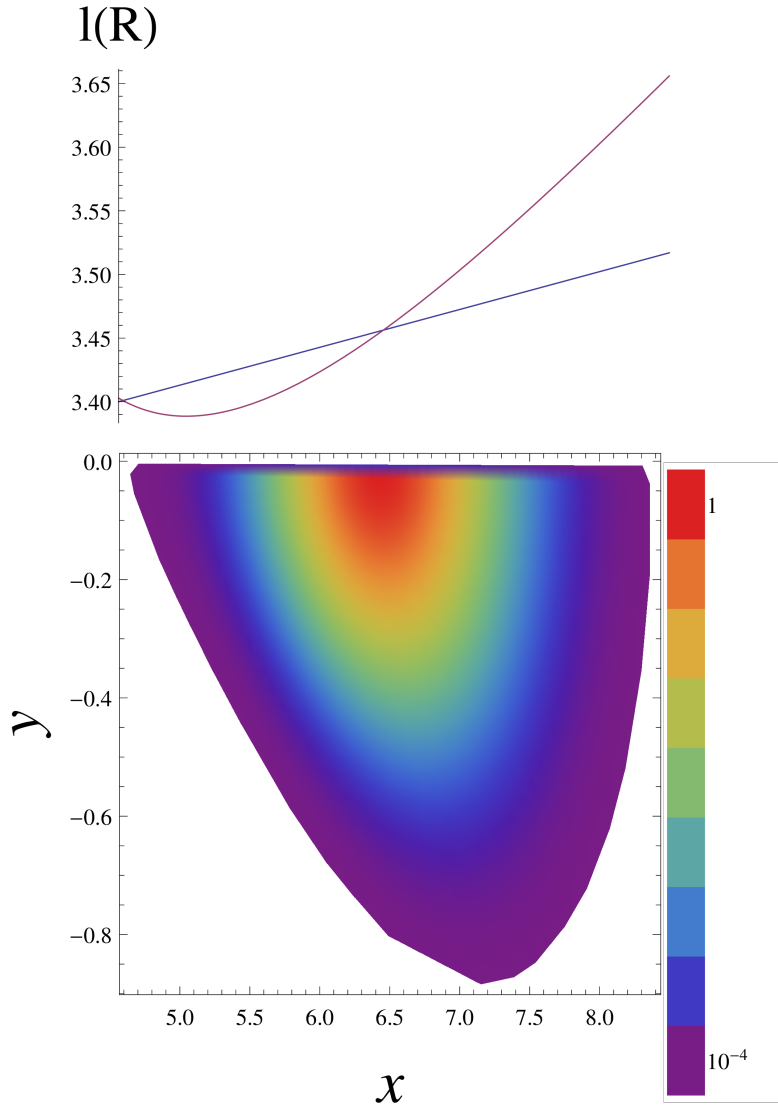


Figure 4.12: The starting set-up for the test example of density and specific angular momentum of a magnetised torus ( $\beta = 5.5$ ). Bottom: a poloidal  $(x, y)$  section across one quadrant of the torus. Two-dimensional distribution of density is shown below the equatorial plane. As an exemplary case of a small perturbation, a low density region above the equatorial plane was assumed to push the initial torus out of equilibrium. The colour bar sets the density scale (in arbitrary units, scaled to the peak value at the torus centre) in the  $(x, y)$  poloidal cross-section. The inner cusp is located at  $R = R_{\text{in}} \simeq 4.5R_g$ . Top: the profile of specific angular momentum  $l \equiv l(R)$  in the torus in the equatorial plane ( $y = 0, x = R$ ), where  $l(R) = l_K(R_{\text{in}}) + 0.03(R - R_{\text{in}})$  is a function of  $R$  only (blue line) and the profile of keplerian angular momentum  $l_K(R)$  in the equatorial plane (magenta). The intersections of the two profiles define the inner edge,  $R = R_{\text{in}}$ , and the centre of the torus,  $R = R_C$ , respectively.

mechanism to work, as long as it satisfies the conditions of being a small disturbance in terms of relative change of the density profile ( $\delta\rho(r, \theta)/\rho(r, \theta)$ ) order of a few percent. This gives rise to small oscillations accompanied by a limited movement of the torus centre and the central mass density. These oscillations have only a small amplitude and they die out after a moderate mass gets accreted. This is in agreement with a well-known observation that accretion can act to stabilise the torus (Abramowicz et al. 1998; Abramowicz & Fragile 2013). To check on the code evolving the perturbed configuration, we compared the oscillation frequency (of rest-mass density in the torus centre) which we determined numerically from the simulations with an analytical evaluation, based on Blaes et al. (2006). We considered all the modes for slender (non-magnetised) tori with constant specific angular momentum and selected the one that fits best the numerical result for the oscillation frequency. Even though the oscillations are excited in the vertical direction, the final motion is not the pure vertical epicyclic mode. The reason is that the inertial hydrodynamic modes of the torus contribute to the epicyclic modes and the final outcome is a combination of these interacting perturbations. The comparison with analytically derived modes for thin discs serves as a test of the impact of these inertial modes caused by the finite thickness of the torus. Theoretically, these inertial frequencies could cause that the torus would oscillate with frequency not allowed for thin discs or slender tori (Blaes et al. 2007; Horák 2008; Straub & Šrámková 2009). However, these can be investigated analytically only with approximation analysis (adequate for small perturbations), whereas here we explore large disturbances of the stationary torus that can even lead to destruction of the initial solution.

Figure 4.13 (top panel) compares these two frequencies as a function of geometrical thickness aspect ratio,  $h(R)/R$ . The plot demonstrates a remarkable agreement. There are two symbols for every thickness; blue square expresses the analytically computed frequency which was closest to our result obtained by numerical simulation, while the red dot denotes the numerical result. Within the selected range the effect of growing thickness does not cause discrepancy greater than 5%. Even the torus with  $h/R = 0.78$  oscillates at frequency that differs from its corresponding analytical mode by less than 1%.<sup>3</sup> Naturally, the torus exhibits a number of other oscillation modes, too. Here we selected the one that agrees best with the movement that we could reveal numerically from the fluctuating position of the torus centre. Let us note that the geometrized frequencies scale with  $1/M_\bullet$ . Therefore, their numerical values must be multiplied by the factor  $\frac{c}{2\pi M_\bullet} = 3.23 \times 10^4 \left(\frac{M_\bullet}{M_\odot}\right)^{-1}$  to find the value in physical units (Hz).

Figure 4.13 (bottom panel) examines the role of the specific angular momentum radial profile, given by the slope  $q$  of the power law  $l(R) \propto R^q$ , where  $0 \leq q \leq 1.3$ . For the same position of the inner edge, the tori with radially increasing profile  $l(R)$  extend radially to larger distance in comparison with the case of constant specific angular momentum. The largest torus in our examples

---

<sup>3</sup>The selected mode:  $x$ -parity  $-$ ,  $y$ -parity  $-$ ,  $j = 0$ ,  $k = 4$ ; cf. Tab. 4 in Blaes et al. (2006). The corresponding frequencies are equal to  $f_1 = 0.01974$  and  $f_2 = 0.01984$ , respectively (geometrized units, setting the speed of light and the gravitational constant equal to unity).

reaches six times farther in radius compared with the smallest one. The resulting deviations are relatively small in the given range of  $q$  and the difference between frequencies was less than 10%, as the plot demonstrates. Furthermore, there is no obvious trend of increasing those deviations with increasing slope  $q$ . So we conclude that analytical formulae for frequencies of slender tori with constant angular momentum are a good approximation for our purpose in this work.

Now, the effect of initial perturbation of density can be sustained and the oscillations enhanced by external triggering in the mentioned range of the torus. The magnitude of the perturbation is adequate to interpret it as a star passing across the torus, which mechanically pushes some material upward and supports the oscillations at the right (resonance) frequency. Effect of such recurrent disruptions depends very much on the interplay of parameters – internal parameters of the torus, size of the star, and the frequency of repetitive triggering versus the intrinsic frequency of the torus oscillation. An exemplary evolution is shown in figure 4.14, showing the density profiles at several subsequent time frames. The example reveals a disruptive effect which the repetitive triggering of the perturbation has on the torus. We explore this mechanism in the next section.

### **Case of repetitive triggering by stellar passages: ejection into corona and accretion onto SMBH**

A recurring perturbation can contribute to the initial disturbance and force the disc oscillation with a suitable periodicity. We already mentioned an example of a star crossing the torus on an inclined orbit (the twice per each revolution) and pushing some amount of material off the equatorial plane. The effect is naturally expected to be more pronounced when the orbital frequency of the star is commensurate with one of internal modes of torus oscillations. When such a relatively large repetitive disturbance is imposed on the initial torus, its further evolution cannot be treated by the formalism of small (linear) perturbation analysis. We can observe the mechanism with our toy model.

We set-up an example for this situation which we can then explore numerically. A range of directly affected radii is given by the cross-sectional area of the star. Hence, the relevant value depends on the size of star (radius  $R_*$ ) with respect to the gravitational radius ( $R_g$ ) of the central black hole. The black-hole spin  $a$  and the torus magnetization  $\beta$  enter the simulation as secondary parameters, along with the exact location of the torus inner edge ( $R=R_{\text{in}}$ ), the polytropic index ( $p \propto \rho^\gamma$ ) of the fluid, and the assumed angular momentum density profile,  $l(R) \propto R^q$ .

As an exemplary case we consider a torus at  $R_{\text{in}} = 4.5$  (i.e. near below the innermost stable circular orbit, ISCO, which also scales with the black hole mass), so the effects of General Relativity are prominently visible, including the typical inner cusp ( $R_{\text{ISCO}} = 4.98$  for the black hole spin  $a = 0.3$ ). The corresponding outer edge comes out at  $R_{\text{out}} = 8.42$ . Let us note that the radial extent of the torus depends on placing the inner edge  $R_{\text{in}}$  and the assumption about the specific angular momentum profile. As we assume tori with the relativistic cusp, the inner edge has to be set between the marginally stable and marginally bound orbit.

The same initial torus as in Fig. 4.12 (where only the part below the equatorial

plane was plotted) is evolved in the top-left panel in figure 4.15 in HARM-2D coordinates (Gammie et al. 2003). The set-up is defined in such a way that the entire left edge of the plot corresponds to the location of the outer horizon at  $r = R_+$ , the latitudinal angle  $\theta$  is a rescaled Boyer-Lindquist's  $\vartheta$ , and the  $x$ -axis is scaled logarithmically with radius. The thickness of the torus is defined by the aspect ratio  $\tan \vartheta = h(R)/R$ , where  $h$  is the vertical span of the torus. In this simulation we adopted the above-mentioned former case of a small radial span of the torus to achieve higher resolution of the numerics. Figure 4.15 shows the evolution of the resulting magnetised torus that underwent one large-scale perturbation by a passing stellar body (triggering of the intrinsic oscillation mode). The parameters are identical to those used previously in Fig. 4.14 (except for different spatial coordinates of the plot). In consequence of repetitive forcing the material becomes eventually expelled out of the torus. Fraction of its mass approaches the horizon, but the infall stalls by the centrifugal barrier (in cooperation with the magnetic field), which causes an increase of gas pressure and eventually helps to accelerate matter outward. As a result, only a part of mass accretes through the horizon while the rest is expelled out of the integration domain. In the magnetised case a larger fraction of mass is ejected from the torus and transported to the rotation axis. Figure 4.16 compares the dependence of mass comprised in the outflow along the axis (both magnetised and non-magnetised cases are considered). The outflow is defined by the material detached from the initial torus and streaming along the rotational axis toward the outer rim of the integration domain. In this example, spin of the black hole was  $a = 0.3$ , the inner edge of the torus  $R_{\text{in}} = 4.5$ , and the outer edge was situated at  $R_{\text{out}} = 8.4$  (in dimension-less geometrized units). Fig. 4.16 demonstrates that magnetised outflows typically comprise more mass and the peak occurs earlier in comparison with non-magnetised cases of otherwise identical parameters. When we focus on the centre of the outflowing blob (where the mass density reaches its maximum value) we find densities of the magnetised cases to be higher than the corresponding non-magnetised case. For example, the maximum mass density for the case with  $\beta = 5.5$  is higher by 20% in comparison with the non-magnetised case. At the same time, the magnetised case exhibits more material falling through the horizon, so we conclude that in our model the organised magnetic field helps to transport matter away from the disturbed torus. At time  $t = 50$  the torus contains about half of the initial torus mass in the non-magnetised case, and  $\simeq 30\%$  in the magnetised case ( $\beta = 4$ ). Figure 4.17 shows the dependence of maximal outflow velocity on magnetization parameter  $\beta$  for spin  $a = 0.3$ . Figures 4.18 and 4.19 show the same dependence but for spins  $a = 0.5$  and  $a = 0.9$ . For magnetic field whose pressure is comparable with thermodynamical pressure a steep growth of the outflow velocity occurs.

### Further details and examples of the torus disruption

Let us note that our integration procedure updates properly the mass and spin of the black hole, as they are transferred in the course of accretion. However, this aspect was more relevant in Hamerský & Karas (2013), where it contributed to the runaway instability of the critical torus. In the present work the model

parameters are set such that the total mass of the torus is very small, and so the change of black hole parameters does not play any important role in the process. Typical mass of the torus is 3% of the black hole mass.

Figure 4.20 shows the simulation where the helical magnetic field was adopted (vertical component  $B_y = 0.1 \cdot B_\varphi$ ) instead of the purely toroidal one. This plot demonstrates how the poloidal component of the magnetic field evolves. Magnetic field lines are largely chaotic and their geometry, which is developing with the mass movement, is subject to the redistribution of the torus material. In comparison with the purely toroidal magnetic field the outflow is formed earlier but the outflow velocities are very close to those obtained for the toroidal configuration. We conclude that the crucial parameter for the outflow velocities is the magnetization parameter  $\beta$ .

Let us note that it is not possible to compare directly the outflow velocities for different spin because the intrinsic properties of the spacetime of the relativistic model are different. Nevertheless, the feature of the increasing outflow velocity with the increasing magnetization is common for all models regardless of the spin value. The total amount of mass thrown out of the torus depends also on the radial span of repetitive disturbances.

The size of the torus which undergoes these perturbations determines the fraction of the initial torus that persists when perturbations are switched off. At late time (typically, tens of periods after the last perturbation at corresponding radius) oscillations are suppressed and the torus regains (almost) the equilibrium configuration with a very small accretion rate. Figure 4.21 shows the torus that has undergone six disturbances (the last one at  $t = 304$ ). From the Keplerian angular velocity  $\Omega_K^2 = GM_\bullet / (r^{\frac{3}{2}} + aM_\bullet^{\frac{1}{2}})^2$  we get the Keplerian period  $T_K = 105$  (in geometrized units; for SMBH mass  $M_\bullet = 10^6 M_\odot$  the corresponding value is 3258 sec in physical units). The period of density oscillations is approximately half of  $T_y \simeq \frac{1}{2}T_K \doteq 53$ .

Let us note that in our examples we set the torus mass (relative to the central black hole) to a small value  $m \equiv M_d/M_\bullet = 0.03$ , so that the torus gravity does not play any significant role. In this set-up the average mass density within the torus is  $\rho_D \simeq 6 \cdot 10^{-5}$ , and the characteristic density with the volume encompassed by the black hole horizon radius (computed as the black hole mass divided by  $\frac{4}{3}\pi R_H^3$ ) is  $\rho_\bullet(R_H) = 3 \cdot 10^{-2}$ . Unless stated otherwise, we assume  $M_\bullet = 1$ . If the mass density of the torus  $\rho_D(R)$  is comparable to  $\rho_\bullet(R) = 1/(\frac{4}{3}\pi R^3)$  the gravity of the torus starts to play a role. The equality sets in at  $R \sim 7$ . Moreover, assuming a supermassive black hole ( $M_\bullet = 10^6 M_\odot$ ) as the central object, the radial span of the torus comes out comparable with the size of a main-sequence star (it is approximately equal to  $4R_\odot$ ). This scenario is quite unlikely for a giant star because the Roche limit  $R_L = 1.26R_H(\rho_\bullet/\rho_\star)^{1/3} \simeq 60$  and so the star would disintegrate by tidal effects. On the other hand, for  $R_{\text{in}} = 3.4$  and  $q = 1$  the outer edge recedes to  $R_{\text{out}} \simeq 199$ .

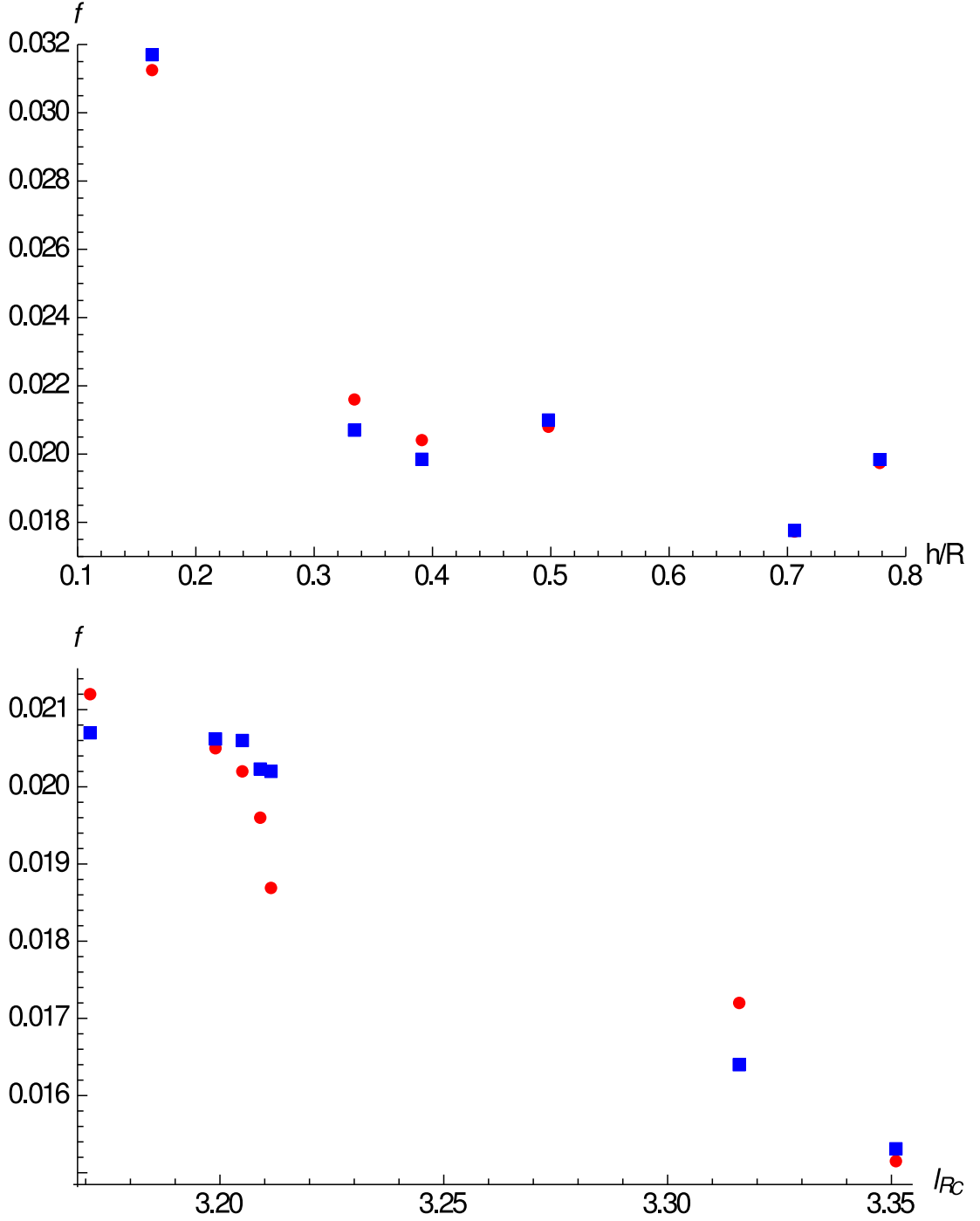


Figure 4.13: A test of determination of the oscillation frequency based on central density fluctuations of the disturbed torus following a small perturbation. Two graphs compare the oscillation frequency computed analytically from the linearized description (blue squares- Blaes et al. (2006)) vs. the corresponding oscillation mode obtained numerically from the simulation (red dots- this work). Top panel: case of tori with different geometrical thickness,  $h/R$ . Bottom panel: the same as a function of specific angular momentum at the torus centre  $l_{RC} \equiv l(R_C)$ . Time is given in dimensionless units of  $GM_{\bullet}/c^3$ , spatial coordinates in  $GM_{\bullet}/c^2$ .

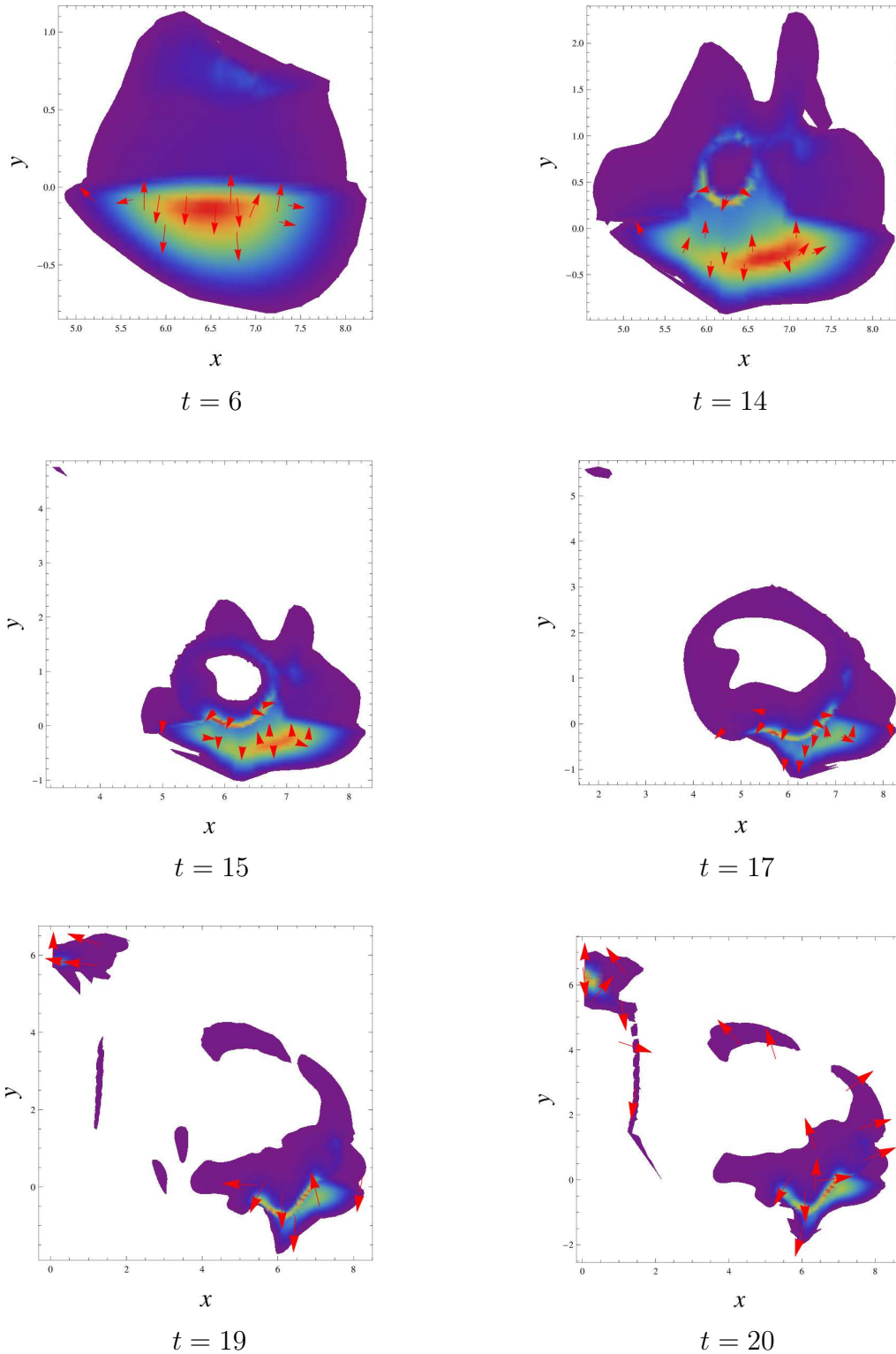


Figure 4.14: Six snapshots of density profiles taken at different moments of time following a large perturbation, with corresponding velocity vectors (arrows) overplotted in the poloidal  $(x, y)$  plane. The case of  $\beta = 5.5$  is shown. The same colour scale has been used as in the previous figure (white outside the matter distribution).

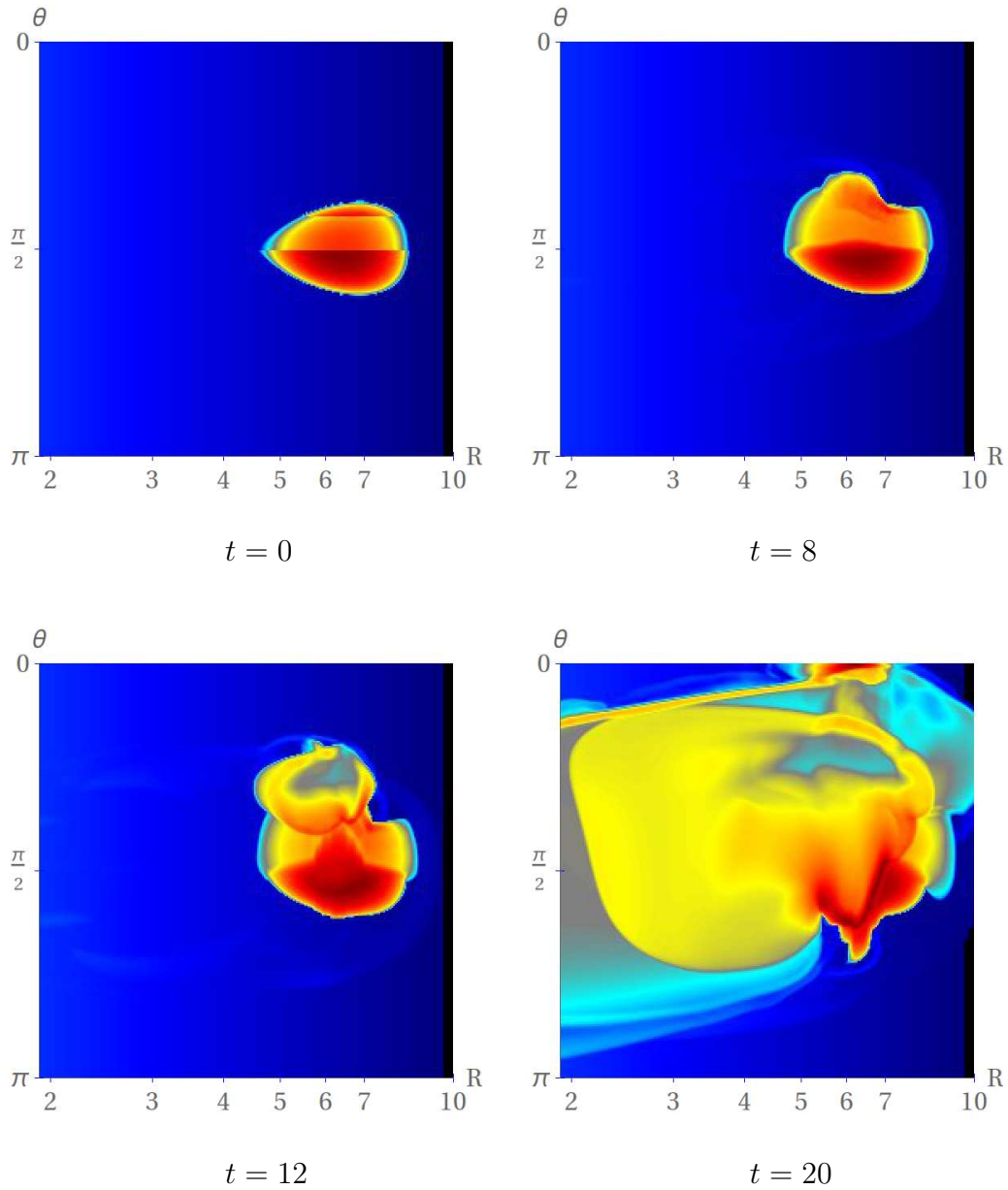


Figure 4.15: Evolution of a magnetised axisymmetric torus (HARM-2D coordinates, the horizon radius is located along the left axis). Plots show the distribution of rest mass density at  $t = 0, 8, 12, 20$ . Colours are scaled with respect to the maximum value of density (red) in each panel separately. The initial density perturbation (a low mass density stripe above the equatorial plane) gave rise to the vertical oscillation. Subsequent large-scale perturbation by a passing star accelerated the material in the vertical direction which, consequently, increased the oscillation amplitude. The inner edge of the torus (the inner cusp) is at  $R_{\text{in}} = 4.5$ , the outer edge at  $R_{\text{out}} = 8.42$  and the profile of specific angular momentum is:  $l(R) = l_{\text{K}}(R_{\text{in}}) + 0.03(R - R_{\text{in}})$ . The perturbation was initiated in the vertical direction between  $r = 5.8$  and  $r = 6.9$ .

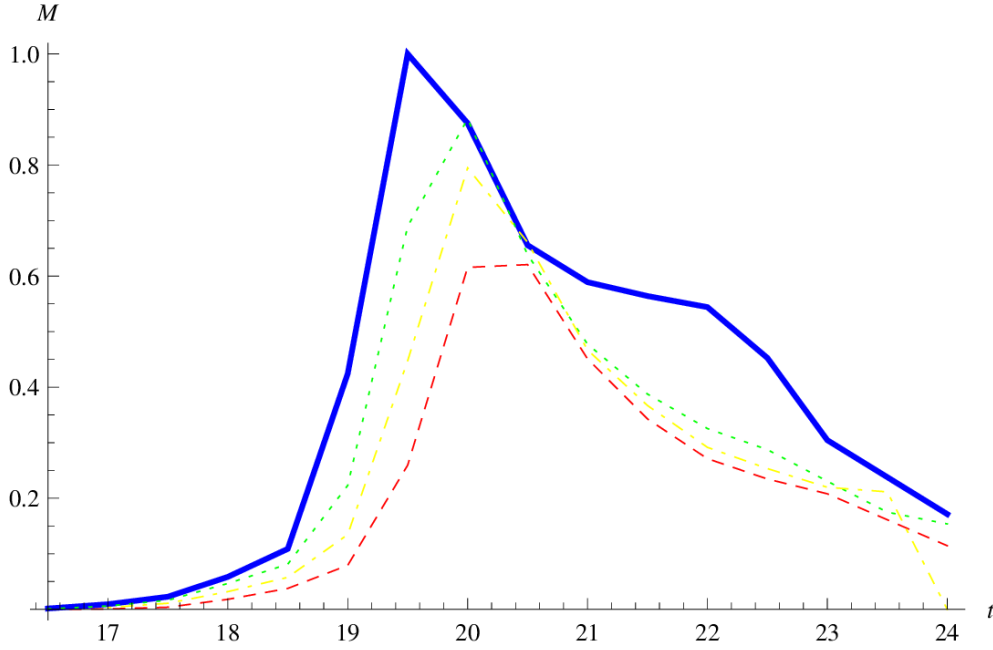


Figure 4.16: Mass fraction (normalized to the maximal value) ejected in an outflow out of the integration domain as function of time:  $\beta = 3.1$  (blue solid line),  $\beta = 4.5$  (green dotted),  $\beta = 7$  (yellow dot-dashed), and the non-magnetised case (red dashed line).

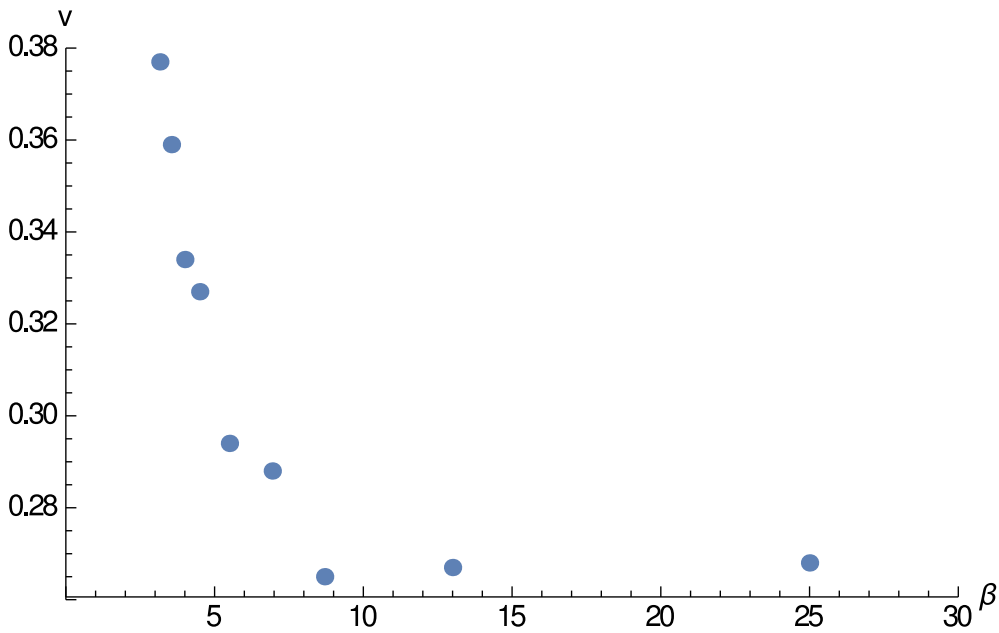


Figure 4.17: Maximal value of outflow velocity  $v$  (vertical component in cartesian coordinates, expressed in units of  $c$ ) as a function of magnetization parameter  $\beta$ . The imposed magnetic field was initially purely toroidal ( $\beta > 1$ , sub-equipartition magnetic intensity). The outflow initiation is triggered by the stellar passage but the terminal velocity depends mainly on the magnetization. The black hole spin is  $a = 0.3$ .

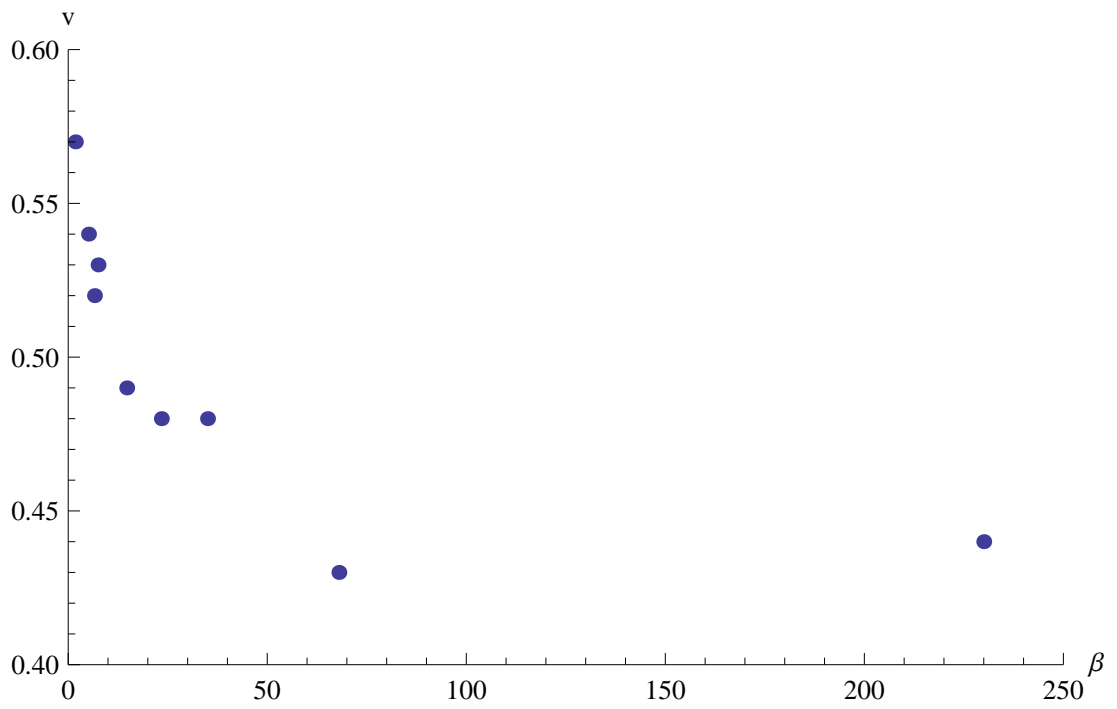


Figure 4.18: The same dependence as in figure 4.17 but for black hole spin  $a = 0.5$ .

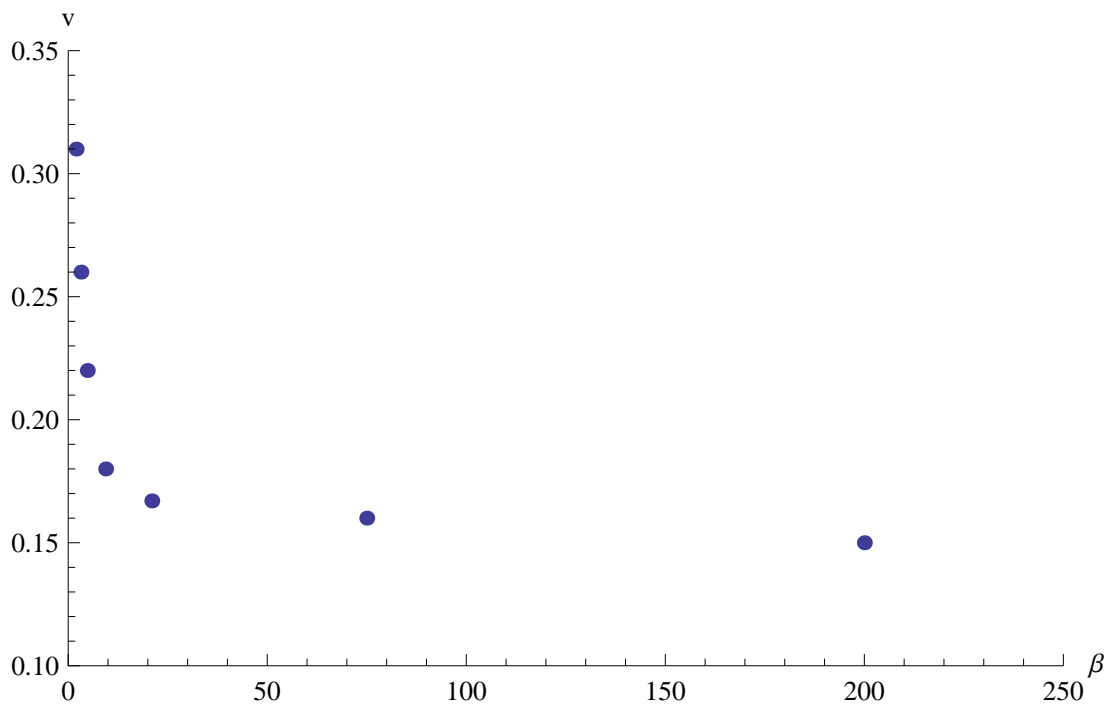


Figure 4.19: The same dependence as in figure 4.17 but for black hole spin  $a = 0.9$ .

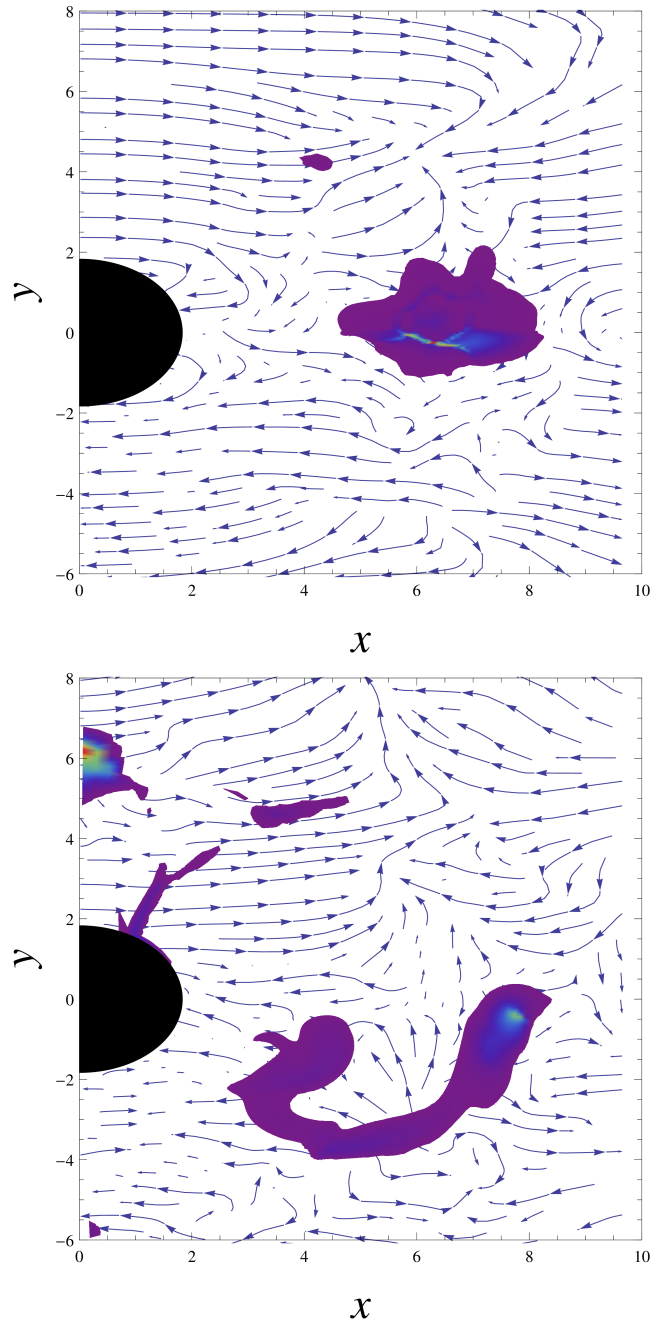


Figure 4.20: Density distribution supplemented by the magnetic field lines at  $t = 14$  (top) and  $t = 20$  (bottom), plotted in the projection onto the poloidal  $(x, y)$  section. The poloidal magnetic component develops in the course of accretion from the originally helical configuration ( $B_y = 0.1 \cdot B_\varphi$ ) and the poloidal motion of the matter due to the torus perturbation. At later time a blob detaches from the initial configuration and it reaches the rotation axis, where a part of it becomes accreted whereas the rest is ejected outwardly. The black circle denotes location of the black-hole horizon.

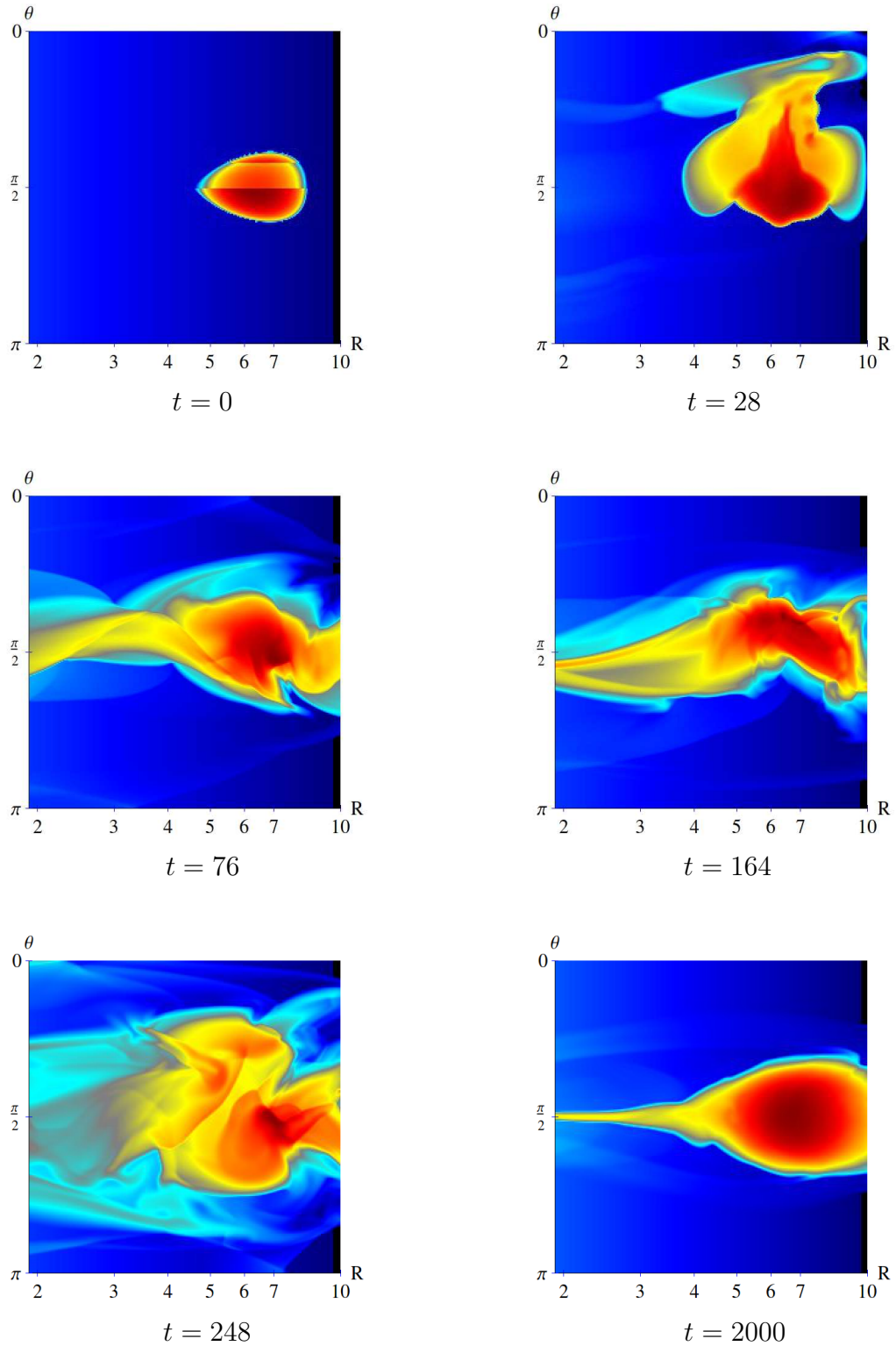


Figure 4.21: Long-time evolution of magnetised torus and the final restoration of the torus (the same set-up as in Fig. 4.15). Different panels show the distribution of rest-mass density at numerical time  $t = 0, 28, 76, 164, 248, 2000$ . A new stationary configuration eventually emerges in the last panel, when the external forcing ceases and the disturbed material is either accreted onto the black hole or ejected out of the system. The final mass of the torus is  $\simeq 30\%$  of the initial value.



## 5. Discussion

Within the framework of an axially symmetric magnetized fluid torus model we have extended the previous results on the onset of runaway instability of relativistic configurations near a rotating black hole. We concentrated on systems with radially increasing angular momentum density that are threaded by a purely toroidal magnetic field. We neglected self-gravity of the gaseous material (the mass of the torus was set to be at most several percent of the black-hole mass), nevertheless, we allowed for a gradual change of the Kerr metric mass and spin parameters by accretion over the inner edge. The angular momentum distribution within the torus was also allowed to evolve, starting from the initial power-law profile. The mass transfer influences the location of the cusp of the critical configuration, which can lead to the runaway instability.

If the profile of the angular momentum increases sufficiently fast with radius (typically, for  $q \gtrsim 0.8$ ), the initial perturbation becomes stabilised by accretion of a small amount of material, whereas for small  $q$  the instability causes rapid accretion of the torus. The intensity of the threaded magnetic field influences the process of stabilisation or destruction of the torus because, within the framework of the adopted model, the magnetic pressure adds directly to the gas pressure (plasma parameter  $\beta \gtrsim 1$ ).

The process of accretion is not perfectly monotonic, instead, there are changing phases of enhanced accretion rate and phases where the mass of torus remains almost constant. The overall gradual decrease of the torus mass is superposed with oscillations that can be seen by following the central density variations on the dynamical time-scale and the position of the centre of the torus. The oscillation amplitude is sensitive to the initial perturbation, but the frequency is not, namely, a small change of the metric coefficients does not affect the oscillation frequency.

The toroidal magnetic field plays a more important role in the early phases of the accretion process until the perturbed configuration finds a new equilibrium or disappears because of the runaway instability. If the oscillations become stabilised with time, no significant differences occur from the corresponding non-magnetized case, even when  $\beta$  is near unity (equipartition) and the accreted fraction of the torus material is significant.

Although our set-up of the model and the choice of parameters are tuned to the scenario of tori breakup near SMBH, a similar approach was adopted for gamma ray bursts from magnetised tori accreting onto a stellar-mass black hole (Barkov & Komissarov 2008; Janiuk et al. 2013). It was further proposed (Janiuk et al. 2014) that also black-hole binaries can exhibit periods of significant outflows that are supported magnetically and directed vertically from the inner region. Large-scale azimuthal magnetic fields are also discussed in the context of planet migration through an accretion disc (Bans et al. 2015) and, furthermore, magnetically driven outflows are modelled for the evolution of 3D tori near Kerr black holes (De Villiers et al. 2003; Wielgus et al. 2015). Purely toroidal magnetic field is the prominent and probably the only relevant analytical solution

for a stationary magnetised torus consisting of perfectly conducting plasma. The toroidal magnetic structures have been discussed widely in literature. The observations of polarization from the Galactic centre (Novak et al. 2003) suggest the evidence of large-scale toroidal magnetic fields, although the observations of non-thermal filaments call for some caution and the presence of ordered field is still under debate (LaRosa et al. 2004). We start with the toy model where the magnetic field is initially purely toroidal, without any poloidal component. Studying the onset of turbulent state evolved from this stationary solution is a feasible experiment serving to explore how the parameters of the system support or suppress this transition. The effect of different magnetic field geometry has been studied by various authors (Beckwith et al. 2008; McKinney & Blandford 2009). Purely toroidal magnetic configurations evolve more slowly than those with an initial poloidal component (for review see Yuan & Narayan 2014).

We explored a toy model where star–disc collisions disrupt the inner torus. Even a small perturbation can feed material from the torus into the corona when repeated at a suitable frequency commensurate with one of internal modes of the torus oscillation.

We extended our previous results on the properties of relativistic accretion tori that fill the cuspy lobe or are close to this critical configuration. We selected a particular case of azimuthally weakly magnetised geometrically thick tori that can oscillate with frequencies close to those derived in an analytical approximation. A radially increasing profile of angular momentum density, defined by the slope parameter  $q < 1.3$ , affects the oscillation frequency only moderately and the resulting frequencies differ from those analytically computed not more than by  $\sim 10\%$ .

The initial oscillations are caused by an under-density stripe in one part of the torus. Then they are assisted, at a suitable frequency, by repetitive triggering that acts at a suitable range of radius. The material overflows from the equipotential surface and allows the mass of an inviscid torus to be accreted. When approaching the marginally stable orbit the accretion process is decelerated by centrifugal forces and material is accelerated outward by gas pressure. The presence of magnetic field supports this acceleration. The vertical component of outflow velocity increases with stronger magnetization (smaller  $\beta$ ). The initial purely toroidal magnetic field remains toroidal and the initial helical field becomes chaotic in a short time. Configurations with the initial helical magnetic field evolve faster in comparison with the purely toroidal configurations and the amount of mass in outflows and their velocities are proportional to the magnetization parameter  $\beta$ . The presence of the poloidal component of the field does not influence the outflow velocities significantly, thus, the crucial parameter of the magnetic field is the ratio of its pressure to the thermodynamical pressure  $\beta$ .

Finally, let us note that the variety of MHD mechanisms can plausibly lead to vertical outflows that may either stabilise the torus oscillation or grow towards its destruction. Our 2D approach is an obvious simplification which can capture some aspects of accretion averaged over azimuth while neglecting non-axisymmetric features, which should be included (work in progress). Other prior works have considered various distributions of the initial angular momentum of the gas and

topology of the magnetic field because these can be relevant for the problem of trapping of large-scale magnetic flux in the plunging region (Reynolds et al. 2006). The main focus of our investigation concerned the fate of a mechanically (collisionally) disturbed torus, where an initially moderate oscillations either settle down or they may grow to a significant loss of the material from the torus.

The procedure of updating mass and angular momentum of the black hole in the course of accretion will be relevant when the star passes below the tidal radius and becomes disrupted (work in progress). Then the amount of accreted material may increase significantly to evolve also  $M_{\bullet}$  and  $a$  parameters.



## 6. Conclusions

In this Thesis we studied oscillation and accretion properties of geometrically thick accretion tori in strong gravity regime. We studied influence of magnetic field, specific angular momentum profile and different perturbations on the time evolution of the torus. For the numerical simulations we used HARM-2D (Gammie et al. 2003). Theoretical and numerical schemes of our simulations were presented in Chapter 3.

Results of this Thesis are presented in Chapter 3. In Section 4.1 we examined the effect of evolving spacetime parameters, the mass of black hole  $M_{\bullet}$  and its spin  $a$ , according to the accreted mass on the runaway instability. We found that the increasing of mass and the increasing of spin are mutually competing effects. While the increase of the black hole mass destabilises the partially accreted configuration, the spin increase has the opposite effect. These effects results in the change of a cusp and torus centre positions. Consequently, if the specific angular momentum profile inside the torus is sufficiently steep (slope  $q$  is high enough) then the accretion of matter from the torus has a stabilising effect against the runaway instability. On the other hand, small  $q$  causes rapid accretion. Further, we examined the role of the purely toroidal magnetic field permeating the torus on the evolution of perturbed tori. We found that the magnetic field has a significant impact if the magnetic pressure is comparable with the thermodynamical pressure. In those cases the magnetic field plays an important role in the early phases of accretion until the perturbed configuration finds a new equilibrium or totally disappears due to runaway instability.

In Section 4.2 we studied the scenario of repetitive perturbations of the torus, which was considered as a toy-model of star-disc collisions disrupting the inner torus. These perturbations accelerate the material of the torus in the vertical direction. This expelled material is consequently either accreted by the black hole or launched outward along the rotation axis. We studied the dependence of the outflow velocities on the strength and geometry of the magnetic field. We found that the maximal outflow velocity depends on the magnetization parameter  $\beta$ . If  $\beta \leq 10$  then there is a rapid increase of the maximal outflow velocity. The fraction of the torus that persists when the perturbations are switched off is determined by the the size of the torus which undergoes these perturbations. When the perturbations are switched off, typically at late times, then the oscillations are suppressed and the torus regains almost the equilibrium configuration with very small accretion rate.

Among the principal results of the present work we can mention the study and numerical modelling of the vertical outflows from a magnetised torus that can be expected by the passage of a stellar body. This includes the discussion of repetitive triggering which can enhance the perturbation when the star orbits at an appropriate radius. We suggest that this mechanism can supply material from the torus into the Coronal region near the rotation axis, where it can be further accelerated.



## 7. Future perspectives

During my doctoral study new features were added to the publicly available version of the HARM code, namely, the possibility of evolving parameters of Kerr metric (the spin and the mass) by the accreted matter feedback (Hamerský & Karas 2013). We plan to add further new features, so as we could evolve accretion tori in non-Kerr backgrounds. In this Thesis, we also studied the influence of the magnetic field and the profile of specific angular momentum inside the torus on the runaway instability (Hamerský & Karas 2013). Although the basic idea behind the runaway instability is well-known for several decades, an inclusion of additional effects makes the discussion more complex. However, if we restrict ourselves to the study of simplified model, we can on the other hand focus on the particular effects due to the magnetic field and angular momentum radial distribution, and more precisely investigate their role. In our simulations the Kerr background was evolving and the oscillation properties exhibited variations for different parameters of the Kerr spacetime and accretion torus (Hamerský & Karas 2015).

It is expected that astronomical compact objects with mass greater than  $3 M_{\odot}$  finish their evolution as Kerr black holes. This is known as the Kerr hypothesis. However, this hypothesis has not yet been definitively confirmed (neither rejected) by observations. Spacetimes with parametric deviations from the Kerr metric are expected to contain additional nonvanishing moments of the gravitational field, singularities, or regions with closed timelike curves outside of the event horizon. For all these currently proposed metrics, pathologies take place very close to the corresponding Kerr event horizon and far inside the location of the photon orbit and ISCO (which dominate the observational characteristics of black holes). It means that they do not hinder tests which contain orbits of objects at large distances from the horizon. Performing analogical GRMHD simulations for non-Kerr sources and studying their specific oscillation characteristics should provide a tool to test the “Kerrness” (i.e. potential departures from the perfectly accurate Kerr solution) of the source using the frequency analysis of observed electromagnetic spectra.

The numerical approach allows us to relax several constraints which have been often imposed in previous analytical works. In particular, the magnetic field does not have to share a common symmetry axis with the spin of the black hole; quite on the contrary, the lines of magnetic force as well as velocity field of the fluid can develop poloidal as well as toroidal component that interact with each other. These inclined fields violate axial symmetry and their evolution is highly dynamical. Also, the black hole does not have to remain at rest but it can instead perform a fast translational motion together with rotation. To explore the effects of translatory motion (boost) of the black hole is among possible future topic of our investigations.

The topological changes that the drift causes upon the field structure, especially the formation of the neutral points indicate that the strong gravitation of the rotating Kerr source may itself entangle an initially uniform magnetic field in a surprisingly complex manner. Astrophysical consequences of this still remain

under discussion. Gravity of the rotating black hole can act as a trigger for magnetic reconnection. What remains to be further explored is the speed and the overall efficiency of the reconnection process.

# Appendix - Derivation of certain equations

In this Appendix, for reader's convenience, I summarize derivation of the essential relations that have been used throughout the Thesis and in the numerical procedures. The relations and notation follow the traditional approach, as described, for example, in Misner et al. (1973); Stephani (1982).

## A.1 Equations (2.32) and (2.33)

From the normalization condition for four-velocity

$$u_\mu u^\mu = -1$$

and realizing that

$$u^\mu = (u^t, 0, 0, u^\varphi)$$

and

$$u^\varphi = u^t \Omega$$

we get

$$A^2(g_{tt} + 2\Omega g_{t\varphi} + g_{\varphi\varphi}\Omega^2) = -1,$$

from which it follows:

$$A = \frac{1}{\sqrt{-(g_{tt} + 2\Omega g_{t\varphi} + g_{\varphi\varphi}\Omega^2)}}. \quad (1)$$

For  $u_\varphi$  we can write

$$u_\varphi = g_{t\varphi}A + g_{\varphi\varphi}A\Omega$$

and using the normalization condition we obtain

$$u_t A = -1 - (g_{t\varphi}A^2\Omega + g_{\varphi\varphi}A^2\Omega^2).$$

From the last equation we get

$$u_t (\equiv U) = \frac{-1 - g_{t\varphi}A^2\Omega - g_{\varphi\varphi}A^2\Omega^2}{A}.$$

Now we use equation (1) to rewrite  $U$  as

$$\begin{aligned} U &= \sqrt{-(g_{tt} + 2\Omega g_{t\varphi} + g_{\varphi\varphi}\Omega^2)} \cdot \frac{-g_{tt} - 2\Omega g_{t\varphi} - g_{\varphi\varphi}\Omega^2 + g_{t\varphi}\Omega + g_{\varphi\varphi}\Omega^2}{g_{tt} + 2\Omega g_{t\varphi} + g_{\varphi\varphi}\Omega^2} \\ &= \frac{-g_{tt} - g_{t\varphi}\Omega}{\sqrt{-(g_{tt} + 2\Omega g_{t\varphi} + g_{\varphi\varphi}\Omega^2)}}. \end{aligned}$$

We employ an expression for the angular velocity  $\Omega = -\frac{g_{t\varphi} + l g_{tt}}{g_{\varphi\varphi} + l g_{t\varphi}}$ , insert it into the last equation and after a simple algebraic manipulation we finally get

$$U = \frac{\sqrt{g_{t\varphi}^2 - g_{tt}g_{\varphi\varphi}}}{\sqrt{g_{\varphi\varphi} + 2l g_{t\varphi} + l^2 g_{tt}}}. \quad (2)$$

## A.2 Equation (2.44)

Let us assume an energy momentum tensor in the form

$$T^\gamma_\nu = (w + b^2)u^\gamma u_\nu + \left(p + \frac{1}{2}b^2\right)g^\gamma_\nu - b^\gamma b_\nu. \quad (3)$$

From the conservation law we know that  $T^\gamma_{\nu;\gamma} = 0$ . We can multiply this equation by the projection tensor  $h^\nu_i \equiv \delta^\nu_i + u^\nu u_i$ , where  $i = r, \vartheta$ . Then we get

$$h^\nu_i [(w + b^2)u^\gamma u_\nu]_{;\gamma} + h^\nu_i \left[ \left(p + \frac{b^2}{2}\right) \delta^\gamma_\nu \right]_{;\gamma} - h^\nu_i (b^\gamma b_\nu)_{;\gamma} = 0. \quad (4)$$

In order to rewrite this equation we use the following relations:  $h^\alpha_\beta u_\alpha = 0$  and  $u^\alpha u_{\alpha;\gamma} = 0$ , which reflect that a four-velocity is perpendicular to a four-acceleration and the expression for covariant divergence of four-vector:  $V^\mu_{;\mu} = \frac{1}{\sqrt{-g}}(\sqrt{-g}V^\mu)_{,\mu}$ . Now we evaluate the first term in equation (4):

$$\begin{aligned} h^\nu_i [(w + b^2)u^\gamma u_\nu]_{;\gamma} &= (w + b^2)[(u^\gamma u_\nu)_{;\gamma}]h^\nu_i \\ &= (w + b^2)[u^\gamma_{;\gamma} u_\nu h^\nu_i + u_{\nu;\gamma} u^\gamma h^\nu_i] \\ &= (w + b^2)[u_{\nu;\gamma} u^\gamma h^\nu_i] = (w + b^2)[u_{i;\gamma} u^\gamma] \\ &= (w + b^2)[(u^\gamma u_i)_{;\gamma} - u_i u^\gamma_{;\gamma}]. \end{aligned} \quad (5)$$

The last term in square brackets is zero due to symmetry conditions and for  $(u^\gamma u_i)_{;\gamma}$  we can write

$$(u^\gamma u_i)_{;\gamma} = \frac{1}{\sqrt{-g}}(\sqrt{-g}u^\gamma u_i)_{,\gamma} - \frac{1}{2}g_{\mu\nu,i}u^\mu u^\nu, \quad (6)$$

where the first term on the right is zero due to symmetry conditions and the second term can be rewritten as  $g_{\mu\nu,i}u^\mu u^\nu = -2u_\nu u^\nu_{,i}$ . So finally we can write the first term in equation (4) as

$$h^\nu_i [(w + b^2)u^\gamma u_\nu]_{;\gamma} = (w + b^2)u_\mu u^\mu_{,i}. \quad (7)$$

The second term in eq. (4) can be rewritten as

$$\begin{aligned} h^\nu_i \left[ \left(p + \frac{b^2}{2}\right) \delta^\gamma_\nu \right]_{;\gamma} &= h^\gamma_i \left(p + \frac{b^2}{2}\right)_{,\gamma} \\ &= \left(p + \frac{b^2}{2}\right)_{,i} + u_i u^\gamma \left(p + \frac{b^2}{2}\right)_{,\gamma}, \end{aligned} \quad (8)$$

where the last term is zero due to symmetry conditions. We rewrite the third term in eq. (4):

$$\begin{aligned} h^\nu_i (b^\gamma b_\nu)_{;\gamma} &= h^\nu_i \left( \frac{1}{\sqrt{-g}}(\sqrt{-g}b^\gamma b_\nu)_{,\gamma} - \frac{1}{2}g_{\alpha\beta,\nu}b^\alpha b^\beta \right) \\ &= -\frac{1}{2}h^\nu_i g_{\alpha\beta,\nu}b^\alpha b^\beta \\ &= -\frac{1}{2}(g_{\alpha\beta,i}b^\alpha b^\beta + u_i b^\alpha b^\beta u^\nu g_{\alpha\beta,\nu}) \\ &= -\frac{1}{2}g_{\alpha\beta,i}b^\alpha b^\beta = -\frac{1}{2}(b^2_{,i} - 2b_\nu b^\nu_{,i}) \end{aligned} \quad (9)$$

and finally we get

$$(w + b^2)u_\mu u^\mu + (p + b^2)_{,i} - b_\nu b^\nu_{,i} = 0. \quad (10)$$

### A.3 Equation (2.45)

Taking into account equations (2.25), (2.28), (2.32), (2.33) and (2.34) we can evaluate  $u_t$  as

$$(u_t)^2 = \frac{\mathcal{L}}{\mathcal{A}}, \quad (11)$$

where  $\mathcal{L} \equiv g_{t\varphi}^2 - g_{tt}g_{\varphi\varphi}$  and  $\mathcal{A} \equiv g_{\varphi\varphi} + 2lg_{t\varphi} + l^2g_{tt}$ . Thanks to the fact that  $b_\mu u^\mu = 0$  we get:

$$\begin{aligned} b_t &= -\frac{u^\varphi}{u^t}b_\varphi = -\Omega b_\varphi, \\ b^t &= -\frac{u_\varphi}{u_t}b^\varphi = lb^\varphi, \\ b^2 &= b_\varphi b^\varphi(1 - \Omega l). \end{aligned} \quad (12)$$

For  $b^2$  we can also write:

$$\begin{aligned} b^2 &= g_{\mu\nu}b^\mu b^\nu = g_{tt}(b^t)^2 + 2g_{t\varphi}(b^t b^\varphi) + g_{\varphi\varphi}(b^\varphi)^2 \\ &= g_{tt}l^2(b^\varphi)^2 + 2g_{t\varphi}l(b^\varphi)^2 + g_{\varphi\varphi}(b^\varphi)^2 \\ &= (b^\varphi)^2 \mathcal{A}. \end{aligned} \quad (13)$$

Now we evaluate  $u_\nu u^\nu_{,i}$ :

$$\begin{aligned} u_\nu u^\nu_{,i} &= -u^\nu u_{\nu,i} = -u^t u_{t,i} - u^\varphi u_{\varphi,i} \\ &= -u^t [u_{t,i} - \Omega(lu_t)_{,i}] = -u^t [u_{t,i}(1 - l\Omega) - \Omega u_t l_{,i}]. \end{aligned} \quad (14)$$

When we use the relation  $u_t u^t = -\frac{1}{1-l\Omega}$ , we get

$$u_\nu u^\nu_{,i} = \frac{1}{(1-l\Omega)u_t} [u_{t,i}(1 - l\Omega) - \Omega u_t l_{,i}] = (\ln |u_t|)_{,i} - \frac{\Omega}{1-l\Omega} l_{,i}. \quad (15)$$

Now we want to rewrite  $b_\nu b^\nu_{,i}$ :

$$\begin{aligned} b_\nu b^\nu_{,i} &= b_t b^t_{,i} + b_\varphi b^\varphi_{,i} = -\Omega b_\varphi (lb^\varphi)_{,i} + b_\varphi b^\varphi_{,i} \\ &= b_\varphi b^\varphi_{,i} (1 - \Omega l) - \Omega b_\varphi b^\varphi l_{,i}. \end{aligned} \quad (16)$$

Using equation (12) we obtain

$$\begin{aligned} b_\nu b^\nu_{,i} &= \frac{b^2}{b^\varphi(1 - \Omega l)} (1 - \Omega l) b^\varphi_{,i} - \frac{b^\varphi \Omega b^2}{b^\varphi(1 - \Omega l)} l_{,i} \\ &= b^2 (\ln |b^\varphi|)_{,i} - \frac{\Omega b^2}{(1 - \Omega l)} l_{,i}. \end{aligned} \quad (17)$$

When we use expressions for  $u_\nu u^\nu_{,i}$  and  $b_\nu b^\nu_{,i}$  derived above, we can rewrite equation (2.44) as

$$(w + b^2) \left[ (\ln |u_t|)_{,i} - \frac{\Omega}{1 - l\Omega} l_{,i} \right] + (p + b^2)_{,i} - b^2 (\ln |b^\varphi|)_{,i} + \frac{\Omega b^2}{(1 - \Omega l)} l_{,i} = 0$$

$$w \left[ (\ln |u_t|)_{,i} - \frac{\Omega}{1 - l\Omega} l_{,i} \right] + p_{,i} + b^2 \left( \ln \left| \frac{u_t}{b^\varphi} \right| \right)_{,i} + b^2_{,i} = 0. \quad (18)$$

The last two terms can be rewritten using equations (11) and (12):

$$b^2 \left( \ln \left| \frac{u_t}{b^\varphi} \right| \right)_{,i} + b^2_{,i} = b^2 \left( \ln \frac{\sqrt{\mathcal{L}}}{b} \right)_{,i} + b^2_{,i}$$

$$= b^2 \left( \frac{\mathcal{L}_{,i}}{2\mathcal{L}} - \frac{b_{,i}}{b} \right) + b^2_{,i} = \frac{(\mathcal{L}b^2)_{,i}}{2\mathcal{L}}. \quad (19)$$

Finally we get

$$(\ln |u_t|)_{,i} - \frac{\Omega}{1 - l\Omega} l_{,i} + \frac{p_{,i}}{w} + \frac{(\mathcal{L}b^2)_{,i}}{2\mathcal{L}w} = 0. \quad (20)$$

#### A.4 Equation (2.53)

Using definitions (2.32), (2.33) and (2.34) and realizing that from the normalization condition,  $U^{-2} = (-g^{tt} + 2lg^{t\varphi} - g^{\varphi\varphi}l^2)$ , we can rewrite the Euler equation (2.35) as

$$\begin{aligned} \frac{\nabla p}{p + \epsilon} &= \nabla(\ln A) - \frac{l}{1 - \Omega l} \nabla \Omega = \frac{\nabla A}{A} - \frac{l}{1 - \Omega l} \nabla \Omega \\ &= -\frac{U(1 - \Omega l)}{U^2(1 - \Omega l)^2} [(1 - \Omega l)\nabla U + U\nabla(1 - \Omega l)] - \frac{l\nabla \Omega}{1 - \Omega l} \\ &= -\frac{(1 - \Omega l)\nabla U + U\nabla(1 - \Omega l)}{U(1 - \Omega l)} - \frac{l\nabla \Omega}{1 - \Omega l} \\ &= -\frac{\nabla U}{U} - \frac{\nabla(1 - \Omega l)}{1 - \Omega l} - \frac{l\nabla \Omega}{1 - \Omega l} = -\frac{\nabla U}{U} + \frac{\Omega \nabla l}{1 - \Omega l} \\ &= \frac{1}{2}(-g^{tt} + 2lg^{t\varphi} - g^{\varphi\varphi}l^2)^{-1} [-\nabla g^{tt} + 2\nabla(lg^{t\varphi}) - \nabla(g^{\varphi\varphi}l^2)] + \frac{\Omega \nabla l}{1 - \Omega l} \\ &= \frac{1 - \nabla g^{tt} + 2l\nabla g^{t\varphi} - l^2\nabla g^{\varphi\varphi}}{-g^{tt} + 2lg^{t\varphi} - g^{\varphi\varphi}l^2} + \frac{1}{2} \frac{2(g^{t\varphi} - lg^{\varphi\varphi})\nabla l}{-g^{tt} + 2lg^{t\varphi} - g^{\varphi\varphi}l^2} + \frac{\Omega \nabla l}{1 - \Omega l}. \quad (21) \end{aligned}$$

Now we show the following relation:

$$\frac{(g^{t\varphi} - lg^{\varphi\varphi})\nabla l}{-g^{tt} + 2lg^{t\varphi} - g^{\varphi\varphi}l^2} = -\frac{\Omega \nabla l}{1 - \Omega l}. \quad (22)$$

The equality (22) is valid if

$$(g^{t\varphi} - lg^{\varphi\varphi})(1 - \Omega l) = -\Omega(-g^{tt} + 2lg^{t\varphi} - g^{\varphi\varphi}l^2), \quad (23)$$

which leads to

$$\begin{aligned} g^{t\varphi}(1 + \Omega l) - lg^{\varphi\varphi} - \Omega g^{tt} &= 0 \\ 1 + \Omega l &= \frac{\Omega g^{tt} + lg^{\varphi\varphi}}{g^{t\varphi}} \\ 1 - \frac{u^\varphi u_\varphi}{u^t u_t} &= \frac{g^{tt} \frac{u^\varphi}{u^t} - g^{\varphi\varphi} \frac{u_\varphi}{u_t}}{g^{t\varphi}}. \end{aligned}$$

Using the normalization condition for a four-velocity we get from the last equation:

$$\begin{aligned} 1 + \frac{1 + u^t u_t}{u^t u_t} &= \frac{g^{tt} u^\varphi u_t - g^{\varphi\varphi} u^t u_\varphi}{u^t u_t g^{t\varphi}} \frac{u_t u_\varphi}{u_t u_\varphi} \\ &= \frac{g^{tt} (u_t)^2 u^\varphi u_\varphi - g^{\varphi\varphi} (u_\varphi)^2 u^t u_t}{u^t u_t g^{t\varphi} u_t u_\varphi} \\ &= \frac{-g^{tt} (u_t)^2 - g^{tt} (u_t)^2 u^t u_t - g^{\varphi\varphi} (u_\varphi)^2 u^t u_t}{u^t u_t g^{t\varphi} u_t u_\varphi} \\ &= \frac{-g^{tt} (u_t)^2 - u_t u^t (-1 - 2g^t u_t u_\varphi)}{u^t u_t g^{t\varphi} u_t u_\varphi} \\ &= \frac{-g^{tt} (u_t)^2 + u_t u^t}{u_t u^t g^{t\varphi} u_t u_\varphi} + \frac{2g^{t\varphi} u_t u_\varphi u_t u^t}{u_t u^t g^{t\varphi} u_t u_\varphi} \\ &= 2 + \frac{1}{u^t u_t}, \end{aligned} \quad (24)$$

where we used:  $-g^{tt} (u_t)^2 + u_t u^t = -g^{tt} (u_t)^2 + u_t (g^{tt} u_t + g^{t\varphi} u_\varphi) = g^{t\varphi} u_t u_\varphi$ . Finally, we showed that equality (22) is valid and therefore we can write the Euler equation (21) in the form

$$\frac{\nabla p}{p + \epsilon} = -\frac{1}{2} U^2 (\nabla g^{tt} - 2l \nabla g^{t\varphi} + l^2 \nabla g^{\varphi\varphi}). \quad (25)$$

## A.5 Equation (2.56)

From the normalization condition for a four-velocity we get:

$$\begin{aligned} -1 &= g^{\mu\nu} u_\mu u_\nu \\ &= g^{tt} u_t u_t + 2g^{t\varphi} u_t u_\varphi + g^{\varphi\varphi} u_\varphi u_\varphi + g_{xx} u^x u^x \\ &= (u_t)^2 (g^{tt} - 2lg^{t\varphi} + l^2 g^{\varphi\varphi}) + g_{xx} u^x u^x, \end{aligned} \quad (26)$$

where  $x = r, \theta$ . Using the definitions  $U \equiv -u_t$  and  $\mathcal{U}_{eff} \equiv -\frac{1}{2} \ln(g^{tt} - 2lg^{t\varphi} + l^2 g^{\varphi\varphi})$  and considering small oscillations ( $\delta l = 0$ ,  $\delta U \neq 0$ ,  $\delta \dot{U} = 0$ ) that occur either in  $r$  or in  $\theta$  direction,  $x(s) - x_0 = \delta x$  and  $u^x \equiv \frac{dx}{ds} = \delta \dot{x}$ , we can write

$$-U^{-2} = e^{-2\mathcal{U}_{eff}} + \frac{g_{xx}}{U^2} (\delta \dot{x})^2. \quad (27)$$

The Taylor expansion starts from the second term,  $\delta x^2$ , and also ends there in the lowest order:

$$\begin{aligned} 2 \frac{\delta U}{U_0^3} &= \frac{1}{2} \left( \frac{\partial^2}{\partial x^2} e^{-2\mathcal{U}_{eff}} \right) (\delta x)^2 + \frac{g_{xx}}{U_0^2} (\delta \dot{x})^2 \\ 2 \frac{\delta \dot{U}}{U_0^3} &= (\delta \dot{x}) \left[ \left( \frac{\partial^2}{\partial x^2} e^{-2\mathcal{U}_{eff}} \right) \delta x + 2 \frac{g_{xx}}{U_0^2} \delta \ddot{x} \right]. \end{aligned} \quad (28)$$

When we set  $\delta \dot{U} = 0$  and  $\delta \dot{x} \neq 0$  then the latter has the form of a simple harmonic oscillator equation:  $0 = \omega_x^2 \delta x + \delta \ddot{x}$  with the frequency  $\omega_x$  equal to

$$\omega_x^2 = \frac{U_0^2}{2g_{xx}} \left( \frac{\partial^2}{\partial x^2} \mathcal{U} \right). \quad (29)$$

To obtain the frequency measured by an observer at infinity  $\omega_x^*$ , we have to rescale it by the redshift factor  $A$ . Then we get

$$\omega_x^{*2} = \frac{U_0^2}{A_0^2} \left( \frac{1}{2g_{xx}} \frac{\partial^2}{\partial x^2} \mathcal{U} \right). \quad (30)$$

## A.6 Equation (2.59)

Let us assume the relativistic Euler equation (2.53):

$$-\frac{\nabla_\alpha p}{p + \epsilon} = \frac{1}{2} U^2 (\nabla_\alpha g^{tt} - 2l \nabla_\alpha g^{t\varphi} + l^2 \nabla_\alpha g^{\varphi\varphi}). \quad (31)$$

If we subtract  $\frac{1}{2} U_0^2 \nabla_\alpha \mathcal{U}$ , where  $\mathcal{U}$  is defined in equation (2.55), from both sides of this equation, we obtain

$$\begin{aligned} -\frac{\nabla_\alpha p}{p + \epsilon} - \frac{1}{2} U_0^2 \nabla_\alpha \mathcal{U} &= \frac{1}{2} (U^2 - U_0^2) \nabla_\alpha g^{tt} - (U^2 l - U_0^2 l_0) \nabla_\alpha g^{t\varphi} \\ &\quad + \frac{1}{2} (U^2 l^2 - U_0^2 l_0^2) \nabla_\alpha g^{\varphi\varphi}. \end{aligned} \quad (32)$$

For a barotropic fluid,  $p = p(\epsilon)$ , the left hand side of this equation is the gradient of a scalar function. Thus, the right hand side has to be the gradient of a scalar

function too. Following Abramowicz et al. (2006) we denote it by  $\nabla_\alpha\psi$ . We can now define the function  $f = f(r, \theta)$  as

$$\frac{p}{\rho} = \frac{p_0}{\rho_0} f(r, \theta),$$

$$f(r, \theta) = 1 - \frac{1}{nc_{s0}^2} \left[ \frac{U_0^2}{2} (\mathcal{U} - \mathcal{U}_0) + \psi \right], \quad (33)$$

where  $c_{s0} = \sqrt{\frac{(n+1)p}{n\rho}}$  is the sound speed at the torus centre. Now we want to evaluate the function  $f$  in the vicinity of the torus centre. It is convenient to introduce new coordinates  $x, y$ :

$$dx \equiv \sqrt{g_{rr}} dr / r_0$$

and

$$dy \equiv -\sqrt{g_{\theta\theta}} d\theta / r_0. \quad (34)$$

These coordinates satisfy  $x = y = 0$  at the torus centre. Using these coordinates we can write

$$\mathcal{U} - \mathcal{U}_0 = \frac{r_0^2}{2} \left[ \frac{1}{g_{rr}} \left( \frac{\partial^2 \mathcal{U}}{\partial r^2} \right)_0 x^2 + \frac{1}{g_{\theta\theta}} \left( \frac{\partial^2 \mathcal{U}}{\partial \theta^2} \right)_0 y^2 \right], \quad (35)$$

where all metric coefficients are evaluated at the torus centre. In the vicinity of the equilibrium point the potential  $\psi$  can be expressed as

$$\psi = -\frac{U_0^2}{2g_{rr}} (g_{,r}^{tt} - l_0 g_{,r}^{t\varphi}) \frac{1}{l_0} \left( \frac{\partial l}{\partial r} \right)_0 r_0^2 x^2. \quad (36)$$

Taking into account expression for epicyclic frequencies (30), and equations (33), (35), (36) we can write for the function  $f$ :

$$\begin{aligned} f &= 1 - \frac{1}{nc_{s0}^2} \left[ \frac{U_0^2}{2} (\mathcal{U} - \mathcal{U}_0) - \frac{U_0^2}{2g_{rr}} (g_{,r}^{tt} - l_0 g_{,r}^{t\varphi}) \frac{1}{l_0} \left( \frac{\partial l}{\partial r} \right)_0 r_0^2 x^2 \right] \\ &= 1 - \\ &\frac{1}{nc_{s0}^2} \left\{ \frac{U_0^2}{2} \left[ \frac{r_0^2}{2} \left( \frac{x^2}{g_{rr}} \left( \frac{\partial^2 \mathcal{U}}{\partial r^2} \right)_0 + \frac{y^2}{g_{\theta\theta}} \left( \frac{\partial^2 \mathcal{U}}{\partial \theta^2} \right)_0 \right) \right] - \frac{U_0^2 (g_{,r}^{tt} - l_0 g_{,r}^{t\varphi})}{2g_{rr} l_0} \left( \frac{\partial l}{\partial r} \right)_0 r_0^2 x^2 \right\} \\ &= 1 - \frac{A_0^2}{nc_{s0}^2} \left[ \frac{1}{2} \omega_r^2 r_0^2 x^2 + \frac{1}{2} \omega_\theta^2 r_0^2 y^2 - \frac{(g_{,r}^{tt} - l_0 g_{,r}^{t\varphi}) U_0^2}{2g_{rr} A_0^2} \frac{1}{l_0} \left( \frac{\partial l}{\partial r} \right)_0 r_0^2 x^2 \right]. \quad (37) \end{aligned}$$

If we realize that

$$u_t = g_{tt} u^t + g_{t\varphi} u^\varphi = g_{tt} u^t + g_{t\varphi} u^t \Omega \Rightarrow \frac{U^2}{A^2} = \frac{u_t^2}{u^{t2}} = (g_{tt} + \Omega g_{t\varphi})^2, \quad (38)$$

we can write

$$\begin{aligned} f &= 1 - \\ &\frac{A_0^2 r_0^2 \Omega_0^2}{2nc_{s0}^2} \left\{ \left[ \frac{\omega_r^2}{\Omega_0^2} - \frac{(g_{,r}^{tt} - l_0 g_{,r}^{t\varphi}) (g_{tt} + \Omega_0 g_{t\varphi})^2}{g_{rr} \Omega_0^2} \frac{1}{l_0} \left( \frac{\partial l}{\partial r} \right)_0 \right] x^2 + \frac{\omega_\theta^2}{\Omega_0^2} y^2 \right\}. \quad (39) \end{aligned}$$

Now we define

$$2\mathcal{R}_0 \equiv \frac{(g_{tt} + \Omega_0 g_{t\varphi})^2}{g_{rr} \Omega_0^2} (g_{,r}^{tt} - l_0 g_{,r}^{t\varphi})$$

and

$$\zeta^2 \equiv \frac{2nc_{s0}^2}{A_0^2 r_0^2 \Omega_0^2}, \quad (40)$$

thanks to which we obtain the final expression for  $f$

$$f = 1 - \frac{1}{\zeta^2} \left\{ \left[ \tilde{\omega}_r^2 - \frac{2\mathcal{R}_0}{l_0} \left( \frac{\partial l}{\partial r} \right)_0 \right] x^2 + \tilde{\omega}_\theta^2 y^2 \right\}, \quad (41)$$

where  $\tilde{\omega}_r$  and  $\tilde{\omega}_\theta$  are the ratios of epicyclic frequencies to the orbital frequency  $\Omega_0$  at the torus centre.

## A.7 Equation (3.26)

$$\begin{aligned} T_{elmag}^{\mu\nu} &= \frac{n^\mu \tilde{B}^\lambda n^\nu \tilde{B}_\lambda \cdot (-n_\mu u^\mu)(-n_\nu u^\nu)}{\gamma \cdot \gamma} \\ &- \frac{1}{4} g^{\mu\nu} \frac{(n^\lambda \tilde{B}^\delta n_\lambda \tilde{B}_\delta + n^\delta \tilde{B}^\lambda n_\delta \tilde{B}_\lambda) \cdot (-n_\lambda u^\lambda)(-n_\lambda u^\lambda)}{\gamma \cdot \gamma} \\ &= \frac{\tilde{B}^\lambda \tilde{B}_\lambda u^\mu u^\nu}{\gamma \cdot \gamma} + \frac{1}{4} g^{\mu\nu} \frac{2 \cdot \tilde{B}^\delta \tilde{B}_\delta u^\lambda u_\lambda}{\gamma \cdot \gamma} \\ &= h^\lambda_\mu b^\mu h^\sigma_\mu b^\mu g_{\sigma\lambda} u^\mu u^\nu + \frac{1}{2} g^{\mu\nu} h^\delta_\mu b^\mu h^\sigma_\mu b^\mu g_{\sigma\delta} u^\lambda u_\lambda \\ &= g^\lambda_\mu b^\mu g^\sigma_\mu b^\mu g_{\sigma\lambda} u^\mu u^\nu + \frac{1}{2} g^{\mu\nu} g^\delta_\mu b^\mu g^\sigma_\mu b^\mu g_{\sigma\delta} u^\lambda u_\lambda \\ &= b^2 u^\mu u^\nu - \frac{1}{2} g^{\mu\nu} b^2 \\ &= b^2 u^\mu u^\nu + \frac{1}{2} g^{\mu\nu} b^2 - b^\mu b^\nu, \end{aligned} \quad (42)$$

where we used:

$$\begin{aligned} b^\mu u_\mu &= 0, \\ \tilde{B}^\nu &= \frac{1}{3} \gamma h^\nu_\mu b^\mu \end{aligned}$$

and

$$g^{\mu\nu} b^2 = g^{\mu\nu} b^\mu b_\mu = b^\mu b^\nu. \quad (43)$$

## A.8 Equation (3.45)

$$\begin{aligned}
\tilde{B}^\mu Q_\mu &= \gamma(w + b^2)u_\mu \tilde{B}^\mu + (n_\nu b^\nu) \frac{1}{\gamma} h_\mu^\nu \tilde{B}_\nu \tilde{B}^\mu \\
&= \gamma(w + b^2)u_\mu \tilde{B}^\mu + (n_\nu b^\nu) \frac{1}{\gamma} (\tilde{B}^\mu \tilde{B}_\mu + u^\mu \tilde{B}_\mu u^\nu \tilde{B}_\nu) \\
&= \gamma(w + b^2)u_\mu \tilde{B}^\mu + \frac{1}{\gamma^2} n_\nu (\tilde{B}^\nu + u^\nu u_\mu \tilde{B}^\mu) (\tilde{B}^2 + (u_\mu \tilde{B}^\mu)^2) \\
&= \frac{W}{\gamma} (u_\mu \tilde{B}^\mu)
\end{aligned} \tag{44}$$

## A.9 Equation (3.46)

$$\begin{aligned}
Q_\mu n^\mu &= -\gamma^2(w + b^2) + \left(p + \frac{b^2}{2}\right) + (n_\nu b^\nu)^2 \\
&= -\gamma^2 \left(w + \frac{1}{\gamma^2} [\tilde{B}^2 + (\tilde{B}^\mu u_\mu)^2]\right) + \left(p + \frac{1}{2\gamma^2} [\tilde{B}^2 + (\tilde{B}^\mu u_\mu)^2]\right) + (u_\mu \tilde{B}^\mu)^2 \\
&= -W - \tilde{B}^2 - (\tilde{B}^\mu u_\mu)^2 + p + \frac{\tilde{B}^2 + (\tilde{B}^\mu u_\mu)^2}{2\gamma^2} + (u_\mu \tilde{B}^\mu)^2 \\
&= -\frac{\tilde{B}^2}{2}(1 + v^2) + \frac{(\tilde{B}^\mu Q_\mu)^2}{2W^2} - W + p
\end{aligned} \tag{45}$$

### A.10 Equation (3.49)

$$\begin{aligned}
Q_\mu Q^\mu &= -\gamma^2(w+b^2)^2 - \left(p + \frac{b^2}{2}\right)^2 + (n_\nu b^\nu)^2 b^2 - 2\gamma(w+b^2) \left(p + \frac{b^2}{2}\right) u_\mu n^\mu \\
&\quad + 2\gamma(w+b^2)(n_\nu b^\nu) u_\mu b^\mu - 2 \left(p + \frac{b^2}{2}\right) (n_\nu b^\nu) n_\mu b^\mu \\
&= -\gamma^2 \left( w + \frac{1}{\gamma^2} \left[ \tilde{B}^2 + (\tilde{B}^\mu u_\mu)^2 \right] \right)^2 + 2\gamma^2 \left( w + \frac{1}{\gamma^2} \left[ \tilde{B}^2 + (\tilde{B}^\mu u_\mu)^2 \right] \right) \\
&\quad \cdot \left( p + \frac{1}{2\gamma^2} \left[ \tilde{B}^2 + (\tilde{B}^\mu u_\mu)^2 \right] \right) - \left( p + \frac{1}{2\gamma^2} \left[ \tilde{B}^2 + (\tilde{B}^\mu u_\mu)^2 \right] \right)^2 \\
&\quad - 2p \cdot (u_\mu \tilde{B}^\mu)^2 \\
&= - \left( \frac{W}{\gamma} + \frac{1}{\gamma} \left[ \tilde{B}^2 + \frac{(\tilde{B}^\mu Q_\mu)^2 \gamma^2}{W^2} \right] \right)^2 + \left( 2W + 2 \left[ \tilde{B}^2 + \frac{(\tilde{B}^\mu Q_\mu)^2 \gamma^2}{W^2} \right] \right) \\
&\quad \cdot \left( p + \frac{1}{2\gamma^2} \left[ \tilde{B}^2 + \frac{(\tilde{B}^\mu Q_\mu)^2 \gamma^2}{W^2} \right] \right) - \left( p + \frac{1}{2\gamma^2} \left[ \tilde{B}^2 + \frac{(\tilde{B}^\mu Q_\mu)^2 \gamma^2}{W^2} \right] \right)^2 \\
&\quad - 2p \frac{(\tilde{B}^\mu Q_\mu)^2 \gamma^2}{W^2} \\
&= -W^2(1-v^2) + 2Wp - p^2 + \tilde{B}^2 \left( -\frac{W}{\gamma^2} + p(1+v^2) - \frac{(\tilde{B}^\mu Q_\mu)^2}{2W^2\gamma^2} \right) \\
&\quad + \frac{(\tilde{B}^\mu Q_\mu)^2 \gamma^2}{W^2} \left( -\frac{W}{\gamma^2} + p(v^2-1) \right) - \frac{1}{4\gamma^4} \left( \tilde{B}^4 + \frac{(\tilde{B}^\mu Q_\mu)^4 \gamma^4}{W^4} \right). \tag{46}
\end{aligned}$$

## A.11 List of symbols

Variable	Description	Definition
$a$	black hole spin	$a \equiv \frac{J}{M}$
$A$	redshift	$A \equiv u_t$
$\mathcal{A}$		$\mathcal{A} \equiv g_{\varphi\varphi} + 2lg_{t\varphi} + l^2g_{tt}$
$\beta$	magnetization	$\beta \equiv \frac{p_m}{\rho_0}$
$B^i$	magnetic field vector	$B^i \equiv {}^*F^{it}$
$\tilde{B}^\mu$	magnetic field four-vector	$\tilde{B}^\mu \equiv -n_\nu {}^*F^{\mu\nu}$
$c$	speed of light in vacuum	
$\epsilon$	total energy density	
$E$	energy	
$\vec{E}$	electric field vector	
$F$		$F \equiv (1 - \Omega l) \exp \int_{l_{in}}^l (1 - \Omega l)^{-1} \Omega dl$
$F^{\mu\nu}$	electromagnetic field tensor	
$g_{\mu\nu}$	metric tensor	
$G$	gravitational constant	
$l$	specific angular momentum	$l \equiv -\frac{u_\varphi}{u_t}$
$\mathcal{L}$		$\mathcal{L}(r, \vartheta) \equiv g_{t\varphi}^2 - g_{tt}g_{\varphi\varphi}$
$M_\bullet$	black hole mass	
$M_\odot$	solar mass	
$\nu$	kinematic viscosity	
$\omega_r$	radial epicyclic frequency	
$\omega_\theta$	vertical epicyclic frequency	
$\Omega$	angular velocity	$\Omega \equiv \frac{u^\varphi}{u^t}$
$p$	thermodynamical pressure	
$p_m$	magnetic pressure	
$\rho$	mass density	
$\rho_0$	rest mass density	
$T^{\mu\nu}$	energy-momentum tensor	
$u$	internal energy density	
$u^\mu$	four-velocity	
$U$	energy per unit inertial mass	$U \equiv u_t$
$\mathcal{U}$	effective potential	$\mathcal{U} \equiv g^{tt} - 2l_0g^{t\varphi} + l_0^2g^{\varphi\varphi}$
$w$	specific enthalpy	$w \equiv \rho_0 + p + u$
$W$		$W \equiv -\ln(FA)$
$\mathcal{W}$	scalar perturbation variable	$\mathcal{W} \equiv -\frac{\delta p}{\rho_0 A \sigma}$
$\zeta$	thickness of the torus	$\zeta^2 \equiv \frac{2(n+1)p_0}{\rho_0 A_0^2 r_0^2 \Omega_0^2}$



# Bibliography

- Abramowicz M. A. (1971). The Relativistic von Zeipel's Theorem. *Acta Astronomica*, 21, 81.
- Abramowicz M. A., Jaroszyński M., & Sikora M. (1978). Relativistic, accreting disks. *A&A*, 63, 221.
- Abramowicz M. A., Calvani M., & Nobili L. (1983). Runaway instability in accretion disks orbiting black holes. *Nature*, 302, 597.
- Abramowicz M. A., Karas V., & Lanza A. (1998). On the runaway instability of relativistic tori. *A&A*, 331, 1143.
- Abramowicz M. A., Blaes O. M., Horák J et al. (2006). Epicyclic oscillations of fluid bodies: II. Strong gravity. *Class. Quantum Gravity*, 23, 1689.
- Abramowicz M. A., Czerny B., Lasota J. P. & Szuszkiewicz E. (1988). Slim accretion disks. *ApJ*, 332, 646.
- Agudo I. (2015). Studies of Relativistic Jets in Active Galactic Nuclei with SKA. eprint arXiv:1501.00420.
- Alexander T. & Hopman C. (2003). Orbital In-spiral into a Massive Black Hole in a Galactic Center. *ApJ*, 590, L29.
- Anninos P., Fragile P. C., Salmonson J. D. (2005). Cosmos++: Relativistic Magnetohydrodynamics on Unstructured Grids with Local Adaptive Refinement. *ApJ*, 635, 723.
- Antonucci R. (1993). Unified models for active galactic nuclei and quasars. *Annual review of astronomy and astrophysics*, 31, 473.
- Abramowicz M. A., & Fragile P. C. (2013). Foundations of Black Hole Accretion Disk Theory. *Living Reviews in Relativity*, 16, 1.
- Anile A. M. (1989). *Relativistic Fluids and Magneto-Fluids*. Cambridge University Press, Cambridge.
- Artymowicz P., Lin D. N. C. & Wampler E. J. (1993). Star trapping and metallicity enrichment in quasars and active galactic nuclei. *ApJ*, 409, 592.
- Baganoff F., Bautz M. W., Brandt W. N. (2001). Rapid X-ray flaring from the direction of the supermassive black hole at the Galactic Centre. *Nature*, 413, 45.
- Bakala P., Urbanec M., Šrámková E., et al. (2012). On magnetic-field-induced corrections to the orbital and epicyclic frequencies: paper II. Slowly rotating magnetized neutron stars. *Classical and Quantum Gravity*, 29, 065012.

- Balbus S. A., & Hawley J. F. (1991). A powerful local shear instability in weakly magnetized disks. I - Linear analysis. II - Nonlinear evolution. *ApJ*, 376, 214.
- Balick B., Brown R. L. (1974). Intense sub-arcsecond structure in the galactic center. *ApJ*, 194, 265.
- Bans A., Königl A. & Uribe A. (2015). Type I Planet Migration in a Magnetized Disk. II. Effect of Vertical Angular Momentum Transport. ArXiv e-prints.
- Barkov M. V., & Baushev A. N. (2011). Accretion of a massive magnetized torus on a rotating black hole. *New Astronomy*, 16, 46.
- Barkov M. V. & Komissarov S. S. (2008). Stellar explosions powered by the Blandford-Znajek mechanism. *MNRAS*, 385, L28.
- Beckwith K., Hawley J. F. & Krolik J. H. (2008). The Influence of Magnetic Field Geometry on the Evolution of Black Hole Accretion Flows: Similar Disks, Drastically Different Jets. *ApJ*, 678, 1180.
- Begelman M. C. (1999). *High Energy Processes in Accreting Black Holes*. Astronomical Society of the Pacific Conference Series, Vol. 161.
- Bélangier G., Terrier R., De Jager O. C., Goldwurm A. (2006). Periodic Modulations in an X-ray Flare from Sagittarius A\*. *Journal of Physics: Conference Series*, 54, 420.
- Bisnovatyi-Kogan G., Klepnev A. S. & Lovelace R. V. E. (2013). Accretion Disks with a Large Scale Magnetic Field Around Black Holes. *Acta Polytechnica*, 53, 677.
- Blaes O. (1985). Oscillations of slender tori. *MNRAS*, 216, 553.
- Blaes O., Arras P., & Fragile P. C. (2006). Oscillation modes of relativistic slender tori. *MNRAS*, 369, 1235.
- Blaes O., Šrámková E., Abramowicz M et al. (2007). Epicyclic Oscillations of Fluid Bodies: Newtonian Nonslender Torus. *ApJ*, 665, 642.
- Blaes O. (2014). General Overview of Black Hole Accretion Theory. *Space Science Reviews*, 183, 21.
- Blandford R. D., Znajek R. L. (1977). Electromagnetic extraction of energy from Kerr black holes. *MNRAS*, 179, 433.
- Blandford R. D., Payne D. G. (1982). Hydromagnetic flows from accretion discs and the production of radio jets. *MNRAS*, 199, 883.
- Bondi H. (1952). On spherically symmetrical accretion. *MNRAS*, 112, 195.
- Bonzini M., Padovani P., Mainieri V. (2013). The sub-mJy radio sky in the Extended Chandra Deep Field-South: source population. *MNRAS*, 436, 3759.

- Chang P. (2009). The effectiveness of the Kozai mechanism in the Galactic Centre. *MNRAS*, 393, 224.
- Carollo C. M., Stiavelli M., Seigar M., et al. (2002). Spiral Galaxies with HST/NICMOS. I. Nuclear Morphologies, Color Maps, and Distinct Nuclei. *The Astronomical Journal*, 123, 159.
- Chakrabarti S. K. (1991). Von Zeipel surfaces. II-A catalogue. *MNRAS*, 250, 7.
- Czerny B. & Hryniewicz K. (2011). The origin of the broad line region in active galactic nuclei. *A&A*, 525, L8.
- Czerny B., Kunneriath D., Karas V. & Das T. K. (2013). Multiple accretion events as a trigger for Sagittarius A\* activity. *A&A*, 555, A97.
- Dai L. J., Fuerst S. V. & Blandford R. (2010). Quasi-periodic flares from star-accretion-disc collisions. *MNRAS*, 402, 1614.
- Daigne F., & Mochkovitch R. (1997). Gamma-ray bursts and the runaway instability of thick discs around black holes. *MNRAS*, 285, L15.
- Dale J. E., Davies M. B., Church R. P. & Freitag M. (2009). Red giant stellar collisions in the Galactic Centre. *MNRAS*, 393, 1016.
- De Villiers J. P. & Hawley J. F. (2003). A Numerical Method for General Relativistic Magnetohydrodynamics. *ApJ*, 589, 458.
- De Villiers J.-P., Hawley J. F. & Krolik J. H. (2003). Magnetically Driven Accretion Flows in the Kerr Metric. I. Models and Overall Structure. *ApJ*, 599, 1238.
- Done C., Madejski G. M. & Życki P. T. (2000). The Relativistic Iron Line Profile in the Seyfert 1 Galaxy IC 4329A. *ApJ*, 536, 213.
- Fabian A. C., Pounds K. A., Blandford R. D. (2004). *Frontiers of X-ray astronomy*. Cambridge University Press, Cambridge.
- Ferriere K. (2009). Interstellar magnetic fields in the Galactic center region. *A&A*, 505, 1183.
- Ferrarese L., Merritt D. (2000). A Fundamental Relation between Supermassive Black Holes and Their Host Galaxies. *ApJ*, 539, L9.
- Fishbone L. G. & Moncrief V. (1976). Relativistic fluid disks in orbit around Kerr black holes. *ApJ*, 207, 962.
- Font J. A. & Daigne F. (2002). On the Stability of Thick Accretion Disks around Black Holes. *ApJ*, 581, L23.
- Frank J., King A. & Raine D. J. (2002). *Accretion power in astrophysics: Third Edition*. Cambridge University Press, 2002.

- Fu W. & Lai D. (2012). Dynamics of the innermost accretion flows around compact objects: magnetosphere-disc interface, global oscillations and instabilities. *MNRAS*, 423, 831.
- Gammie C. F., McKinney J. C. & Tóth G. (2003). HARM: A Numerical Scheme for General Relativistic Magnetohydrodynamics. *ApJ*, 589, 444.
- Gardner E. & Done C. (2014). A physical model for the X-ray time lags of narrow-line Seyfert type 1 active galactic nuclei. *MNRAS*, 442, 2456.
- Gebhardt K., Bender R., Bower G. et al. (2000). A Relationship between Nuclear Black Hole Mass and Galaxy Velocity Dispersion. *ApJ*, 539, L13.
- Genzel R., Hollenbach D., Townes C. H. (1994). The nucleus of our Galaxy. *Reports on Progress in Physics*, 57, 5.
- Gerhard O. (2002). The Dynamics, Structure History of Galaxies. *ASP Conference Series*, 273.
- Ghisellini G., Tavecchio F., Foschini L. (2010). General physical properties of bright Fermi blazars. *MNRAS*, 402, 497.
- Goodman J. & Narayan R. (1988). The stability of accretion tori. III - The effect of self-gravity. *MNRAS*, 231, 97.
- Hamerský J. & Karas V. (2013). Effect of the toroidal magnetic field on the runaway instability of relativistic tori. *A&A*, 555, A32.
- Hamerský J. & Karas V. (2015). A magnetised black hole torus disrupted by stellar fly-by. *A&A*, submitted.
- Harten A., Lax P. D. & van Leer B. (1983). On upstream differencing and Godunov type methods for hyperbolic conservation laws. *SIAM Rev.*, 25, 35.
- Horák J. (2008). Weak nonlinear coupling between epicyclic modes in slender tori. *A&A*, 486,1.
- Hoyle F. & Lyttleton R. A. (1939). The effect of interstellar matter on climatic variation. *Proceedings of the Cambridge Philosophical Society*, 35, 405.
- Ipsier J. R. & Lindblom L. (1992). On the pulsations of relativistic accretion disks and rotating stars - The Cowling approximation. *ApJ* 389, 392.
- Livio M. & Koekemoer A. M. (2011). *Black Holes*. Cambridge University Press, Cambridge.
- Lu Y. & Wang T. (2000). Possible Evidence for a Truncated Thin Disk in Seyfert 1 Galaxy NGC 4593. *ApJ*, 537, L103.
- Janiuk A., Mioduszewski P. & Moscibrodzka M. (2013). Accretion and Outflow from a Magnetized, Neutrino Cooled Torus around the Gamma-Ray Burst Central Engine. *ApJ*, 776, 105.

- Janiuk A., Grzedzielski M., Capitanio F. & Bianchi S. (2014). On the interplay between the heartbeat oscillations and wind outflow in the microquasar IGR J17091-3624. ArXiv e-prints.
- Junor W. & Biretta J. (1995). The radio jet in 3C274 at 0.01 PC resolution. *Astronomical Journal*, 109, 500.
- Just A., Yurin D., Makukov M., et al. (2012). Enhanced Accretion Rates of Stars on Supermassive Black Holes by Star-Disk Interactions in Galactic Nuclei. *ApJ*, 758, 51.
- Karas V., Huré J.-M., Semerák O. (2004). TOPICAL REVIEW: Gravitating discs around black holes. *CQG*, 21, R1.
- Karas V., Matt G. (2007). Black Holes from Stars to Galaxies across the Range of Masses. Proceedings of the 238th symposium of the International Astronomical Union, Vol. 238.
- Karas V. & Šubr L. (2001). Orbital decay of satellites crossing an accretion disc. *A&A*, 376, 686.
- Karas V. & Šubr L. (2007). Enhanced activity of massive black holes by stellar capture assisted by a self-gravitating accretion disc. *A&A*, 470, 11.
- Kato S., Fukue J., Mineshige S. (2008). *Black-Hole Accretion Disks*. Kyoto University Press, Kyoto.
- Koide S., Meier D. L., Shibata K. & Kudoh T. (2000). General Relativistic Simulations of Early Jet Formation in a Rapidly Rotating Black Hole Magnetosphere. *ApJ*, 536, 668.
- Komissarov S. S. (2006). Magnetized tori around Kerr black holes: analytical solutions with a toroidal magnetic field. *MNRAS*, 368, 993.
- Korobkin O., Abdikamalov E., Schnetter E., Stergioulas N., Zink B. (2011). Stability of general-relativistic accretion disks. *Physical Review D*, 83.
- Korobkin O., Abdikamalov E., Stergioulas N., Schnetter E., Zink B., Rosswog S., Ott C. (2013). The runaway instability in general relativistic accretion discs. *MNRAS*, 431, 349.
- Krolik J. H. (1999). *Active Galactic Nuclei: from the Central Black Hole to the Galactic Environment*. Princeton University Press, Princeton.
- LaRosa T. N., Nord M. E., Lazio T. J.W., et al. (2004). New Nonthermal Filaments at the Galactic Center: Are They Tracing a Globally Ordered Magnetic Field? *ApJ*, 607, 302.
- Launhardt R., Zylka R. & Mezger P. G. (2002). The nuclear bulge of the Galaxy. III. Large-scale physical characteristics of stars and interstellar matter. *A&A*, 384, 112.

- Lax P. D & Wendroff B. (1960). Systems of conservation laws. *Communications on Pure and Applied Mathematics*, 13, 217.
- Lee W. H., Abramowicz M. A. & Kluźniak W. (2004). Resonance in Forced Oscillations of an Accretion Disk and Kilohertz Quasi-periodic Oscillations. *ApJ*, 603, L93.
- LeVeque R. J. (1997). *Computational Methods for Astrophysical Fluid Flow*. Saas-Fee Advanced Course 27 Lecture Notes, New York Springer, p.1.
- Liu S., Melia F., Petrosian V. (2006). Stochastic Electron Acceleration During the Near-Infrared and X-Ray Flares in Sagittarius A\*. *ApJ*, 636 798.
- Lovelace R. V. E. (1976). Dynamo model of double radio sources. *Nature*, 262, 649.
- Lu Y., Cheng K. S., Yang L. T., Zhang L. (2000). A massive thick disc around a massive black hole and its runaway instability. *MNRAS*, 314, 453.
- Magorrian J., Tremaine S., Richstone D. et al. (1998). The Demography of Massive Dark Objects in Galaxy Centers. *The Astronomical Journal*, 115, 2285.
- Masada Y. & Sano T. (2008). Axisymmetric Magnetorotational Instability in Viscous Accretion Disks. *ApJ*, 689, 1234.
- Masuda N., Nishida S., Eriguchi Y. (1998). The runaway instability of self-gravitating tori with non-constant specific angular momentum around black holes. *MNRAS*, 297, 1139.
- Matt G., Porquet D., Bianchi S. et al. (2005). A changing inner radius in the accretion disc of Q0056-363? *A&A*, 435, 857.
- McKinney J. C. & Blandford R. D. (2009). Stability of relativistic jets from rotating, accreting black holes via fully three-dimensional magnetohydrodynamic simulations. *MNRAS*, 394, L126.
- McKinney J. C., Tchekhovskoy A., Blandford R. D. (2012). General relativistic magnetohydrodynamic simulations of magnetically choked accretion flows around black holes. *MNRAS*, 423, 3083.
- Merloni A., Heinz S. & Di Matteo T. (2003). A fundamental plane of black hole activity. *arXiv:astro-ph/0305261*.
- Merritt D. & Ferrarese L. (2001). Relationship of Black Holes to Bulges. *ASP Conference Series*, 249, 335.
- Misner C. W., Thorne K. S. & Wheeler J. A. (1973). *Gravitation*. W. H. Freeman and Company, New York.
- Montero P. J., Font J. A., Shibata M. (2010). Influence of Self-Gravity on the Runaway Instability of Black-Hole-Torus Systems. *Physical Review Letters*, 104, 191101.

- Montero P. J. & Zanotti O. (2012). Oscillations of relativistic axisymmetric tori and implications for modelling kHz-QPOs in neutron star X-ray binaries. *MNRAS*, 419, 1507.
- Mosquera A. M., Kochanek C. S., Chen B., et al. (2013). The Structure of the X-Ray and Optical Emitting Regions of the Lensed Quasar Q 2237+0305. *ApJ*, 769, 53.
- Narayan R. (2000). Hydrodynamic Drag on a Compact Star Orbiting a Supermassive Black Hole. *ApJ*, 536, 663.
- Noble S. C., Gammie C. F., McKinney J. C., Del Zanna L. (2006). Primitive Variable Solvers for Conservative General Relativistic Magnetohydrodynamics. *ApJ*, 641, 626.
- Novak G., Chuss D. T., Renbarger T., et al. (2003). First Results from the Submillimeter Polarimeter for Antarctic Remote Observations: Evidence of Large-Scale Toroidal Magnetic Fields in the Galactic Center. *ApJ*, 583, L83.
- Okazaki A. T., Kato S. & Fukue J. (1987). Global trapped oscillations of relativistic accretion disks. *PASJ*, 39, 457.
- Pariev V. I. & Colgate S. A. (2007). A Magnetic  $\alpha$ - $\omega$  Dynamo in AGN Disks. I. The Hydrodynamics of Star-Disk Collisions and Keplerian Flow. *Apj*, 658, 114.
- Peterson B. M. (1997). Book Review: An introduction to active galactic nuclei. New York Cambridge University Press, Cambridge.
- Pétri J. (2005). Forced oscillations in magnetized accretion disks and QPOs. *A&A*, 439, 443.
- Pino J. & Mahajan S. M. (2008). Global axisymmetric Magnetorotational Instability with density gradients. *ApJ*, 678, 1223.
- Pugliese D. & Montani G. (2013). Squeezing of toroidal accretion disks. *Europhysics Letters*, 101, 19001.
- Pugliese D., Montani G., Bernardini M. G. (2013). On the Polish doughnut accretion disc via the effective potential approach. *MNRAS*, 428, 952.
- Pugliese D. & Montani G. (2015). Relativistic thick accretion disks: Morphology and evolutionary parameters. *Physical Review D*, 91, 083011.
- Quataert E., Di Matteo T., Narayan R. & Ho L. C. (1999). Possible Evidence for Truncated Thin Disks in the Low-Luminosity Active Galactic Nuclei M81 and NGC 4579. *ApJ*, 525, L89.
- Rauch K. P. (1995). Dynamical evolution of star clusters around a rotating black hole with an accretion disc. *MNRAS*, 275, 628.

- Rees M. J. (1984). Black Hole Models for Active Galactic Nuclei. Annual review of astronomy and astrophysics, 22, 471.
- Reynolds C. S., Garofalo D. & Begelman M. C. (2006). Trapping of Magnetic Flux by the Plunge Region of a Black Hole Accretion Disk. ApJ, 651, 1023.
- Rezzolla L., Yoshida S., Zanotti O. (2003). Oscillations of vertically integrated relativistic tori - I. Axisymmetric modes in a Schwarzschild space-time. MNRAS, 344, 978.
- Sbarrato T., Ghisellini G., Maraschi L. (2012). The relation between broad lines and gamma-ray luminosities in Fermi blazars. MNRAS, 421, 1764.
- Schödel R., Ott T., Genzel R. (2003). Stellar Dynamics in the Central Arcsecond of Our Galaxy. ApJ, 596, 1015.
- Schödel R., Feldmeier A., Kunneriath D., et al. (2014). Surface brightness profile of the Milky Way's nuclear star cluster. A&A, 566, A47.
- Seguin F. H. (1975). The stability of nonuniform rotation in relativistic stars. ApJ, 197, 745.
- Seth A., Agüeros M., Lee D. & Basu-Zych A. (2008). The Coincidence of Nuclear Star Clusters and Active Galactic Nuclei. ApJ, 678, 116.
- Shakura N. I. & Sunyaev R. A. (1973). Black holes in binary systems. Observational appearance. A&A, 24, 337.
- Stawarz L. & Petrosian V. (2008). On the Momentum Diffusion of Radiating Ultrarelativistic Electrons in a Turbulent Magnetic Field. ApJ, 681, 1725.
- Stephani H. (1982). *General Relativity*. Cambridge University Press, Cambridge.
- Stone J. M. & Norman M. L. (1992). ZEUS-2D: A radiation magnetohydrodynamics code for astrophysical flows in two space dimensions. I - The hydrodynamic algorithms and tests. ApJS, 80, 753.
- Stone J. M., Gardiner T. A., Teuben P. et al. (2008). Athena: A New Code for Astrophysical MHD. ApJS, 178, 137.
- Straub O. & Šrámková E. (2009). Epicyclic oscillations of non-slender fluid tori around Kerr black holes. CQG, 26, 055011.
- Stuchlík Z., Hledík S., Truparová K. (2010). Evolution of Kerr superspinars due to accretion counterrotating thin discs. CQG, 28, 155017.
- Sunyaev R. A., Markevitch M. & Pavlinsky M. (1993). The center of the Galaxy in the recent past - A view from GRANAT. ApJ, 407, 606.
- Summerlin E. J. & Baring M. G. (2012). Diffusive Acceleration of Particles at Oblique, Relativistic, Magnetohydrodynamic Shocks. ApJ, 745, 63.

- Svoboda J., Guainazzi M. & Karas V. (2010). Warm absorber and truncated accretion disc in IRAS 05078+1626. *A&A*, 512, A62.
- Syer D., Clarke C. J. & Rees M. J. (1991). Star-disc interactions near a massive black hole. *MNRAS*, 250, 505.
- Šubr L., Karas V. & Huré J.-M. (2004). Star-disc interactions in a galactic centre and oblateness of the inner stellar cluster. *MNRAS*, 354, 1177.
- Tassoul J. L. (1978). *Theory of rotating stars*. Princeton Series in Astrophysics, Princeton University Press.
- Tóth G. (1998). *Computational Magnetohydrodynamics. Notes for an introductory level course*. Porto.
- Urry C. M. & Padovani P. (1995). Unified Schemes for Radio-Loud Active Galactic Nuclei. *PASP*, 107, 803.
- Wang J.-M., Du P., Baldwin J. A., et al. (2012). Star Formation in Self-gravitating Disks in Active Galactic Nuclei. II. Episodic Formation of Broad-line Regions. *ApJ*, 746, 137.
- Watson L. C., Martini P., Dasyra K. M. et al. (2008). First stellar velocity dispersion measurement of a luminous quasar host with Gemini North Laser. *ApJ*, 682, L21. Guide Star Adaptive Optics.
- Wielgus M., Fragile P. C., Wang Z. & Wilson J. (2015). Local stability of strongly magnetized black hole tori. *MNRAS*, 447, 3593.
- Wilson D. B. (1984). A runaway instability in thick accretion disks? *Nature* 312, 620.
- Yuan F. & Narayan R. (2014). Hot Accretion Flows Around Black Holes. *ARA&A*, 52, 529.
- Zanotti O., Rezzolla L., Font J. A. (2003). Quasi-periodic accretion and gravitational waves from oscillating toroidal neutron stars around a Schwarzschild black hole. *MNRAS*, 341, 832.
- Zanotti O. & Pugliese D. (2015). Von Zeipel's theorem for a magnetized circular flow around a compact object. *GRGr*, 47, 44.
- Zurek W. H., Siemiginowska A. & Colgate S. A. (1994). Star-disk collisions and the origin of the broad lines in quasars. *ApJ*, 434, 46.



# List of author's publications

## Publications in refereed journals

Hamerský J., Karas V. (2015). A magnetised black hole torus disrupted by stellar fly-by. *A&A*, submitted (11 pages).

Karas V., Kopáček O., Kunneriath D., Hamerský J. (2014). Oblique magnetic fields and the role of frame dragging near a rotating black hole. *Acta Polytechnica*, 54, 398 (16 pages).

Hamerský J., Karas V. (2013). Effect of the toroidal magnetic field on the runaway instability of relativistic tori. *A&A*, 555, A32 (8 pages).

## Publications in conference proceedings

Hamerský J. & Karas V. (2014). Triggered oscillations and destruction of magnetized relativistic tori in 2D. *Proceedings of RAGtime 14-16: Workshops on black holes and neutron stars*, editors: Stuchlík Z., Török G. & Pecháček T. (Silesian University in Opava), pp. 107-114.

Karas V., Hamerský J. (2014). Effects of magnetic field on the runaway instability of relativistic accretion tori near a rotating black hole. *Proceeding of the International Astronomical Union*, 303, editors: Sjouwerman L., Ott J. & Lang C., Cambridge University Press (Cambridge), pp. 424-426.

Hamerský J. (2012). On transfer of mass and angular momentum from accretion disk onto black hole. *Proceedings of the 21st annual conference of doctoral students, Part III - Physics*, editors: Šafránková J. & Pavlů J., MATFYZPRESS, Faculty of Mathematics and Physics (Prague), pp. 111-115.